INDRAPRASTHA INSTITUTE OF INFORMATION TECHNOLOGY, DELHI

DOCTORAL THESIS

Spatiotemporal Linear Stability of Viscoelastic Free Shear Flows

---

Author:
Diksha BANSAL

Supervisor:
Dr. Sarthok SIRCAR

*A thesis submitted in fulfillment of the requirements
for the degree of Doctor of Philosophy*

to the

Indraprastha Institute of Information Technology Delhi

INDRAPRASTHA INSTITUTE *of*
INFORMATION TECHNOLOGY DELHI

March 18, 2021

ii

CERTIFICATE

This is to certify that the thesis titled "Spatiotemporal Linear Stability of Viscoelastic Free Shear Flows" being submitted by Diksha BANSAL to the Indraprastha Institute of Information Technology Delhi, for the award of the degree of Doctor of Philosophy, is an original research work carried out by her under my supervision. In my opinion, the thesis has reached the standards fulfilling the requirements of the regulations relating to the degree.

The results contained in this thesis have not been submitted in part or full to any other university or institute for the award of any degree/diploma.

August, 2020
Dr. Sarthok SIRCAR

Indraprastha Institute of Information Technology Delhi
New Delhi 110020

iv

INDRAPRASTHA INSTITUTE OF INFORMATION TECHNOLOGY, DELHI

Abstract

Doctor of Philosophy

Spatiotemporal Linear Stability of Viscoelastic Free Shear Flows

by Diksha BANSAL

In this thesis, we have explored the temporal and spatiotemporal stability analyses of free shear, viscoelastic flows in the limit of low to moderate Reynolds number (Re) and Weissenberg number (We). The description of the six chapters are as follows:

• The first chapter introduces the fundamental difference in the instability arising from Newtonian versus non Newtonian fluids: Newtonian fluid undergoes instabilities with increasing Re, although a direct transition to instability is also possible via bypass transition. Contrarily, non Newtonian fluids exhibit both inertial and purely elastic instabilities that arise even when the effect of inertia is too small to drive an instability in a Newtonian fluid at the same flow condition. Past research by several groups are highlighted.

• The second chapter discusses the Compound Matrix Method (CMM) which is used to numerically integrate the eigenvalue problem using auxiliary variables emerging from the Orr-Sommerfeld equation (OSE).

• In the third chapter, a description of the different types of instabilities is included. The temporal modes refer to cases where the instability in the complex frequency is determined as a function of real wave number. The convectively unstable modes give rise to wave packets moving away from the source and ultimately leaving the medium in its undisturbed state. Absolutely unstable modes, by contrast, are gradually contaminated everywhere from a point-source disturbance. Evanescent modes (or the direct resonance mode) arise if the two coalescing modes originate from waves propagating in the same direction.

• The fourth chapter highlights the stability analyses of antisymmetric, free shear, viscoelastic flows in the dilute regime, obeying the Oldroyd-B constitutive equation. The temporal stability analysis indicates that with increasing We, (a) the entire range of the most unstable mode is shifted toward longer waves, (b) the vorticity structure contours are dilated, and (c) the residual Reynolds stresses are diminished. The spatiotemporal analyses show that the free shear flow of dilute polymeric liquids is either (absolutely/convectively) unstable for all Re or the transition to instability occurs at comparatively low Re.

- In the fifth chapter, we provide a detailed comparison of the temporal and the spatiotemporal linearized analyses of free shear, viscoelastic flows in the limit of low to moderate Reynolds number and Elasticity number obeying four different types of stress-strain constitutive equations: Oldroyd-B($\varepsilon = 0, a = 1$), Upper Convected Maxwell($\varepsilon = 0, a = 1, v = 0$), Johnson-Segalman ($\varepsilon = 0, a = 0.5$) and Phan-Thien Tanner($\varepsilon = 0.5, a = 0.5$). The temporal stability analysis indicates (a) elastic stabilization at higher values of elasticity number and (b) a non- monotonic instability pattern at low to intermediate values of elasticity number for the JS as well as the PTT model. The spatiotemporal phase diagram divulge the familiar regions of inertial and elastic turbulence, a recently verified region of elastoinertial turbulence and the unfamiliar temporally stable region for intermediate values of Reynolds and Elasticity number.

- In the concluding chapter, we highlight the challenges that we have faced and intend to face in future numerical simulations as well as our future problems demanding a full spatiotemporal stability analyses: (a) Rayleigh-Plateau, describing the onset of the detachment of a droplet, (b) Saffman-Taylor, or the formation of patterns in a morphologically unstable interface between two fluids in a porous medium, (c) Faraday instability, or an unstable state of a flat hydrostatic surface due to a critical vibration frequency.

Acknowledgements

As I stand at the end of this journey, I would like to thank all those who have been involved in ensuring I reached my destination. First and foremost, I thank God for his illuminating power, which has shown me the way to tread. I'd like to express my deepest gratitude to my supervisor, Dr. Sarthok Sircar, who has supported me throughout my Ph.D. journey. I am extremely grateful for our friendly chats at the end of our meetings.

Besides my advisor, I would like to thank Dr. G.P.S. Raghava and Dr. Ashish Kumar Pandey for their insightful comments and willingness to serve on my doctorate committee. Also, I am very thankful to my fellow labmates, especially my colleague Akansha Arora for helping me to take plenty of rest by regularly providing distraction, and ensuring that the journey has been an extremely enjoyable one.

I am deeply indebted to my parents and my family members, who are always there supporting me and giving me the freedom to pursue my interest. This journey would not have been possible without their unparalleled love and motivation. Lastly by mostly, I am deeply appreciative of the support and encouragement offered by my best friends: Nitesh Sharma, Ananta Thakur, Sarswati Shah, Nitish Mehta for their tremendous emotional support during all the years of my Ph.D. life. In addition, thank you to all the other friends who have made my life better through their friendship throughout my life so far, whose names are too many to count.

Finally, I would like to acknowledge the financial support by Council of Scientific & Industrial Research (CSIR), India and a very special thanks to IIITD for providing me the necessary facilities and a healthy research environment.

Diksha Bansal

Contents

List of Figures

Dedicated to my nieces Aradhya and Divija.

Chapter 1

Introduction and review of literature

This chapter provides a general overview of the past research in Newtonian as well as non-Newtonian fluid instabilities, and organized as follows: §1.1 outlines the basic difference of the instability arising in Newtonian fluids versus those arising in non-Newtonian (viscoelastic) fluids. §1.2 outlines the basic features of the viscoelastic flows. §1.3 delineates the phenomena of 'turbulence' and §1.4 describes some of the basic transition pathways to instability and turbulence in viscoelastic fluids. Finally, some industrial applications are provided in §1.5.

1.1 Newtonian versus viscoelastic instability

For a fluid with kinematic viscosity v in a geometry of linear scale L with a typical flow velocity V, the Reynolds number, $Re = \frac{VL}{v}$ is the ratio of the inertial term of $\mathcal{O}(V^2/L)$ and the viscous damping term of order $\frac{vV}{L^2}$ at the largest relevant scale, the scale of the flow geometry. It is well known that when the Reynolds number increases, flows of Newtonian fluids typically follow a scenario: (a) at small Re the flow is laminar and stable, (b) at some intermediate value the laminar flow profile becomes unstable, so that a more complicated flow pattern develops, while (c) at sufficiently large Reynolds numbers the flow is turbulent (Morozov and Sarloos, 2007). However, a direct transition from a laminar flow to turbulent flow (also known as the 'bypass transition') is also possible (Negi et al., 2019; Sundarama, Sengupta, and Sengupta, 2019). An exception to such a sequence of transition pathway to turbulence in Newtonion fluids are the wall-bounded flows (Sengupta and Bhaumik, 2018).
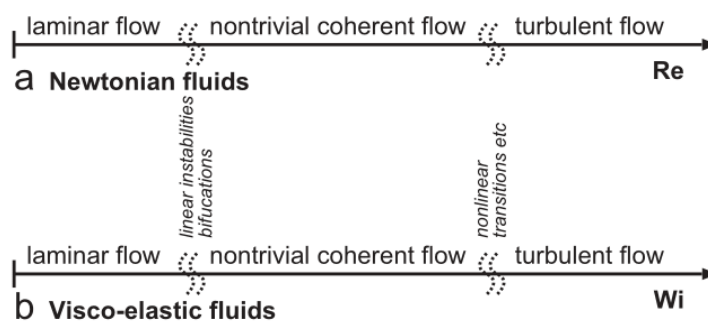
FIGURE 1.1: Qualitiative sketch stressing the similarities between a typical scenario found in Newtonian fluids as the Reynolds number Re increases, and in visco-elastic fluids upon increase of the Weissenberg number We. (Source (Morozov and Sarloos, 2007))

Newtonian fluids are simple fluids like water and alcohol whose dynamics is described by the Navier-Stokes equations (Sengupta, 2016). Since the Reynolds number measures the importance of inertial effects relative to the viscous damping effects, the typical scenario is that as inertial terms become more and more important in normal Newtonian flows, there is a tendency to more and more complicated flow patterns and eventually turbulence. Sometimes the first transition is a transition to a nontrivial coherent flow pattern, and this transition is followed by one or more secondary bifurcations, before the turbulent regime is reached. But a direct transition from a laminar flow to a turbulent flow is also possible (also known as the 'bypass transition'). Contrarily, viscoelastic dilute polymeric liquids exhibit both the inertial (Bird, Armstrong, and Hassager, 1987; Bird et al., 1987) and purely elastic instabilities (instabilities which arise even when the effect of inertia is too small to drive an instability in a Newtonian fluid at the same flow conditions) (Larson, Shaqfeh, and Mueller, 1990). Inertial effects are usually negligible as the Reynolds numbers are small but the fluid is strongly non-Newtonian due to the shear-induced elasticity and anistropy, or the so-called 'slow relaxation effects'. The dimensionless number governing these non-Newtonian effects is the Weissenberg number (*We*). From a number of precise experiments and theoretical investigations in the last fifteen years, it has become clear that as the *We* increases, visco-elastic fluids exhibit flow instabilities driven by the anisotropy of the normal stress components and the curvature of the streamlines (Groisman and Steinberg, 1998). The combination of these normal stress effects that drive laminar curved flow unstable and the possibilty of the elastic effects to store energy in high shear regions and to dump it elsewhere in less sheared regions, appears to be strongly self-enhancing: Instabilities and the transition to a turbulent regime driven by these elastic forces, are often found to be hysteretic and strongly subcritical (nonlinear) (Groisman and Steinberg, 2000).

1.2 Basic features of viscoelastic flows

In viscoelastic flows of polymeric solutions, the Reynolds numbers are often quite small, since the viscosity is large. Polymeric fluids are sometimes called viscoelastic fluids. This means that the fluids have both viscous and elastic properties. The use of the word "elastic" to characterize a property of a fluid may seem a bit contradictory. By elasticity one usually means the ability of a material to return to some unique, original shape; on the other hand, by a fluid one means a material that will take the shape of any container in which it is left, and therefore does not possess a unique, original shape. Another concept that is closely tied to that of elasticity is the concept of "memory". Indeed a material that has no memory cannot be elastic, since it has no way of remembering a unique, original shape. Hence fluids exhibiting elastic properties are also often referred to as memory fluids. Since polymeric fluids are not chemically cross-linked they will not have a permanent memory, but there will be a finite long relaxation time. We say that the relaxation spectrum gives the fluids a fading memory of duration of the longest relaxation time. When the longest relaxation time is equal to or greater than the characteristic time for the macroscopic flow system, marked deviations from Newtonian behavior are observed. The distinction between the rheology and the fluid mechanics of viscoelastic materials is vague but is worth

stating. The former is concerned with constitutive relations between stress and deformation and may involve physical modeling at a molecular level. Controllability of the flow field is essential when making rheological measurements to evaluate material properties, so the kinematics are generally imposed and the momentum equation is not solved. Viscoelastic fluid mechanics, on the other hand, is the study of motions in which the kinematics cannot be established a priori, and the continuity and momentum equations must be solved together with the constitutive equation for the stress. The equations that must be solved for even the most elementary viscoelastic liquids are considerably more complex than the Navier-Stokes equations, and many unresolved issues of a fundamental nature remain (Denn, 1990). Students of viscoelastic fluid mechanics have therefore focused on the use of constitutive equations that capture important qualitative features of material rheology, but that are simplistic relative to the formulations believe to characterize real materials. When polymers are long, they get easily stretched by the shear present in flows, and the viscosity of the solution is large. Solutions of flexible high molecular weight polymers differ from Newtonian fluids in many aspects (Bird, Armstrong, and Hassager, 1987). The most striking elastic property of the polymer solutions is that stress does not immediately become zero when the fluid motion stops, but rather decays with some characteristic time, λ, which can reach seconds and even minutes. Equation of motion for dilute polymer solutions differs from the Navier-Stokes equation by an additional linear term due to the elastic stress, τ (Bird et al., 1987). Since the elastic stress is caused by stretching of the polymer coils, it depends on history of motion and deformation of fluid elements along its flow trajectory. This implies non-linear relationship between τ and the rate of deformation in a flow (Bird, Armstrong, and Hassager, 1987). The non-linear mechanical properties of polymer solutions are well manifested in their large extensional viscosity at high rates of extension (Tirtaatmadja and Sridhar, 1993) and in the Weissenberg effect (Bird, Armstrong, and Hassager, 1987; Weissenberg, 1947).

The important dimensionless number characterizing the rheology of polymers is *We* which controls the stretching of the polymers, the so-called normal stress effect, or the relaxation phenomena. Alternatively, the $We = V\lambda/L$ (or the product of the characteristic rate of deformation and the relaxation time) is a measure of degree of nonlinearity in the mechanical properties of the viscoelastic fluid. When the *We* becomes large, in practice larger than 1, the fluid rheology deviates from a regular Newtonian flow (Bird, Armstrong, and Hassager, 1987; Denn, 1990; Denn, 2004; Shaqfeh, 1996; Larson, 1999; Larson, 1988). A simple well-known example of this is the so-called rod-climbing effect (Bird, Armstrong, and Hassager, 1987)(refer Figure 1.2). Viscoelastic effects manifest themselves in shear flows through the normal stress, which first appears as a quadratic term in shear rate. Inertial stresses are of order ρV^2, where ρ is the density. This competition is dramatically illustrated via inserting rotating rods in two beakers. First one contains a Newtonian liquid while the second one contains a polymer solution. In figure 1.2, we see that the Newtonian liquid near the rotating rod is pushed outward by the centrifugal force and a dip arises near the center of the beaker. The contrasting behavior is for the polymer solution where it moves towards the center of the beaker and starts to climb up the rod. Moreover, for comparable rotational speeds, the polymer solution seems to respond far more dramatically than Newtonian liquid.
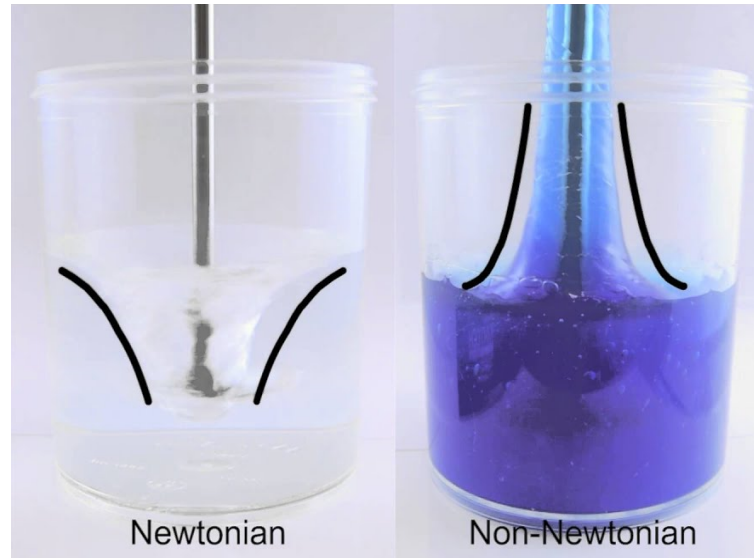
FIGURE 1.2: Rod climbing in solution of high molecular weight polystyrene in a Newtonian fluid(right) and no effect in Newtonian fluid(left) (Source: https://ewoldt.mechanical.illinois.edu/)

This phenomenon has undoubtedly been known for a long time and it seems first to have been discussed in the context of normal stresses in a lecture by Weissenberg in 1946, and it is therefore known as the "*Weissenberg effect*"(Figure 1.2). The phenomenon can be interpreted in a rather simple fashion with the use of an extra tension along the streamlines. Rod climbing is easily analyzed approximately in the absence of surface tension. Simple models of viscoelastic liquids predict a tension along a circular streamline, which must be balanced by an increased hydrostatic pressure, and this simple approach leads to an analytical solution for many viscoelastic constitutive equations. A number of important effects in the flow of polymeric liquids may be attributed to the fact that polymeric liquids exhibit normal stress differences in shear flows. Let us first establish some labeling conventions for referring to normal stress differences. If the fluid moves along one coordinate direction only and its velocity varies only in one other coordinate direction, then we call the direction of fluid velocity the "1" direction; the direction of velocity variation, the "2" direction; and the remaining neutral direction, the "3" direction. Then we call $\tau_{11} - \tau_{22}$, the first normal stress difference. Likewise, we call $\tau_{22} - \tau_{33}$ the second normal stress difference. x, y, and z correspond to 1, 2, and 3 respectively. Thus the first normal stress difference is $\tau_{xx} - \tau_{yy}$ and the second normal stress difference is $\tau_{yy} - \tau_{zz}$. For Newtonian fluids the normal stress differences are exactly zero in shearing flow. For polymeric fluids the first normal stress difference is practically always negative and numerically much larger than the second normal stress difference. This means that to a first approximation polymeric fluids exhibit in addition to the shear stresses an extra tension along the streamlines, that is, in the "u1" direction. It was shown by Weissenberg that the simple notion of an extra tension along streamlines may be used to obtain qualitative explanations of a large number of experiments. The second normal stress difference has been found experimentally to be positive, but usually much smaller than the magnitude of the first normal stress difference. This means that in a

shear flow the fluid exhibits a small extra tension in the "3" direction. A simple structural explanation for this extra tension is lacking, and the simplest kinetic theories of polymeric fluids are not capable of describing this effect; more elaborate theories are successful, however (Bird, Armstrong, and Hassager, 1987). We emphasize that the second normal stress difference is quite small, and it is normally observable only in situations where the first normal stress difference, for geometrical reasons, has no effect.

1.3 Turbulence

Turbulence is one of the most fascinating phenomena in nature and one of the biggest challenges for modern physics. It is common knowledge that a flow of a simple, Newtonian fluid is likely to be turbulent when velocity is high, viscosity is low and size of the tank is large. Recent examples in the category of Newtonian fluid turbulence include the analytical techniques to study the Boussinesq approximation in Richtmyer-Meshkov Instabilities (RMI) (Mikaelian, 2014), a non-perturbative approach to study the spatial instability of weakly non-parallel shear flow (Huang and Wu, 2015), Direct Numerical Simulations (DNS) of Rayleigh Taylor Instability (RTI) between two air masses with a temperature gradient (Sengupta et al., 2016), the impulse response of a canonical zero pressure gradient boundary layer via the dynamical system approach (Bhaumik and Sengupta, 2017) and the DNS of a wavepacket in laminar to turbulent transition in a Blasius boundary layer with the wave modes decomposed using a combination of Proper Orthogonal Decomposition (POD) and Fast Fourier Transform (FFT) (Kang and Yeo, 2017). However, a direct transition from a laminar flow to a turbulent flow is also possible (Sundarama, Sengupta, and Sengupta, 2019). Motion of simple, low molecular, Newtonian fluids is governed by the Navier-Stokes equation (Landau and Lifshitz, 1987; Tritton, 1988). This equation has a non-linear term, which is inertial in its nature. The ratio between the non-linearity and viscous dissipation is given by the Reynolds number, $Re = VL/\nu$, where V is velocity, L is characteristic size and ν is kinematic viscosity of the fluid. When Re is high, non-linear effects are strong and the flow is likely to be turbulent. So, turbulence is a paradigm for a strongly non-linear phenomenon (Landau and Lifshitz, 1987; Tritton, 1988). There is no unique commonly accepted definition of turbulent flow (Tritton, 1988), so it is usually identified by its major features (Landau and Lifshitz, 1987; Tritton, 1988). Turbulence implies fluid motion in a broad range of spatial and temporal scales, so that many degrees of freedom are excited in the system. A striking practically important characteristic of turbulent flows is major increase in the flow resistance compared to an imaginary laminar flow with the same *Re*. It is reasonable to inquire, whether non-linearity of mechanical properties of a fluid can give rise to turbulent flow, when the equation of motion is linear. For a polymer solution this corresponds to a state, when the Weissenberg number is large, while the Reynolds number is small. This situation can be realized, if the parameter of elasticity $We/Re = \lambda\nu/L^2$ is large enough. An important step in investigation of influence of the non-linear mechanical properties on flow was made about a decade ago, when purely elastic instability was experimentally identified in curvilinear shear flows (Magda and Larson, 1988; Muller, Larson, and Shaqfeh, 1989). This instability occurs at moderate *We* and vanishingly small *Re* and is driven by the elastic

stresses (Muller, Larson, and Shaqfeh, 1989; Larson, Shaqfeh, and Mueller, 1990; Groisman and Steinberg, 1998). As a result of this instability, secondary, in general oscillatory, vortex flows develop, and flow resistance somewhat increases (Magda and Larson, 1988; Muller, Larson, and Shaqfeh, 1989; Larson, Shaqfeh, and Mueller, 1990; Groisman and Steinberg, 1998; Byars et al., 1994). There are elastic stresses that appear in the polymer solutions in a flow, and that grow non-linearly with the flow rate (Bird et al., 1987). This can lead to many special flow effects, including purely elastic transitions (Larson, Shaqfeh, and Mueller, 1990; Byars et al., 1994; Joo and Shaqfeh, 1994) that qualitatively change character of the flow at vanishingly small Re. As a result of such transitions secondary vortical flows appear in different systems, where the primary motion is a curvilinear shear flow. Onset of those secondary flows depends on the $We = \lambda \dot{\gamma}$, where $\dot{\gamma}$ is the shear rate. It plays a role analogous to that of Re in competition between non-linearity and dissipation. As it has been reported recently, an elastic flow transition can result in a special kind of turbulent motion, elastic turbulence (Groisman and Steinberg, 2000), which arises at arbitrary small Re. A second and more recent instability is the so called 'elastoinertial turbulence' (occurring at moderate Re and large We) which is characterized by maximum drag reduction state, and originates from a linear instability of pipe and channel flows. In a series of experiments in the 1960s and 1970s, this transition to turbulence was observed in dilute polymer solutions, at Reynolds numbers much lower than Newtonian threshold by several groups, the phenomena being dubbed as "early turbulence" (Hansen and Little, 1974). Later (A. A. Draad and Nieuwstadt, 1998) observed an order of magnitude reduction in the natural (unforced) transition Re for a polymer solution. More recently, (Samanta et al., 2013) studied transition in polyacrylamide solutions, in smaller diameter pipes, thereby accessing higher Weissenberg numbers. In a 4 mm diameter pipe, the transition process for concentrations lesser than 200 ppm was analogous to the Newtonian one with forced and natural transitions occurring at disparate Reynolds numbers. In sharp contrast, for the 500 ppm solution, the transition occurred at $Re \sim 800$ independent of the perturbation amplitude. Further, spatially localized structures (puffs), characteristic of the bistability associated with the Newtonian subcritical transition (Barkley, 2016), were absent. Subsequently, this new transitional pathway, connecting the laminar state to a novel elastoinertial turbulent state, has been demonstrated over a much wider parameter range (Choueiri, Alonso, and Hof, 2018). Fluids can exhibit non-Newtonian behavior in a number of ways. They may be purely viscous, in that the stress depends on the rate of deformation in a nonlinear fashion, but there is no dependence on the past history of the deformation. They maybe viscoelastic, in that the stress depends in a well-defined way on the history of the deformation; viscoelastic liquids are also called memory fluids, and basic invariance principles of physics require that their stress dependence be nonlinear for any finite deformation. The term viscoelasticity is used because these fluids respond to deformations over short time scales like elastic solids, but they flow like ordinary liquids over long time scales. Non-Newtonian fluid behavior is to some extent a matter of timescales. Even argon will exhibit non-Newtonian behavior if the deformation rate is comparable to the reciprocal of the molecular relaxation time. Fluids that are non-Newtonian over observable time scales (milliseconds to minutes) usually have a microstructure that must relax; typical examples are entangled polymers and colloidal suspensions. For

most fluid mechanics applications, the microstructure must exist over a sufficiently small spatial scale to permit averaging and the use of a continuum approximation. The standard problem in non-Newtonian fluid dynamics arises when the continuum constitutive equation relating the stress tensor to the rate of deformation tensor is known, resulting in a coupled set of field equations that must be solved for a specified geometry and defined boundary conditions. The constitutive equation depends on the particular microstructure and might be in the form of algebraic, differential, integral, or integro-differential equations. Two characteristics emerge in flows in which memory fluids differ qualitatively from those in Newtonian fluids: normal stress effects in shear that counter inertial effects (see Weissenberg effect above), and stresses in extensional deformations that can be orders of magnitude larger than those in Newtonian fluids. A common situation in which inertia and fluid elasticity result in qualitatively different contributions to the motion is flow near a rotating disk. The inertial (von Karman) flow for Newtonian fluids is a textbook example, because it is one of the few cases in which an exact solution can be obtained to the full Navier-Stokes equations. The fluid near the disk is pumped outward as a manifestation of the "centrifugal force", while the fluid flows uniformly toward the disk to conserve mass. Viscoelasticity, however, induces the opposite flow: fluid flows radially inward near the disk, with a transverse flow away from the disk to conserve mass. This phenomenon seems to have been observed by Reiner and coworkers (Reiner, Blair, and Hawley, 1949), but they provide no details. Descriptions of noninertial secondary motions induced by rotating surfaces began to appear in the published literature in the early 1960's, many in articles by Giesekus. There are numerous reproductions of these early experiments, as well as later ones, in Boger and Walters (Boger and Walters, 1993). The effect of fluid elasticity on rotational flows has obvious significance for laminar mixing, both in polymer processing and in biotechnology, where dissolved polysaccharides may cause similar phenomena (Hill, 1972). These effect results in nonlinear effects on hydrodynamic length scales, as they are induced by the shear rate (the velocity gradient) in the flow being large enough, larger than the inverse of the longest polymer relaxation time. So, in viscoelastic flows the nonlinear effects do not come from inertial terms but from the elastic terms. The question now naturally arises whether small Reynolds number viscoelastic flows will follow roughly a similar scenario as the Newtonian fluids, a laminar flow regime, followed possibly by a regime with nontrivial coherent flow patterns, then turbulence, as a function of the *We*, and what would be the mechanism of destabilization. Clearly, this question can only be posed and answered precisely for a given flow geometry and for a given rheological model (the so-called "constitutive equation" for the viscoelastic stresses). Nevertheless, the normal stress effect, which we think is the major mechanism of flow destabilization and transition to turbulence in viscoelastic flows, is very robust and common to virtually all polymers. Therefore, we feel that it is useful to think of this question in this broader sense, and to be guided by the analogy between well-known Newtonian scenario and the putative viscoelastic scenario when tackling a specific problem. As we shall discuss, in the last decade several key experiments have been done which demonstrate the existence of viscoelastic instabilities and turbulence and which lead us to propose that our thinking be guided by the analogy (Morozov and Sarloos, 2007). Moreover, these experiments indicate, loosely speaking, that viscoelastic flows might have an ever stronger tendency to become

turbulent than normal Newtonian fluids. This forces on us the question what the typical route to turbulence of viscoelastic flows is, and whether the scenario is realistic. Many of the issues are still largely open, and researchers are struggling to find a way to approach them. It is therefore too early for a review of the subject-instead this chapter has more the character of an introductory essay aimed at bringing together evidence from various angles on how strong the tendency of viscoelastic fluids is to exhibit subcritical flow transitions. One of the main threads of this essay will be that this tendency to subcritical behavior is so strong, that also viscoelastic parallel shear flows exhibit a direct subcritical transition to viscoelastic turbulence. Apart from the intrinsic scientific interest in exploring the similarity of the two scenarios discussed above, there are also very good practical reasons to do so. If Newtonian fluid dynamics remains a challenge even today, then viscoelastic flows seem to pose unsurmountable problems. First of all, at the technical level, the difficulty is that while the Navier-Stokes equations for a Newtonian fluid are simply equations for the velocity vector field, the rheological equations for a viscoelastic fluid involve a nonlinear "constitutive equation" for the stress tensor. Any calculation is therefore much harder for viscoelastic flow than for Newtonian flow, and even conceptually simple approximation schemes often lead to cumbersome expressions with many terms. Secondly, the structure of these equations is such that in flow regions with significant shear, components of the stress tensor tend to grow exponentially fast; this makes numerical simulations of such flows so hard that the difficulty of extending numerical techniques to significant Weissenberg numbers has been termed the "High Weissenberg Number Problem" (Owens and Philips, 2002; Fattal and Kupferman, 2004; Hulsen, Fattal, and Kupferman, 2005).

Finally, a complicating factor is that because there are many different constitutive equations, one always faces the question to what extent a given theoretical result is an artefact of a particular constitutive equation or an explicit example of a relatively general phenomenon. For all the above reasons, even if analogies can only help give qualitative insight into which instability scenario or route to turbulence might be possible or expected in a particular case, exploring these analogies can be of great help in studying viscoelastic flows. Our interest in viscoelastic flows as an instability problem arose when we posed ourselves the question "will viscoelastic flow in a parallel flow geometry (plane Couette flow, Poiseuille flow) exhibit some kind of nonlinear instability to (probably weakly) turbulent flow, just like Newtonian pipe and Couette flow become turbulent at high enough driving forces?" As we shall discuss, it has been accepted for quite some time that in flow geometries with curved streamlines (like a Taylor-Couette cell), viscoelastic flows become linearly unstable at high Weissenberg numbers, even when the Reynolds number is small (P.Pakdel and McKinley, 1996). These instabilities are due to the anisotropy of stress tensor, which also gives rise to the so-called rod-climbing effect of polymer solutions. If one is a bit familiar with the nonlinear (subcritical) transition to turbulence in Newtonian pipe flow or Couette flow, one naturally expects viscoelastic pipe flows to have a similar nonlinear subcritical transition to some kind of turbulent state. Simply put, one expects the laminar state to be linearly stable to perturbations of infinitesimal amplitude, but once the amplitude of the perturbation is large enough, the perturbed flow will have curved streamlines and the curved streamlines in combination with anisotropic forces mechanism will take over and the perturbations will grow even larger (Bertola et al.,

2003; Meulenbroek et al., 2003; Meulenbroek et al., 2004; Morozov and Sarloos, 2005). This is the essence of what is called a subcritical (nonlinear) transition. Quite surprisingly, after parallel shear flows were shown to be linearly stable in the mid-seventies of the previous century, the implicit assumption in the field seems to have been that such flows would also be nonlinearly or even absolutely stable, i.e., that even if such flows are perturbed significantly, they will return to steady laminar flow behavior. The final verdict on this issue is not yet in, but there are both strong theoretical and numerical indications that indeed there is indeed a nonlinear flow instability, with a threshold which decays rapidly (as $\frac{1}{We^2}$) with Weissenberg number. Moreover, we shall show in Chapter 3 that a simple back-of-the-envelope extension of the linear stability criterion of curved flows predicts that the threshold is wavenumber-independent, suggesting that the instability normally will give rise to turbulence. The question concerning the nonlinear stability of parallel shear flows actually has immediate practical and technological relevance. Beyond some rather well-defined flow rate the outflow (the "extrudate" in industrial terms) shows undulations whose amplitude increases rapidly with increasing flow rate. At high enough flow rates the flow appears to be chaotic or turbulent (Larson, 2000). In fact, various recent high-precision experiments on viscoelastic model fluids have given overwhelming evidence for the presence of turbulence in viscoelastic fluids at low Reynolds numbers (Vinogradov and Manin, 1965; Groisman and Steinberg, 2000; Groisman and Steinberg, 2001; Groisman and Steinberg, 2004). Although we will focus here on the basic issue of polymer flow stability and the onset of turbulence, we note that the effects are directly relevant technologically: the standard way of making polymer fibers in industry is extrusion, in which the molten polymer is forced through a small opening and subsequently cooled to obtain the final product. Since undulations of the extrudate are unwanted, the occurrence of such instabilities is the rate-limiting factor for such extrusion processes (Denn, 1990; Pahl, Gleissle, and Laun, 1991; Denn, 2001; Rauwendaal and Gramann, 2001). A detailed understanding of these types of phenomena has remained elusive for already over 40 years: the earliest documented attempts date back at least to the 1960s (Vinogradov and Manin, 1965), when the use of polymer fibers became widespread. Although it is clear that in some cases instabilities at the outlet of the extruder are at the origin of melt fracture phenomena, if indeed polymer pipe flow itself exhibits a nonlinear instability, these will in some sense pose a fundamental barrier to avoiding melt fracture instabilities. In fact if the instability is subcritical (nonlinear), it is likely that in practice extrusion instabilities are strongly coupled to the nonlinear instabilities in the pipe, as the latter need to be triggered by an perturbation of sufficiently large amplitude. To contrast this with the inertia-driven turbulence in Newtonian flows, Larson has coined the term "turbulence without intertia" or "elastic turbulence" (Larson, 2000).

In the 1880s Osborne Reynolds (Reynolds, 1883) established that fluid inertia (that is, momentum) drives the irregular patterns observed in water flowing rapidly from a pipe, plumes emerging from a smokestack, eddies in the wake of a bulky object, and many other everyday phenomena. Known as "turbulence", these patterns occur at high values of the Reynolds number, the dimensionless ratio of inertial to viscous force. Over the years turbulence has become better characterized, and we now know it to be accompanied not only by an increase in drag, but also by
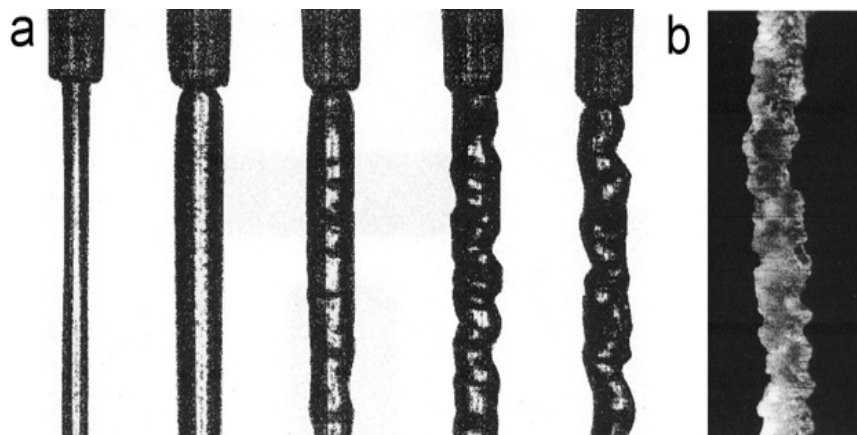
FIGURE 1.3: 1Illustration of the surface irregularities that occur in the extrusion of a polymer fluid from a tube. (a) five snapshots of a polymer flowing out of a tube (the wider structure at the top), with the flow rate increasing from left the right, (b) At high flow rates the extrudate become very irregular (Source (Morozov and Sarloos, 2007)).

certain characteristic spatial or temporal velocity fluctuations. Groisman and Steinberg (Groisman and Steinberg, 1998) show that both an increased resistance to flow and other features of turbulence can occur in fluids with hardly any inertial forces, if the role of inertia is instead played by elasticity, a force present in solutions of long-chain polymers. The flow studied by Groisman and Steinberg (Groisman and Steinberg, 2000) is simple: a polymer fluid confined between two parallel disks is sheared by rotation of one of the disks about their common axis. At increased flow rates (but rates still too low to generate much inertia) the flow acquires turbulent characteristics. Irregular flow patterns have long been seen in polymeric and other elastic fluids, and have even occasionally been dubbed "elastic turbulence" (Larson, 1988). One such flow is that of a polymer melt emerging from the end of a capillary tube. Above a critical flow rate, the polymer jet becomes irregularly distorted. Distortions in this and other polymer flows can mar products made from polymers, such as films and extruded parts. If the polymer is made more viscous by increasing the length of its polymer molecules, the minimum flow rate producing such irregular flow decreases. This is surprising because an increase in viscosity has the opposite effect on inertially driven turbulence. In fact, for fluids containing long polymer molecules, the Reynolds number at the onset of the instabilities can be minuscule, as low as 10^{-15}. Turbulent flow of water in a pipe, by contrast, has a much higher Reynolds number, around 10^5. It is clear, then, that inertia has nothing whatsoever to do with this kind of polymeric turbulence. For viscous polymers, instabilities and irregular flows set in at a critical value of *We* or the ratio of elastic to viscous forces in the fluid, which for polymeric fluids plays the role of *Re* in creating the nonlinearities that lead to unstable flow. Because elastic forces increase with polymer length more rapidly than viscous forces, fluids containing long polymers are especially prone to such phenomena, despite having viscosities that can be hundreds to millions of times higher than water. Until the work of Groisman and Steinberg (Groisman and Steinberg, 2000), quantitative measurements of the length and time scales of elastic turbulence had been lacking. Still lacking, even now, is a proper understanding of how the length and time scales of elastic turbulence are produced by the underlying elastic

forces. In other words, what is missing is an elastic counterpart of the 'cascade' picture of inertial turbulence. In this, the largest eddies in the flow feed their energy into smaller eddies, which in turn drive even smaller eddies, and so on until the energy stored in the smallest eddies is finally dissipated as heat. The resulting hierarchy of interacting eddies of various sizes is known as well-developed or hard turbulence. In Kolmogorov's 'bucket brigade' description of hard turbulence, a power-law distribution in length scales is produced by this handing off of energy from larger to smaller eddies. For "elastic turbulence", the basic mechanisms of instability in the base flow are mechanisms involving 'normal stresses'. Normal stresses are produced by the stretching of polymer molecules in a flow, leading to an elastic force like that in a stretched rubber band. If the streamlines are circular, the polymer 'rubber bands' press inward from all directions, pressure, or 'hoop stress' (Larson, Shaqfeh, and Mueller, 1990). Despite being non-inertial, there is a strong analogy between such elastic forces and inertial instabilities involving curved streamlines, such as the flow in the gap between an inner rotating and a concentric outer stationary cylinder (circular Couette flow). In either the parallel-disk flow studied by Groisman and Steinberg (Groisman and Steinberg, 2000), or the circular Couette flow, inertial forces try to fling fluid outwards, producing a radial pressure gradient, whereas elastic forces squeeze fluid inwards, tending to drive fluid up the rotating inner cylinder. Whether the stresses are inertial or elastic (directed outward or inward), there is a radial pressure gradient that, if large enough, can drive an instability, leading to a more complex flow. For non-elastic fluids, the precise mechanism for the initial instability in inertial circular Couette flow was worked out by Taylor (Taylor, 1923) in 1923, whereas analogous work for purely elastic instabilities (Phan-Thien, 1983; Larson, Shaqfeh, and Mueller, 1990; Byars et al., 1994)dates only from around 1985-95. Beyond these initial instabilities, the first steps are being taken to work out the cascades of instabilities in elastic flows. The work of Groisman and Steinberg (Groisman and Steinberg, 2000) leaps over these cascades, deliberately inciting highly unstable flow by having a large gap between the disks, relative to the disk diameter, so that the stabilizing influence of the viscous drag is minimized. The result is a flow with the power-law structures characteristic of hard, well-developed turbulence, but with negligible inertia.

1.4 Instability and transition to turbulence

Developing an understanding of instability and transition in free shear flows at low to moderate *Re* has been a central problem in the theory of fluid motion for over a century. In the present study we are concerned with the instability of viscoelastic fluids in free shear flow and in particular in the possibility that viscoelasticity may significantly affect the inviscid modes associated with inflexional velocity profiles. Important understanding of the mechanisms of vorticity production, subharmonic (pairing) instabilities, and vortex stretching has come from such studies (Morozov and Sarloos, 2007). This understanding opens the possibility of rational methods of manipulation and active control of turbulence by influencing transition mechanisms.

Examples of such manipulation include the use of time dependent motion of boundaries, modification of the properties of surfaces, including grooves and ribs, and addition of polymers and/or fibres to the flow. The nonlinearities in the equations of motion describing fluid flow can lead to the development of hydrodynamic instabilities stemming from the consideration of fluid inertial effects, Coriolis effects, buoyancy, surface tension, etc. (Sengupta, 2004). In many flows involving macromolecular liquids, hydrodynamic instabilities are observed at low flow rates that are absent in the corresponding flow of Newtonian fluids (Bird, Armstrong, and Hassager, 1987). In polymeric materials, the presence of a well defined microstructure results in a complex rheological response, which in turn affects the stability of the fluid motion. Polymeric liquids exhibit significant elastic and shear-thinning phenomena which are represented by nonlinear terms in constitutive relations that describe the state of stress in flowing polymeric materials. These viscoelastic constitutive equations are nonlinear functionals of the rate of deformation tensor, $\dot{\gamma} = (\nabla \upsilon) + (\nabla \upsilon)^t$, where $\upsilon(x,t)$ is the velocity vector. The complex interaction of nonlinear terms in the momentum equation and the constitutive equation give rise to a new class of unstable flows with a rich dynamical structure (Azaiez and Homsy, 1994a). One of the best-documented instabilities in Newtonian flows is the Taylor-Couette instability (DiPrima and Swinney, 1981). In the Taylor-Couette geometry (a fluid confined between two concentric rotating cylinders (DiPrima and Swinney, 1981; Swinney, 1988; Andereck, Liu, and Swinney, 1986)), the first nontrivial change when the outer cylinder is fixed while the inner one rotates with increasingly large rotation rate, is a sharp transition to Taylor vortex flow, induced by a linear instability of the laminar flow profile. When the rotation rate is increased even more, one rapidly encounters secondary bifurcations to more complicated flows and turbulence (Andereck, Liu, and Swinney, 1986). For counterrotating cylinders, there may even be a direct transition to turbulence, i.e., there is no intermediate regime with nontrivial coherent flow. This is consistent with the fact that in planar Couette flow (two parallel plates moving in opposite directions, with a fluid in between) the laminar flow is linearly stable for any *Re*, while a nonlinear (subcritical) transition to turbulence occurs in practice for *Re* of order 300-400 (Schmid and Henningson, 2001). After all, in the limit in which the gap is small and the cylinders counterrotate with the same rotation rate, Taylor-Couette flow approaches planar Couette flow. Likewise, the transition to turbulence in pipe flow is direct and nonlinear, although, weakly turbulent flow in this geometry still appears to be organized by coherent structures (Hof et al., 2004). The Taylor instability is characterized by the generation of streamwise vorticity and development of a steady secondary cellular structure in the axial direction, known as Taylor cells. The source of this instability is inertial motion of material elements along curved streamlines in which the centrifugal forces act to push the fluid outside its circular orbit. A similar Taylor-Couette instability occurs in the flow of non-Newtonian fluids; however, the destabilizing forces arise from nonlinear interactions between inertia, fluid shear thinning, and elasticity. Experiments with constant viscosity 'ideal elastic fluids' have demonstrated the presence of a purely elastic mode that occurs at negligibly small Reynolds numbers (Reynolds, 1883), and linear stability analyses with simple constitutive relations are able to predict this instability. Elastic instabilities also occur in more complex geometries that are not amenable to classical linear stability analyses due to the difficulties in obtaining analytical expressions or

accurate numerical solutions for their base flows. Finally, we want to reiterate the fact that unlike the Newtonian case, predictions are likely to depend upon details of the equations relating stress to shear rate. The relation between these two tensors is nonlinear and usually involves an integral or differential equation known as the constitutive equation. For a thorough discussion of the development of rheological constitutive equations for viscoelastic fluids and their application in fluid dynamics see Goddard (Goddard, 1979), Bird et al. (Bird, Armstrong, and Hassager, 1987; Bird et al., 1987) and Larson (Larson, 1988).

1.5 Industrial applications of viscoelastic instabilities

Understanding the hydrodynamic stability and transition of free shear flows of dilute polymer solutions is paramount to both the fundamental theory of viscoelastic liquids and their industrial applications, especially those arising in microfluidic mixing and viscoelastic stabilization via polymer addition. Microfluidics, (Squires and Quake, 2005) which is essentially a field dedicated to miniaturized plumbing and fluidic manipulation, offers the possibility of solving outstanding system integration issues by allowing automation to proceed to scales that will rival current electronic integrated circuits. Although most current effort in microfluidics concerns devices with applications in chemistry, biology, and medicine, there are also applications in the physical sciences for control systems and heat management, energy generation, and display technology. There is a long history of using fluidics as control systems, ranging from logic devices to thrust reversers in aircraft; this program ultimately foundered in part because scaling properties of the fluid physics prevented miniaturization. Liquid crystal displays and ink jet printers are ubiquitous consumer products that can be thought of as microfluidic devices, and have had enormous industrial impact. As fuel cells become more widely deployed, it is likely that they will ultimately incorporate some sort of microfluidic plumbing. Likewise, understanding the mechanism governing the transition to turbulence in shearing flows of viscoelastic biofluids is decisive in resolving the swelling instability transition in mucus (Sircar and Roberts, 2016a), cartilage (Sircar et al., 2015), adhesion-fragmentation transition in cells (Sircar and Bortz, 2013; Sircar, Younger, and Bortz, 2014; Sircar and Roberts, 2016b) and bending instability transition in soft tissues (Destarde, Annaidh, and Coman, 2009).

Another industrial application of viscoelastic liquids lies in the mechanism of drag reduction (DR). The reduction in turbulent friction losses by the dilute addition of high molecular weight polymers to flowing liquids has been extensively studied since the phenomenon was first observed over 60 years ago (Toms, 1948). The addition of small quantities of high molecular weight polymers to flowing liquids can produce profound effects on a wide variety of flow phenomena that appear incommensurate with a small concentration of polymers added to a solution (Graham, 2014). This is most evident in turbulent boundary layers, in which dissolving parts-per-million quantities of long-chain flexible polymers into solution can reduce turbulent friction losses by as much as 80% compared with that of the solvent alone. The corresponding effect on the character of the flow is equally impressive. The acute differences in the near-wall turbulent structure between Newtonian flow and polymer drag reduced flow can be described phenomenologically as follows: As a consequence of

the reduced wall friction, the mean velocity profile is modified and the shear in the boundary layer is redistributed. This effect alters the nature and strength of the vortices formed, resulting in a significant modification of the near-wall structure of the turbulent boundary layer. The unknown in this simple description is the lack of coupling between the near-wall turbulence and the skin friction, such that one cannot be merely a consequence of the other. It is this complexity of the near-wall turbulence dynamics, further coupled with the dynamics of dilute polymers in solution, that has made the determination of a detailed mechanism of polymer drag reduction an enigma for nearly 60 years. Drag reduction was discovered independently by Mysels and Toms during World War II and published only later (Mysels, 1949; Toms, 1949; Agoston et al., 1954). The phenomenon is sometimes called as "Toms effect", because the first public description was by Toms in 1948 (Toms, 1948) at the First International Congress on Rheology, but Mysels's observation predate those of Toms, and the terminology is inappropriate. At the very tiny polymer concentrations of interest in drag reduction, the viscosity and density of the polymer solution differ only slightly from those of the pure solvent. Nonetheless, the effect of the polymer additive is to lower the value of the friction factor at a given Reynolds number. The amount by which the friction factor is lowered is a measure of the amount of drag reduction. A number of polymer characteristics making for good drag reducers have been determined. A long-chain backbone and flexibility are important characteristics of good drag-reducing agents. For instance, of two polymers with the same molecular weight and same structural units, a linear one will be more effective than a highly branched one. Also, for two different polymers of similar configuration and the same molecular weight, the one with the lower molecular weight monomer will have the greater drag-reducing effect if both are utilized at the same weight concentration.

Researchers study polymer DR for both practical and fundamental purposes (White and Mungal, 2008). The obvious economic interest in applications as wide-ranging as crude oil transport, wastewater treatment, firefighting, and distributed heating and cooling systems, in addition to the obvious military applications, resulted in a burst of research activity. It was subsequently found that the addition of surfactants or fibers can also cause drag reduction; surfactant drag reduction is reviewed in Zakin et al. (Zakin, Lu, and Bewersdorff, 1998). The early research on drag reduction focused on how the presence of the polymer at such dilute concentrations affected the structure of the turbulence, particularly the near-wall region. There are only a few experimental studies of viscoelastic free shear flows and there is little understanding of how polymers affect either primary or secondary instability modes. Hibberd, Kwarde and Scharf (Hibberd, Kwade, and Scharf, 1982) and Riediger (Riediger, 1989) studied the effects of the addition of polymers and surfactants on the instability of the mixing layer. The results of the experimental measurements and flow visualizations show a delay in the formation of the typical structures of the plane mixing layer, i.e. roll-up and pairing. They also reveal that the presence of polymer additives leads to an enhancement of the large-scale turbulent structures and an almost complete suppression of the small-scale structures. Practical applications are pipe flows (or other internal flow geometries) and marine vehicles, although the former has had much more success with polymers than the latter. Fundamentally, studying the effects of polymers on turbulence provides valuable insight into the physics of fluid turbulence, particularly the self-sustaining mechanisms of wall turbulence. Moreover, if

a detailed understanding of the mechanics of polymer DR can be determined, it is conceivable that the effect can be reproduced by other means, such as surface modification, sensor actuation, or additives, among other strategies (**Gad2000**). Success on this front would have tremendous impact on the economics of energy propulsion and pollutant emission reduction from vehicles. Improved and expanded practical applications of polymer DR will be advanced greatly by the development of robust polymer models and drag reduced turbulence models for the large eddy simulation and Reynolds-averaged Navier-Stokes numerical simulations techniques (White and Mungal, 2008). These techniques will allow for the modeling and optimization of applications at high *Re* and in complex geometries. In addition to the experiments needed to support these efforts, detailed numerical investigations to study the effects of polymer additives in flows at high *Re*, with pressure gradients, with roughness, and with separation offer unique opportunities to provide valuable insights on the fundamental fluid physics in these complex flows.

Chapter 2

Compound Matrices: A numerical method for stiff DEs

2.1 Introduction

The most primitive way to find numerical solution of linear inhomogeneous two-point boundary-value problems for systems of ordinary differential equations is through the use of explicit shooting methods. We shall restrict our attention to "difficult" problems, by which we mean "stiff" differential systems for which the real parts of the characteristic values of the differential operator will be widely separated. A fundamental work by Conte (Conte, 1966) has clearly explained the pitfalls which may be encountered if one attempts to solve such a difficult problem by using the standard (superposition) shooting method, and there is a considerable literature devoted to devising other shooting methods which obviate these pitfalls. Perhaps the most popular of these other methods is that of orthonormalization (Godunov, 1961), a concise account of which is given in Conte's paper. Another method which has received a great deal of attention is the Riccati method, see for example (Scott, 1973). Both the orthonormalization method and the Riccati method do however have their disadvantages, with orthonormalization it is a laborious accounting feat to construct the required function, and the differential equations of the Riccati method have annoying singularities. The Riccati method is successful in overcoming the growth problem but other difficulties arise due to the singularities of the Riccati matrix R and its inverse S. If, however, an attempt is made to eliminate the singularities from the Riccati method then, as Davey (Davey, 1979) has shown, one is led directly to the use of compound matrices. Our interest in the use of compound matrices was stimulated initially by the need to overcome certain difficulties which arose in the asymptotic theory of the eigenvalue relation for the Orr-Sommerfeld problem (Lakin, Ng, and Reid, 1978). It soon became evident, however, that they also provide a simple and effective method for the numerical treatment of eigenvalue problems for stiff differential equations, especially those of hydrodynamic type which are typically of order four or six. There are many aspects of the method which clearly require further study both analytically and numerically. In this chapter, we discuss few of those aspects.

Standard iterative technique (such as the shooting techniques) for finding eigenvalues of a set of differential equations tend to be inaccurate for stiff systems. Since these technique are used to calculate eigenvalues, the converged numerical solution strongly depends on an initial estimate. Therefore, a major disadvantage of the algorithm is the necessity of providing an appropriate initial estimate to get the most

dominant eigenvalue. The accuracy can be improved dramatically by using a corresponding differential system of a compound matrix, the elements of which are the minors of the solution matrix. Further, the problem of inaccuracy in the solution can be alleviated by complementing the Compound Matrix Method with an approximate asymptotic analysis, or by calculating all the eigenvalues of a discretized problem using standard algorithms for selected parameters. For linear homogeneous eigenvalue problems with separated boundary conditions, the brilliancy of the Compound Matrix Method is that it transforms difficult (i.e., stiff) two-point boundary-value problems which cannot be solved by the standard (superposition) shooting method into initial-value problems which can be solved by the same standard shooting method because the required solutions will not be subdominant. The essence of the method is to determine the multilinear form (or wedge product) of the linearly independent solutions which satisfy the known initial conditions. The resulting Compound Matrix Method was first used by Gilbert and Backus' for elastic wave problems (Gilbert and Backus, 1966), and later by Ng and and Davey for two-point boundary value problems and eigenvalue problems of the Orr-Sommerfeld equation (Ng and Reid, 1979b). These investigations computed eigenvalues and eigenfunctions with marginal errors where standard shooting methods failed. Eigenvalue problems for ordinary differential equations are usually treated by first defining a solution matrix which satisfies certain prescribed initial conditions and the required eigenvalues are then obtained as the roots of some minor of the solution matrix. If we attempt to evaluate this minor by computing its elements separately, as in a standard shooting method, then there may be a serious loss of accuracy numerically especially when the differential equation is stiff. Davey examined the efficiency of the Compound Matrix Method compared to the orthonormalization for a standard difficult eigenvalue problem and found that the Compound Matrix Method requires about three times as many integration steps and approximately twice as much computing time as orthonormalization (Davey, 1980). This comparison was for a fourth-order problem and for higher differential orders we expect the Compound Matrix Method to require comparatively more computing time. However, the method has the important advantage that it is so easy to understand and program relative to other shooting methods for difficult problems, therefore it is an ideal method for those who are anxious to spend most of their time doing theoretical work and so wish to do their occassional computational work with the minimum of inconvenience. Another important advantage of using the Compound Matrix Method for difficult problems relative to other shooting methods is that it can be used by someone who only needs to know how to use a Runge-Kutta integration routine, all other shooting methods for difficult problems require much more knowledge. This chapter is organized as follows. In section 2.2, we discuss the different methods to solve the eigenvalue problem and in subsection 2.2.2 we introduced the Compound Matrix Method for different type of problems followed by an application of the method in section 2.3.

2.2   Mathematical Methods

We consider the following eigenvalue problem,

$$\frac{\partial \boldsymbol{\phi}}{\partial x} = A(x, \lambda)\boldsymbol{\phi}, \qquad a \leq x \leq b, \tag{2.1}$$

$$B(x, \lambda)\boldsymbol{\phi} = 0, \qquad x = a, \tag{2.2}$$

$$C(x, \lambda)\boldsymbol{\phi} = 0, \qquad x = b, \tag{2.3}$$

where A is a 2n × 2n matrix, B and C are n × 2n matrices, all being known functions of the independent variable x and a parameter λ, and $\boldsymbol{\phi}$ is a 2n-dimensional vector function ("Compound matrix method and evans function - a quick introduction"). The aim is to determine values of the parameter (eigenvalues) λ so that non-trivial solutions exist. Such eigenvalue problems feature in a variety of disciplines. For instance, it often results from a linear stability/bifurcation analysis of fluid flows (Afendikov and Bridges, 2001), solitary waves (Pego and Weinstein, 1992), and pre-stressed elastic bodies(Fu and Pour, 2002). One or both of the boundaries $x = a, b$ may be infinite.

2.2.1   Determinantal Method

This would be the first method one could think of without reading any books. The idea is to shoot from one end to the other end and to iterate on λ so that the boundary condition on the other end is satisfied. We may also shoot from both ends towards a middle point and to iterate on λ so that the two solutions coincide at the middle point. If we choose to shoot from $x = a$, then the procedure is as follows:

- Assuming that matrix B has rank n, we may then always find *n* linearly independent vectors $\boldsymbol{\phi}_0^{(1)}, \boldsymbol{\phi}_0^{(2)}, ..., \boldsymbol{\phi}_0^{(n)}$, such that

$$B(a, \lambda)\boldsymbol{\phi}_0^{(i)} = 0, \qquad i = 1, 2, ...n. \tag{2.4}$$

  Using each of these vectors as the initial value at $x = a$, we may integrate (2.1) from $x = a$ to obtain n independent solutions, say $\boldsymbol{\phi}^{(i)}(x), i = 1, 2, ..., n$.

- A general solution that satisfies (2.1) and the boundary condition (2.2) is then given by

$$\boldsymbol{\phi} = \sum_{i=1}^{n} k_i \boldsymbol{\phi}^{(i)}(\mathbf{x}) \tag{2.5}$$

  where $k_1, k_2, ..., k_n$ are arbitrary constants. We define $M(x, \lambda)$ to be the 2n× n matrix whose i$^{\text{th}}$ column is $\boldsymbol{\phi}^{(i)}$, that is

$$M(x, \lambda) = [\boldsymbol{\phi}^{(1)}, \boldsymbol{\phi}^{(2)}, ..., \boldsymbol{\phi}^{(n)}]. \tag{2.6}$$

  Equation (2.5) can then be written as

$$\boldsymbol{\phi} = M(x, \lambda)\boldsymbol{k}, \tag{2.7}$$

where $k = [k_1, k_2, ...k_n]^T$.

- On substituting (2.7) into the other boundary condition (2.3), we obtain

$$C(b, \lambda)M(b, \lambda)\boldsymbol{k} = 0. \qquad (2.8)$$

- Since $\boldsymbol{k} \neq 0$, we deduce that

$$|C(b, \lambda)M(b, \lambda)| = 0, \qquad (2.9)$$

where a pair of vertical bars denotes the determinant of the matrix enclosed. We iterate on λ so that the determinantal equation (2.9) is satisfied.

When one of the boundaries or both are infinite, it is usual to shoot from $x = a$ and from $x = b$, respectively, so that the two solutions match at a middle point, say $x = d$. Denote $\boldsymbol{\phi}^{(1)}(x), \boldsymbol{\phi}^{(2)}(x), \ldots, \boldsymbol{\phi}^{(n)}(x)$ the n solutions obtained by shooting from $x = a$ as explained above. Then again, a general solution satisfying the left boundary condition is given by

$$\boldsymbol{\phi} = \sum_{i=1}^{n} k_i \boldsymbol{\phi}^{(i)}(x) \qquad (2.10)$$

Likewise, we denote by $\boldsymbol{\phi}^{(n+1)}(x), \boldsymbol{\phi}^{(n+2)}(x), ..., \boldsymbol{\phi}^{(2n)}(x)$ the n solutions obtained by shooting from $x = b$. Then a general solution satisfying the right boundary condition is given by

$$\boldsymbol{\phi} = \sum_{i=n+1}^{2n} k_i \boldsymbol{\phi}^{(i)}(x), \qquad (2.11)$$

where $k_{n+1}, k_{n+2}, ..., k_{2n}$ are another set of n constants. The two solutions (2.10) and (2.11) must match at $x = d$. Thus,

$$\sum_{i=1}^{n} k_i \boldsymbol{\phi}^{(i)}(x) = \sum_{i=n+1}^{2n} k_i \boldsymbol{\phi}^{(i)}(x), \qquad \text{when } x = d \qquad (2.12)$$

or equivalently,

$$N(d, \lambda)c = 0, \qquad (2.13)$$

where

$$N(d, \lambda) = [\boldsymbol{\phi}^{(1)}, \boldsymbol{\phi}^{(2)}, ..., \boldsymbol{\phi}^{(n)}, \boldsymbol{\phi}^{(n+1)}, \boldsymbol{\phi}^{(n+2)}],$$
$$c = [k_1, k_2, ..., k_n, -k_{n+1}, -k_{n+2}, ..., -k_{2n}]^T \qquad (2.14)$$

We then iterate on λ so that the determinantal equation

$$|N(d, \lambda)| = 0 \qquad (2.15)$$

is satisfied. We note that whereas the $|N(d, \lambda)|$ defined above is dependent on d, or the matching point, the following quantity is independent of d,

$$D(\lambda) = e^{-\int_a^d trA(s,\lambda)ds}|N(d, \lambda)|. \qquad (2.16)$$

This may easily be proved with the aid of the properties

$$\frac{d\boldsymbol{\phi}^{(i)}}{dx} = A(x,\lambda)\boldsymbol{\phi}^{(i)}, \tag{2.17}$$

and

$$\left| A\boldsymbol{\phi}^{(1)}, \boldsymbol{\phi}^{(2)}, \ldots, \boldsymbol{\phi}^{(2n)} \right| + \left| \boldsymbol{\phi}^{(1)}, A\boldsymbol{\phi}^{(2)}, \ldots, \boldsymbol{\phi}^{(2n)} \right| + \cdots$$
$$+ \left| \boldsymbol{\phi}^{(1)}, \boldsymbol{\phi}^{(2)}, \ldots, A\boldsymbol{\phi}^{(2n)} \right| = \text{tr}A \left| \boldsymbol{\phi}^{(1)}, \boldsymbol{\phi}^{(2)}, \ldots, \boldsymbol{\phi}^{(2n)} \right| \tag{2.18}$$

The determinantal method is conceptually easy, but for large or small values of λ the eigenvalue problem usually becomes stiff and the solutions $y_{(1)}, y_{(2)}, \ldots, y_{(n)}$, although linearly independent initially at $x = a$, quickly become linearly dependent due to the dominance of exponentially growing solutions. To address this problem, the Compound Matrix Method was proposed in (Ng and Reid, 1979b; Ng and Reid, 1979a; Ng and Reid, 1985; Lindsay and rooney, 1992). Bridges (Bridges, 1999)) gave a very good differential-geometric interpretation of this method and explained why this new method works.

2.2.2   Compound Matrix Method

Here, a generalization of the Compound Matrix Method (originally proposed in (Ng and Reid, 1985)) is presented in this section to deal with the eigenvalue and the boundary-value problem involving unstable systems of ordinary differential equations. Details are given for the fourth- and the sixth-order problems. Consider a problem involving single differential equation of the form

$$\phi^{\text{IV}} - a_1 \phi''' - a_2 \phi'' - a_3 \phi' - a_4 \phi = f \tag{2.19}$$

where a_i (i= 1, 2, 3,4) and f is a complex function of x and $0 \le x \le 1$ (for example), and ϕ is required to satisfy an equal number of boundary conditions at the endpoints. The procedure outlined in (Ng and Reid, 1979b; Ng and Reid, 1979a) consists of two essential steps.

1. Rather than attempting to compute a set of linearly independent solutions of (2.19) which satisfy the boundary conditions at $x = 0$ (for example), we compute the minors of the corresponding solution matrix by a direct numerical integration of the so-called compound matrix equations which these minors satisfy.

2. We derive a second- order auxiliary differential equation the coefficients of which are some of the minors determined in the first step. The solution to the boundary-value problem is then obtained by integrating the auxiliary equation from $x = 1$ to 0 subject to the boundary conditions at $x = 1$.

Because of the effectiveness of the Compound Matrix Method in treating problems involving single equations of the Orr-Sommerfeld type, it is desirable to generalize the method to deal with other unstable differential systems, typically of order four

and six, which frequently arise in the study of hydrodynamic stability. In this connection, we note that the necessary generalization of the first step of the method for systems can readily be found in the work of (Schwarz, 1970) which gives a general algorithm for the derivation of the compound matrix equation associated with an *n*th order complex, linear system of the form

$$\boldsymbol{\phi}' = \boldsymbol{A}(x)\boldsymbol{\phi} + \boldsymbol{f} \tag{2.20}$$

In order to explain the method in detail we solve a Boundary Value problem via fourth order and a sixth order system, described next.

2.2.2.1 Fourth-Order System

Consider the linear inhomogeneous system

$$\boldsymbol{\phi}' = \boldsymbol{A}(x)\boldsymbol{\phi} + \boldsymbol{f}(x), \qquad 0 \leq x \leq 1, \tag{2.21}$$

where $\boldsymbol{A}(x)=[a_{ij}(x)]$ is a 4×4 matrix, $\boldsymbol{f}(x)=[f_j(x)]^T$ and the solution $\boldsymbol{\phi}=[\phi_j(x)]^T$ are 4×1 column vectors. We shall also suppose that the boundary conditions at $x = 0$ and $x = 1$ are given by

$$\boldsymbol{P}\boldsymbol{\phi}(0) = \boldsymbol{p}, \tag{2.22a}$$

$$\boldsymbol{Q}\boldsymbol{\phi}(1) = \boldsymbol{q}. \tag{2.22b}$$

where $\boldsymbol{P}$ and $\boldsymbol{Q}$ are 2×4 matrices of rank 2 and $\boldsymbol{p}$ and $\boldsymbol{q}$ are 2×1 column vectors. By superposition, the solution to the two-point boundary-value problem can then be written in the form,

$$\boldsymbol{\phi} = \boldsymbol{g} + \alpha\boldsymbol{u} + \beta\boldsymbol{v}, \tag{2.23}$$

where $\boldsymbol{g}$ is any solution of (2.21) which satisfies the initial condition (2.22a), while $\boldsymbol{u}$ and $\boldsymbol{v}$ are two linearly independent solutions of the homogeneous system

$$\boldsymbol{\phi}' = \boldsymbol{A}(x)\boldsymbol{\phi} \tag{2.24}$$

subject to initial condition

$$\boldsymbol{P}\boldsymbol{\phi}(0) = \boldsymbol{0} \tag{2.25}$$

The constants α and β are determined by requiring that $\boldsymbol{\phi}$ satisfies the boundary condition (2.22b) at x = 1.

Rather than attempting to compute $\boldsymbol{g}$, $\boldsymbol{u}$, and $\boldsymbol{v}$ explicitly as is the case with the other initial-value methods, the first step of the Compound Matrix Method is based on considering certain minors of the 4×3 solution matrix $\boldsymbol{\phi_0}$=[g u v] of the inhomogeneous system (2.21) and the 4x2 solution matrix $\boldsymbol{\phi}$= [u v] of the corresponding homogeneous system. We note that the six 2×2 minors of $\boldsymbol{\phi}$ are

$$y_{ij} = \begin{vmatrix} u_i & v_i \\ u_j & v_j \end{vmatrix} \tag{2.26}$$

for $i = 1, 2, 3$ and $j = i + 1., ..., 4$. In terms of these 2×2 minors, the four 3×3 minors of ϕ_0, can be written as

$$z_{ijk} = g_i y_{jk} + g_j y_{ki} + g_k y_{ij} \tag{2.27}$$

where $i = 1, 2, j = i + 1, .., 4$ and $k = j + 1., ..., 4$. For later purposes, we also note the quadratic identity

$$y_{12} y_{34} - y_{13} y_{24} + y_{14} y_{23} = 0, \tag{2.28}$$

which can readily be obtained from the Laplace expansion of the determinant

$$\begin{vmatrix} u_1 & v_1 & 0 & 0 \\ u_2 & v_2 & u_2 & v_2 \\ u_3 & v_3 & u_3 & v_3 \\ u_4 & v_4 & u_4 & v_4 \end{vmatrix} = 0 \tag{2.29}$$

If we now arrange the 2×2 minors of ϕ according to the lexicographical order of their indices to form the 6×1 vector $y = [y_{12}, y_{13}, ... y_{34}]^T$, then y is called the second compound of ϕ which can also be denoted by $C_2[\phi]$. Similarly $z = C_3[\phi_0] = [Z_{123}, Z_{124}, Z_{134}, Z_{234}]^T$ is called the third compound of ϕ_0. By a direct calculation or by using the algorithm of (Schwarz, 1970), it is easy to show that

$$y' = B(x)y, \tag{2.30}$$

where

$$\mathbf{B}(x) = \begin{bmatrix} a_{11} + a_{22} & a_{23} & a_{24} & -a_{13} & -a_{14} & 0 \\ a_{32} & a_{11} + a_{33} & a_{34} & a_{12} & 0 & -a_{14} \\ a_{42} & a_{43} & a_{11} + a_{44} & 0 & a_{12} & a_{13} \\ -a_{31} & a_{21} & 0 & a_{22} + a_{33} & a_{34} & -a_{24} \\ -a_{41} & 0 & a_{21} & a_{43} & a_{22} + a_{44} & a_{23} \\ 0 & -a_{41} & a_{31} & -a_{42} & a_{32} & a_{33} + a_{44} \end{bmatrix} \tag{2.31}$$

Similarly, z must satisfy the equation

$$z' = C(x)z + D(x)f, \tag{2.32}$$

where

$$\mathbf{C}(x) = \begin{bmatrix} a_{11} + a_{22} + a_{33} & a_{34} & -a_{24} & a_{14} \\ a_{43} & a_{11} + a_{22} + a_{44} & a_{23} & -a_{13} \\ -a_{42} & a_{32} & a_{11} + a_{33} + a_{44} & a_{12} \\ a_{41} & -a_{31} & a_{21} & a_{22} + a_{33} + a_{44} \end{bmatrix} \tag{2.33}$$

and

$$\mathbf{D}(x) = \begin{bmatrix} y_{23} & -y_{13} & y_{12} & 0 \\ y_{24} & -y_{14} & 0 & y_{12} \\ y_{34} & 0 & -y_{14} & y_{13} \\ 0 & y_{34} & -y_{24} & y_{23} \end{bmatrix} \tag{2.34}$$

Moreover, the initial conditions for y and z can easily be derived from (2.22a) and (2.25) using (2.26) and (2.27).

Suppose now that y and z have been computed by integrating (2.30) and (2.32) from x=0 to 1 subject to the appropriate initial conditions, the next step of the Compound Matrix Method requires that the solution of the boundary-value problem (2.21), (2.22) be obtained from an auxiliary second-order system. First, we note that for fixed i, j with i j, (2.23) gives

$$\phi_i - g_i = \alpha u_i + \beta v_i, \tag{2.35}$$

and

$$\phi_j - g_j = \alpha u_j + \beta v_j, \tag{2.36}$$

and hence it follows that

$$y_{ij}\alpha = (\phi_i - g_i)v_j - (\phi_j - g_j)v_i \tag{2.37}$$

and

$$-y_{ij}\beta = (\phi_i - g_i)u_j - (\phi_j - g_j)u_i \tag{2.38}$$

On substituting (2.37) and (2.38) into

$$\phi_i' - g_i' = \alpha u_i' + \beta v_i' \tag{2.39}$$

and simplifying, we have

$$y_{ij}\phi_i' = a_{i\mu}(y_{\mu j}\phi_i - y_{\mu i}\phi_j - z_{i\mu j}) + y_{ij}f_i, \tag{2.40}$$

where the summation is to be taken over μ. Moreover, on interchanging i and j in (2.36), and on noting that $y_{ij} = -y_{ji}$ and $z_{i\mu j} = -z_{j\mu i}$, we obtain

$$y_{ij}\phi_j' = a_{j\mu}(y_{\mu j}\phi_i - y_{\mu i}\phi_j - z_{i\mu j}) + y_{ij}f_j, \tag{2.41}$$

Equations (2.40) and (2.41) thus form a closed system which can be used for the determination of ϕ_i and ϕ_j by integrating backward from x= 1 to 0.

To determine the initial condition for ϕ at x =1, we rewrite (2.23) in matrix form

$$\begin{bmatrix} \phi_1 - g_1 & u_1 & v_1 \\ \phi_2 - g_2 & u_2 & v_2 \\ \phi_3 - g_3 & u_3 & v_3 \\ \phi_4 - g_4 & u_4 & v_4 \end{bmatrix} \begin{bmatrix} 1 \\ -\alpha \\ -\beta \end{bmatrix} = 0 \tag{2.42}$$

This is a linear homogeneous system with a nontrivial solution $[1, -\alpha, -\beta]^T$, Hence the determinant of any three rows of the coefficient matrix must vanish. This in turn implies that

$$\boldsymbol{D}(x)\boldsymbol{\phi}(x) = \boldsymbol{z}(x), \tag{2.43}$$

where $\boldsymbol{D}(x)$ is given by (2.34). Incidentally, we note that the derivation of (2.43) from (2.42) provides a simple algorithm for computing the matrix $\boldsymbol{D}(x)$ in (2.34). By using row reduction and the quadratic identity (2.28), it is easy to show that the

augmented matrix associated with (2.43) is of rank 2, i.e.,

$$
[\mathbf{D}|\mathbf{z}] \sim \left[\begin{array}{cc} \mathbf{D}^* & \mathbf{z}^* \\ \mathbf{0} & \mathbf{0} \end{array}\right] = \left[\begin{array}{ccccc} y_{23} & -y_{13} & y_{12} & 0 & z_{123} \\ 0 & y_{34} & -y_{24} & y_{23} & z_{234} \\ 0 & 0 & 0 & 0 & 0 \\ 0 & 0 & 0 & 0 & 0 \end{array}\right]
\tag{2.44}
$$

Clearly then the boundary conditions (2.22b) together with (2.44) form a system of four linear equations of the form

$$
\left[\begin{array}{c} \mathbf{D}^*(1) \\ \mathbf{Q} \end{array}\right] \phi(1) = \left[\begin{array}{c} \mathbf{z}^*(1) \\ \mathbf{q} \end{array}\right].
\tag{2.45}
$$

Thus $\phi(1)$ can be uniquely determined provided that

$$
det \left[\begin{array}{c} \mathbf{D}^*(1) \\ \mathbf{Q} \end{array}\right] \neq 0.
\tag{2.46}
$$

We note that this condition must be satisfied if the boundary-value problem (2.21), (2.22) is to have a unique solution. This follows from the fact, which can be verified by a direct calculation, that (2.22b) is equivalent to the condition that $det[\mathbf{Q}\phi(1)] \neq 0$, where ϕ is any solution matrix of the homogeneous system (2.24) which satisfies the homogeneous boundary conditions $\mathbf{P}\phi(0) = \mathbf{0}$.

Suppose now that ϕ_i, and ϕ_j, are computed by integrating (2.40), (2.41) from x = 1 to 0 and that the remaining two components of ϕ are obtained algebraically by solving $\mathbf{D}^*(x)\phi(x) = \mathbf{z}^*(x)$, then it is necessary to show that ϕ thus determined is the solution of the boundary-value problem (2.21), (2.22).

First, we consider (2.40) and (2.41). Using (2.43), we can rewrite (2.40) and (2.41), respectively, as

$$
y_{ij}\left(\phi_i' - a_{i\mu}\phi_\mu - f_i\right) = 0
\tag{2.47}
$$

$$
y_{ij}\left(\phi_j' - a_{j\mu}\phi_\mu - f_i\right) = 0
\tag{2.48}
$$

Second, differentiating (2.43) and noting that $\mathbf{D}' = \mathbf{CD} - \mathbf{DA}$, we obtain

$$
\mathbf{D}(\phi' - \mathbf{A}\phi - \mathbf{f}) = \mathbf{0} \qquad \text{or} \qquad \mathbf{D}^*(\phi' - \mathbf{A}\phi - \mathbf{f}) = \mathbf{0}
\tag{2.49}
$$

Equations (2.47)-(2.49) can clearly be combined to obtain

$$
\mathbf{H}(\phi' - \mathbf{A}\phi - \mathbf{f}) = \mathbf{0}
\tag{2.50}
$$

where $\mathbf{H}$ is nonsingular. Hence ϕ is a solution of (2.21) and it satisfies the initial condition(2.45). Finally, we note that the solution of the boundary-value problem (2.21), (2.22) must also satisfy the initial condition (2.45) at x =1. Hence by uniqueness, if is the solution of the initial-value problem (2.21) and (2.45) as is presently the case, then it is also a solution of the boundary-value problem (2.21), (2.22).

2.2.2.2 Sixth-Order System

Although we have restricted our discussion in subsection 2.2.2.1 to fourth-order problems, the basic ideas are quite general. In this section, we outline the corresponding results for problems involving sixth-order systems. These results, together with those presented in subsection 2.2.2.1, are therefore directly applicable to a large class of unstable boundary-value problems which frequently arise in the study of hydrodynamic stability.

To avoid repetition in our present discussion, direct reference will be made to specific equations in the previous section, but it should then be understood that the definitions of the various quantities involved must be suitably modified to deal with the sixth-order systems. For example, the coefficient matrix $\mathbf{A}(x)$ in (2.21) is now 6×6 and $\boldsymbol{f}(x)$ and $\boldsymbol{\phi}(x)$ are each 6×1 column vectors. Similarly in (2.22), $\boldsymbol{P}$ and $\boldsymbol{Q}$ are 3×6 matrices of rank 3, and $\boldsymbol{p}$ and $\boldsymbol{q}$ are 3×1 column vectors. Analogous to (2.23), we write

$$\boldsymbol{\phi} = \boldsymbol{g} + \alpha \boldsymbol{u} + \beta \boldsymbol{v} + \gamma \boldsymbol{w}, \tag{2.51}$$

where $\boldsymbol{g}$ is any solution of (2.21) which satisfies the initial condition (2.22a), while $\boldsymbol{u}$, $\boldsymbol{v}$, and $\boldsymbol{w}$ are three linearly independent solutions of (2.24), (2.25).

Consider now the solution matrices $\boldsymbol{\phi_0} = [\mathbf{g\ u\ v\ w}]$ and $\boldsymbol{\phi} = [\mathbf{u\ v\ w}]$. The twenty 3×3 minors of $\boldsymbol{\phi}$ are

$$y_{ijk} = \begin{vmatrix} u_i & v_i & w_i \\ u_j & v_j & w_j \\ u_k & v_k & w_k \end{vmatrix} \tag{2.52}$$

where $i = 1, 2, 3, 4, j = i+1 \ldots, 5$, and $k = j+1, \ldots, 6$. The fifteen 4×4 minors of $\boldsymbol{\phi_0}$, can be written as

$$z_{ijkl} = g_i y_{jkl} - g_j y_{kli} + g_k y_{lij} - g_l y_{ijk} \tag{2.53}$$

where $i = 1, 2, ..., 6, j = i+1..., 6, K = j+1...., 6$, and $l = k+1, \ldots, 6$. Moreover, by considering the Laplace expansion by complementary minors of the determinant

$$\begin{vmatrix} u_i & v_i & w_i & 0 & 0 & 0 \\ u_j & v_j & w_j & u_j & v_j & w_j \\ u_m & v_m & w_m & u_m & v_m & w_m \\ u_k & v_k & w_k & u_k & v_k & w_k \\ u_l & v_l & w_l & u_l & v_l & w_l \\ u_m & v_m & w_m & 0 & 0 & 0 \end{vmatrix} = 0 \tag{2.54}$$

we obtain 30 quadratic identities of the form

$$y_{ijm} y_{klm} - y_{ikm} y_{jlm} + y_{ilm} y_{jkm} = 0 \tag{2.55}$$

where $m = 1., ..., 6; i, j, k, l \neq m; 1 \leq i < j < k < l \leq 6$. If we let $\mathbf{y} = C_3[\boldsymbol{\phi}] = [y_{123}, y_{124}, ..., y_{456}]^T$ and $\mathbf{z} = C_4[\boldsymbol{\phi_0}] = [z_{1234}, z_{1235}, ..., z_{3456}]^T$, then $\mathbf{y}$ and $\mathbf{z}$ satisfy the compound matrix equations (2.30) and (2.32), respectively. Corresponding to (2.40) and (2.41), we now have the auxiliary system

$$y_{ijk} \phi'_i = a_{i\mu} \left(y_{\mu jk} \phi_i - y_{\mu ik} \phi_j + y_{\mu ij} \phi_k - z_{i\mu jk} \right) + y_{ijk} f_i \tag{2.56}$$

$$y_{ijk}\phi'_j = a_{j\mu}\left(y_{\mu jk}\phi_i - y_{\mu ik}\phi_j + y_{\mu ij}\phi_k - z_{i\mu jk}\right) + y_{ijk}f_j \tag{2.57}$$

$$y_{ijk}\phi'_k = a_{k\mu}\left(y_{\mu jk}\phi_i - y_{\mu ik}\phi_j + y_{\mu ij}\phi_k - z_{i\mu jk}\right) + y_{ijk}f_k \tag{2.58}$$

Furthermore, by using the quadratic identities (2.55) and after a somewhat lengthy calculation, we can show that the augmented matrix $[\boldsymbol{D}(x)|\boldsymbol{z}(x)]$ is of rank 3, i.e.,

$$[\mathbf{D}|\mathbf{z}] \sim \begin{bmatrix} \mathbf{D}^* & \mathbf{z}^* \\ 0 & 0 \end{bmatrix} = \begin{bmatrix} y_{234} & -y_{134} & y_{124} & -y_{123} & 0 & 0 & z_{1234} \\ 0 & y_{345} & -y_{245} & y_{235} & -y_{234} & 0 & z_{2345} \\ 0 & 0 & y_{456} & -y_{356} & y_{346} & -y_{345} & z_{3456} \\ 0 & 0 & 0 & 0 & 0 & 0 & 0 \\ \vdots & \vdots & \vdots & \vdots & \vdots & \vdots & \vdots \\ 0 & 0 & 0 & 0 & 0 & 0 & 0 \end{bmatrix}$$
$$\tag{2.59}$$

Clearly then the initial condition for $\boldsymbol{\phi}$ at x=1 can be uniquely determined using (2.45). Thus once **y** and **z** have been computed by integrating (2.30)- (2.32) from x=0 to 1, the solution $\boldsymbol{\phi}$ can be obtained by integrating (2.56)- (2.58) backward from x = 1 to 0. Moreover, as in the fourth-order case, we can show that $\boldsymbol{\phi}$ is indeed the solution of the sixth-order boundary-value problem (2.21), (2.22).

2.2.3   Eigenvalue Problems and Their Adjoints

Consider the linear eigenvalue problem defined by

$$\boldsymbol{\phi}' = \mathbf{A}(x,\lambda)\boldsymbol{\phi}, \quad 0 \le x \le 1 \tag{2.60}$$

and

$$P\phi(0) = \mathbf{0}, \tag{2.61a}$$
$$Q\,\phi(1) = \mathbf{0}. \tag{2.61b}$$

where $\mathbf{A}(x,\lambda)$ is a 2r x 2r matrix, **P** and **Q** are r x 2r matrices of rank r, $\boldsymbol{\phi}$ is a 2r x 1 vector and λ is the eigenvalue parameter. Depending on whether r=2 or 3, Eqs (2.60), (2.61) defines a fourth- or sixth-order problem. We let **y** be the rth-compound of the $2r \times r$ solution matrix $\boldsymbol{\phi}$ of (2.60) which satisfies the boundary condition (2.61a) at x =0. Clearly then **y** must satisfy the compound matrix equation

$$\mathbf{y}' = \boldsymbol{B}(x,\lambda)\mathbf{y} \tag{2.62}$$

where the matrix $\mathbf{B}(x,1)$ can be derived from $\mathbf{A}(x,\lambda)$ as discussed in section 2.2.2. By using the rule that the compound of the product of two matrices is equal to the product of their compounds, it then follows from (2.61b) that

$$C_r[\mathbf{Q}\boldsymbol{\Phi}(\mathbf{1})] = C_r[\mathbf{Q}] \cdot C_r[\boldsymbol{\Phi}(1)] = 0 \tag{2.63}$$

Equation (2.63) is the appropriate eigenvalue relation for (2.60), (2.61) and it is equivalent to requiring that a certain linear combination of the elements of **y** vanish

at x =1. Thus to determine the eigenvalue, we can repeatedly integrate the compound matrix equation (2.62) from x =0 to 1, while a Newton-type iteration scheme is used to vary λ until the eigenvalue relation (2.63) is satisfied. Next we note that $\boldsymbol{\phi}$ must also satisfy the auxiliary systems (2.40), (2.41) or (2.56)-(2.58) with $\mathbf{z}$=0 and $\mathbf{f}$=0. The initial condition for $\boldsymbol{\phi}$ at x=1 can be obtained in the same manner as discussed in section 2.2. Thus, once we have computed the eigenvalue, we can obtain $\boldsymbol{\phi}$ by integrating (2.40), (2.41) or (2.56)-(2.58) from x=1 to 0. Moreover, using an argument identical to the one used for boundary-value problems, we can show that $\boldsymbol{\phi}$ is indeed an eigenfunction of (2.60), (2.61). Now, consider the adjoint problem of (2.60), (2.61) consisting of the system

$$\boldsymbol{\phi}^{\dagger\prime} = -\mathbf{A}^H(x,\lambda)\boldsymbol{\phi}^{\dagger} \qquad (2.64)$$

and the adjoint boundary conditions

$$\boldsymbol{\Phi}^H(0)\boldsymbol{\phi}^{\dagger}(0) = 0, \qquad (2.65a)$$
$$\boldsymbol{\Phi}^H(1)\boldsymbol{\phi}^{\dagger}(1) = 0. \qquad (2.65b)$$

where the superscript H denotes the conjugate transpose, and $\boldsymbol{\phi}$ is the solution matrix of (2.60) which satisfies the boundary condition (2.61a). To obtain the adjoint eigenfunction $\phi^{\dagger}$, we may, of course, follow the same procedure for solving (2.60), (2.61) and first integrate the compound matrix system associated with (2.64), i. e.,

$$\mathbf{y}^{\dagger\prime} = -\mathbf{B}^H(x,\lambda)\mathbf{y}^{\dagger} \qquad (2.66)$$

from x =0 to 1. Here $\mathbf{y}^{\dagger}$ denotes the rth compound of the $2r \times r$ solution matrix $\boldsymbol{\phi}^{\dagger}$ of (2.64) which satisfies the boundary condition(2.65a). Once we have computed $\mathbf{y}^{\dagger}$ for $O \leq x \leq 1$, the adjoint eigenfunction $\boldsymbol{\phi}^{\dagger}$ can be obtained by integrating the appropriate auxiliary system from x = 1 to 0, except that the elements of$\mathbf{y}$ in these systems must now be replaced by the corresponding elements of $\mathbf{y}^{\dagger}$. On the other hand, the above procedure can be simplified and the need for integrating(2.66) can be circumvented on noting that a simple equivalence relation exists between the elements of $\mathbf{y}$ and $\mathbf{y}^{\dagger}$. For the purpose of the present discussion, we first assume that the matrix $\mathbf{A}$ is in normal form, i.e., the diagonal elements of $\mathbf{A}$ are all zero. It then follows that b_{ij}=0. By a straightforward but somewhat tedious calculation, it can be verified that

$$\mathbf{y}^{\dagger} = \boldsymbol{T}\mathbf{y}^* \qquad (2.67)$$

where $\mathbf{y}^*$ is the complex conjugate of $\mathbf{y}$, and $\mathbf{T}$ is a constant antidiagonal matrix of the form

$$\mathbf{T} = \begin{bmatrix} 0 & & t_{1n} \\ & \cdots & \\ t_{n1} & & 0 \end{bmatrix} \qquad (2.68)$$

For fourth-order (r= 2) problems, $\mathbf{T}$ is 6x6 and

$$\text{antidiag } \mathbf{T} = [t_{16}, \ldots, t_{61}] = [1, -1, 1, 1, -1, 1] \qquad (2.69)$$

Similarly for sixth-order (r = 3) problems, $\mathbf{T}$ is 20 x 20 and

$$\text{antidiag } \mathbf{T} = [1, -1, 1, -1, 1, -1, 1, 1, -1, 1, -1, 1, -1, -1, 1, -1, 1, -1, 1, -1] \tag{2.70}$$

Now, consider the case where the coefficient matrix $\mathbf{A}$ is not in normal form. We then let $N = AA^T\Lambda$, where $\Lambda = \text{diag } \mathbf{A}$ and

$$\boldsymbol{\phi} = \mathbf{E}\widehat{\boldsymbol{\phi}} \quad \text{where} \quad \mathbf{E} = \mathbf{E}(x) = \exp\left[\int_0^x \Lambda dx\right] \tag{2.71}$$

Then (2.60) becomes

$$\hat{\boldsymbol{\phi}}' = \left(\mathbf{E}^{-1}\mathbf{N}\mathbf{E}\right)\hat{\boldsymbol{\phi}} \tag{2.72}$$

where $E^{-1}NE$ is a matrix whose diagonal elements are zero. Corresponding to (2.61), we have

$$\mathbf{P}\hat{\boldsymbol{\phi}}(0) = \mathbf{0} \quad \text{and} \quad [\mathbf{Q}\mathbf{E}(1)]\hat{\boldsymbol{\phi}}(1) = \mathbf{0} \tag{2.73}$$

It is easy to show that $\boldsymbol{\phi}^\dagger = (\mathbf{E}^*)^{-1}\widehat{\boldsymbol{\phi}}^\dagger$, where $\mathbf{E}^*$ is the complex conjugate of $\mathbf{E}$ and $\hat{\boldsymbol{\phi}}^+$ is the adjoint eigenfunction of (2.72), (2.73). Thus if we let $\boldsymbol{\Phi}$ and $\tilde{\boldsymbol{\Phi}}$ be, respectively, the solution matrices of (2.60) and (2.72) which satisfy the boundary conditions (2.61a) and (2.73), and $\boldsymbol{\Phi}^\dagger$ be the solution matrix of the corresponding adjoint problem, then

$$\boldsymbol{\Phi} = \mathbf{E}\hat{\boldsymbol{\Phi}} \quad \text{and} \quad \boldsymbol{\Phi}^\dagger = (\mathbf{E}^*)^{-1}\hat{\boldsymbol{\Phi}}^\dagger \tag{2.74}$$

By taking the rth compounds of Eqs. (2.74), we obtain

$$\mathbf{y} = C_r(\mathbf{E})\hat{\mathbf{y}} \quad \text{and} \quad \mathbf{y}^\dagger = C_r\left[(\mathbf{E}^*)^{-1}\right]\hat{\mathbf{y}}^\dagger \tag{2.75}$$

where $\hat{\mathbf{y}} = C_r(\hat{\boldsymbol{\Phi}})$ and $\hat{\mathbf{y}}^\dagger = C_r\left(\hat{\boldsymbol{\Phi}}^\dagger\right)$. since $\hat{\mathbf{y}}^\dagger = \mathbf{T}\hat{\mathbf{y}}^*$, it follows from (2.75) that

$$\mathbf{y}^\dagger = C_r\left[(\mathbf{E}^*)^{-1}\right]\mathbf{T}C_r\left[(\mathbf{E}^*)^{-1}\right]\mathbf{y}^* = [w(x)]^{-1}\mathbf{T}\mathbf{y}^* \tag{2.76}$$

where

$$w(x) = \exp\left[\int_0^x \text{tr}\left(\mathbf{A}^H\right) dx\right] \tag{2.77}$$

Thus, once we have obtained $\mathbf{y}$ by integrating (2.62), $\mathbf{y}^\dagger$ can be obtained from (2.69), (2.70) and (2.76), (2.77) with little further computation. Moreover, when these results are applied to the actual computation of the adjoint eigenfunction, it is not necessary to evaluate w(x). This is due to the fact that in replacing the elements of y in the auxiliary systems (2.40), (2.41) or (2.56)-(2.58) by the appropriate elements of $\mathbf{y}^\dagger$, an overall multiplicative factor of $\mathbf{y}^\dagger$ (i.e., w(x)) can clearly be omitted.

We note that in most weakly nonlinear theories of hydrodynamic stability, it is often necessary to solve first an eigenvalue problem which governs the linear stability, and then a sequence of inhomogeneous boundary-value problems. For unique solutions to exist for these problems, it is necessary to require that their inhomogeneous terms be orthogonal to the adjoint eigenfunction of the linear stability theory. This in

turn provides the various conditions needed for the systematic determination of the Landau constants in the Landau amplitude equation. An application of the procedure outlined in this section for computing the adjoint eigenfunction can therefore lead to a simplification of some aspects of non-linear stability calculations.

2.2.4 Linear Boundary Value Problem

To illustrate the basic ideas involved, consider the linear fourth-order equation

$$L(\phi) = \phi^{IV} - a_1\phi''' - a_2\phi'' - a_3\phi' - a_1\phi = 0 \tag{2.78}$$

where a_1, a_2, a_3, and a_4 are functions of x and $0 \leq x \leq 1$. To be definite, we shall also suppose that the boundary conditions at x = 0 are $\phi = \phi' = 0$. The boundary conditions at x = 1, however, need not be specified until later. For the present purposes it is convenient to rewrite (2.78) as a system of first-order equations. Thus, if we let $\phi = [\phi, \phi', \phi'', \phi''']^T$ then (2.78) becomes

$$\phi' = A(x)\phi, \tag{2.79}$$

where

$$\mathbf{A}(x) = \begin{bmatrix} 0 & 1 & 0 & 0 \\ 0 & 0 & 1 & 0 \\ 0 & 0 & 0 & 1 \\ a_4 & a_3 & a_2 & a_1 \end{bmatrix} \tag{2.80}$$

Now let ϕ_1 and ϕ_2 be two solutions of (2.78) which satisfy the initial conditions

$$\phi_1(0) = [0,0,1,0]^T \quad \text{and} \quad \phi_2(0) = [0,0,0,1]^T \tag{2.81}$$

and consider 4 x 2 solution matrix

$$\mathbf{\Phi} = \begin{bmatrix} \phi_1 & \phi_2 \\ \phi_1' & \phi_2' \\ \phi_1'' & \phi_2'' \\ \phi_1''' & \phi_2'' \end{bmatrix} \tag{2.82}$$

The 2 x 2 minors of the matrix 4, are

$$\begin{array}{ll} y_1 = \phi_1\phi_2' - \phi_1'\phi_2, & y_4 = \phi_1'\phi_2'' - \phi_1'\phi_2' \\ y_2 = \phi_1\phi_2'' - \phi''\phi_2, & y_5 = \phi_1'\phi_2'' - \phi_1''\phi_2' \\ y_3 = \phi_1\phi_2''' - \phi_1''\phi_2, & y_6 = \phi''\phi_2''' - \phi_1''\phi_2'' \end{array} \tag{2.83}$$

and they satisfy the quadratic identity (Davey, 1979),

$$y_1 y_6 - y_2 y_5 + y_3 y_4 = 0 \tag{2.84}$$

By using the general theory given in (Gilbert and Backus, 1966) or by a direct calculation it is easy to show that $\mathbf{y} = [y_1, ..., y_6]^T$ satisfies the equation

$$\mathbf{y}' = \mathbf{B}(x)\mathbf{y}, \tag{2.85}$$

where

$$\mathbf{B}(x) = \begin{bmatrix} 0 & 1 & 0 & 0 & 0 & 0 \\ 0 & 0 & 1 & 1 & 0 & 0 \\ a_3 & a_2 & a_1 & 0 & 1 & 0 \\ 0 & 0 & 0 & 0 & 1 & 0 \\ -a_4 & 0 & 0 & a_2 & a_1 & 1 \\ 0 & -a_4 & 0 & -a_3 & 0 & a_1 \end{bmatrix} \tag{2.86}$$

Thus $\mathbf{y}$ is the second compound of $\boldsymbol{\phi}$ and it satisfies the initial condition

$$\mathbf{y}(0) = [0,0,0,0,0,1]^T \tag{2.87}$$

The boundary conditions on ϕ at x = 1 will imply that some element of y or, more generally, a linear combination of the elements of y must vanish there and this condition will provide the required eigenvalue relation. In actual calculations, of course, some iterative procedure must be used to vary the eigenvalue parameter until this condition is satisfied to some prescribed degree of accuracy.

Once the required eigenvalue has been obtained by the method just described, we can then proceed to the determination of the corresponding eigenfunction ϕ (for example). Clearly there must exist constants λ and μ such that

$$\phi = \lambda \phi_1 + \mu \phi_2, \quad \phi' = \lambda \phi_1' + \mu \phi_2'$$
$$\phi'' = \lambda \phi_1'' + \mu \phi_2'', \quad \phi''' = \lambda \phi_1''' + \mu \phi_2''' \tag{2.88}$$

The constants λ and μ can be eliminated from these equations in four different ways and if this is done then we obtain

$$y_1 \phi'' - y_2 \phi' + y_4 \phi = 0 \tag{2.89}$$

$$y_1 \phi''' - y_3 \phi' + y_5 \phi = 0 \tag{2.90}$$

$$y_2 \phi''' - y_3 \phi'' + y_6 \phi = 0 \tag{2.91}$$

and

$$y_4 \phi''' - y_5 \phi'' + y_6 \phi' = 0 \tag{2.92}$$

Thus we have four possible equations for the determination of the eigenfunction ϕ. Consider first the behavior of the solutions of Eqs. (2.89)-(2.92) near x = 0. For this purpose we observe that as $x \to 0$ we have

$$y_1 \sim \tfrac{1}{12}x^4, \quad y_2 \sim \tfrac{1}{3}x^3, \quad y_3 \sim \tfrac{1}{2}x^2$$
$$y_4 \sim \tfrac{1}{2}x^2, \quad y_5 \sim x, \quad y_6 \sim 1 \tag{2.93}$$

and this limiting behavior is seen to be independent of the coefficients in (2.78). The point x = 0 is therefore a regular singular point of Eqs. (2.89)-(2.92) and at that point they have exponents (2, 3), (-1/2, 2, 3), (-4, 2, 3), and (0,2, 3) respectively. It is easy to show, however, as a consequence of (2.85), that none of the solutions contains logarithmic terms. Accordingly, near x = 0 the solution of Eqs. (2.89)-(2.92) that

satisfies the boundary conditions must be of the form

$$\phi(x) = \sum_{s=0}^{\infty} b_s x^{s+2} \tag{2.94}$$

where b_0, and b_1 are arbitrary. When Eq. (2.78) is even moderately stiff, however, forward integration of Eqs. (2.89)-(2.92) from x = 0 to 1 leads, as might have been expected, to a serious growth problem. To avoid this growth problem, consider the possibility of determining $\phi(x)$ by integrating one of Eqs. (2.89)-(2.92) backwards from x = 1 to 0. For illustrative purposes we shall suppose that $\phi'(1) = \phi'''(1) = 0$ as these are the relevant boundary conditions for the Orr-Sommerfeld problem which will be discussed later. In all cases it is convenient to fix the normalization of the solution so that $\phi(1) = 1$ and, for the present discussion, we shall assume that $y_1(x)$ does not vanish anywhere in the interval $0 \le x \le 1$. For Eq. (2.89) the initial conditions are $\phi(1) = 1$ and $\phi'(1) = 0$, and (2.89) then shows that $\phi'''(1)$ vanishes automatically. On integrating Eq. (2.89) from x = 1 to 0, we see that ϕ must necessarily satisfy the boundary conditions at x = 0 since the exponents of (2.89) at x = 0 are 2 and 3. Thus we have a simple marching problem for the determination of ϕ. This procedure, however, will fail to yield the final values at x = 0 since (2.89) is singular there, but this is only a very minor limitation. For Eqs. (2.90)- (2.92) the initial conditions are $\phi = 1$, $\phi'(1) = 0$ and $\phi''(1) = -y_4(1)/y_1(1)$. On integrating these equations from x = 1 to 0, however, some numerical difficulties would be expected due to the exponents -2, -1/2, and 0 of the equations, respectively, at x = 0. These difficulties, which are particularly severe in the case of (2.90), have been confirmed by actual calculations on the Orr-Sommerfeld problem. It remains to be shown, however, that the solution of Eq. (2.89) obtained in this way is also a solution of Eq. (2.78). For this purpose let

$$z_1 = y_1 \phi'' - y_2 \phi' + y_4 \phi \tag{2.95}$$

$$z_2 = y_1 \phi''' - y_3 \phi' + y_5 \phi \tag{2.96}$$

$$z_3 = y_2 \phi''' - y_3 \phi'' + y_6 \phi \tag{2.97}$$

$$z_4 = y_4 \phi''' - y_5 \phi'' + y_6 \phi' \tag{2.98}$$

A short calculation then shows that

$$z_1' = z_2 \tag{2.99}$$

$$z_2' = a_2 z_1 + a_1 z_2 + z_3 + y_1 L(\phi) \tag{2.100}$$

$$z_3' = -a_3 z_1 + a_1 z_3 + z_4 + y_2 L(\phi) \tag{2.101}$$

$$z_4' = a_4 z_1 + a_1 z_4 + y_4 L(\phi) \tag{2.102}$$

Suppose now that (2.89) holds, i.e., that $z_1 = 0$. Then $z_2 = 0$ from (2.99) and Eqs. (2.100)-(2.102) reduce to

$$0 = z_3 + y_1 L(\phi) \tag{2.103}$$

$$z_3' = a_1 z_+ + z_4 + y_2 L(\phi) \tag{2.104}$$

$$z_4' = a_1 z_4 + y_4 L(\phi) \tag{2.105}$$

With ϕ determined from (2.89) as described above, it can then be shown from (2.97) and (2.98) that $z_3(1) = z_4(1) = 0$. Elimination of $L(\phi)$ from Eqs. (2.103)- (2.105) then gives a pair of first-order equations for z_3 and z_4 , and the only solution of these equations which satisfies the initial conditions is the trivial one. Thus $L(\phi) = 0$ and the solution of (2.89) is indeed the required eigenfunction. An alternative to the method just described would be to define the solution matrix (2.82) with respect to the boundary condition at x = 1. In this approach, with $\phi'(1) = \phi'''(1) = 0, \phi_1$ and ϕ_2 would be required to satisfy the initial conditions

$$\phi_1(1) = [1,0,0,0]^T \quad \text{and} \quad \phi_2(1) = [0,0,1,0]^T \tag{2.106}$$

The eigenvalue of the problem is then obtained by integrating (2.85) backwards, subject to the initial condition

$$\mathbf{y}(1) = [0,1,0,0,0,0]^T \tag{2.107}$$

and by requiring that $y_1(0) = 0$. We also note that as $x \to 1$ we have

$$
\begin{array}{lll}
y_1 \sim x - 1, & y_2 \sim 1, & y_3 \sim a_2(1)(x-1) \\
y_4 \sim -\frac{1}{3} a_4(1)(x-1)^3, & y_5 \sim -a_4(1)(x-1)^2, & y_6 \sim -a_4(1)(x-1)
\end{array} \tag{2.108}
$$

and hence x = 1 is a regular singular point of (2.89) and (2.92) but it is an ordinary point of (2.90) and (2.91). To obtain the eigenfunction we must now integrate forward from x = 0 to 1 to avoid the growth problem and, for this purpose, Eq. (2.91) would appear to be the best choice since x = 0 and 1 are both ordinary points of this equation. The initial conditions are $\phi(0) = \phi'(0)$ and $\phi''(0) = 1$ (for example). An argument similar to the one given above then shows that the solution obtained in this way is also a solution of (2.78) and that ϕ' and ϕ''' both vanish automatically at x = 1. The eigenfunction ϕ can then be renormalized, if desired, so that $\phi(1) = 1$.

2.3   An Application

The Orr-Sommerfeld equation, which governs the linear stability of parallel shear flows, is given by

$$\boldsymbol{\phi}' = A\boldsymbol{\phi} \tag{2.109}$$

where

$$\boldsymbol{\phi} = \left[\phi, \phi', \phi'', \phi'''\right]^T, \quad \mathbf{A} = \begin{bmatrix} 0 & 1 & 0 & 0 \\ 0 & 0 & 1 & 0 \\ 0 & 0 & 0 & 1 \\ a_{41} & 0 & a_{43} & 0 \end{bmatrix} \qquad (2.110)$$

with $a_{41} = -\left\{\alpha^4 + i\alpha R\left[\alpha^2(U-c)+U''\right]\right\}$ and $a_{43} = 2\alpha^2 + i\alpha R(U-c)$. Here ϕ is the amplitude of the disturbance stream function, U(x) is the mean velocity distribution, α and R are real parameters and c is (possibly complex) eigenvalue parameter. For plane Poiseuille flow on the interval $0 < x < 2$, we have $U(x) = x(2-x)$. If we consider only symmetric modes then the problem can be studied on the interval $0 \leq x \leq 1$ with boundary conditions

$$\phi(0) = \phi'(0) = 0, \qquad (2.111a)$$
$$\phi'(1) = \phi'''(1) = 0. \qquad (2.111b)$$

Now, we need only note that the eigenfunction ϕ satisfies the second-order auxiliary equation

$$y_1 \phi'' - y_2 \phi' + y_4 \phi = 0 \qquad (2.112)$$

where y_1, y_2 and y_4 are elements of the second compound y of the 4x 2 solution matrix of (2.109) which satisfies the homogeneous boundary condition at x = 0. In the notation of section 5.3, $y_1 := y_{12}, y_2 = y_{13}$ and $y_4 = y_{23}$. It is also convenient to rewrite $\phi, y_2/y_1$ and y_4/y_1 in terms of their real and imaginary parts, i.e.,

$$\phi = \phi_r + i\phi_i, \quad y_2/y_1 = s_r + is_i, \quad y_4/y_1 = t_r + it_i \qquad (2.113)$$

Equation (2.112) then becomes

$$\begin{bmatrix} \phi_r \\ \phi_i \\ \phi_r' \\ \phi_i' \end{bmatrix} = \begin{bmatrix} 0 & 0 & 1 & 0 \\ 0 & 0 & 0 & 1 \\ -t_r & t_i & s_r & -s_i \\ -t_i & -t_r & s_i & s_r \end{bmatrix} \begin{bmatrix} \phi_r \\ \phi_i \\ \phi_r' \\ \phi_i' \end{bmatrix} \qquad (2.114)$$

Consider now the so-called Reynolds stress function $\phi_r \phi_i' - \phi_r' \phi_i$. Differentiating and then using (2.114), we have

$$\left(\phi_r \phi_i' - \phi_r' \phi_i\right)' = s_r \left(\phi_r \phi_i' - \phi_r' \phi_i\right) + s_i \left(\phi_r \phi_r' + \phi_i \phi_i'\right) - t_i \left(\phi_r^2 + \phi_i^2\right) \qquad (2.115)$$

If we now define

$$\begin{matrix} \tau_1 = \phi_r \phi_i' - \phi_r' \phi_i, & \tau_2 = \phi_r \phi_r' + \phi_i' \phi_i \\ \tau_3 = \phi_r^2 + \phi_i^2, & \tau_4 = \phi_r'^2 + \phi_i'^2 \end{matrix} \qquad (2.116)$$

then it is easy to show that

$$\begin{bmatrix} \tau_1 \\ \tau_2 \\ \tau_3 \\ \tau_4 \end{bmatrix}' = \begin{bmatrix} s_r & s_i & -t_i & 0 \\ -s_i & s_r & -t_r & 1 \\ 0 & 2 & 0 & 0 \\ -2t_i & -2t_r & 0 & 2s_r \end{bmatrix} \begin{bmatrix} \tau_1 \\ \tau_2 \\ \tau_3 \\ \tau_4 \end{bmatrix} \qquad (2.117)$$

Moreover, if we fix the normalization so that $\phi(1) = 1$ (say), the boundary conditions (2.111b) give

$$\tau_1(1) = \tau_2(1) = \tau_4(1) = 0 \quad \text{and} \quad \tau_3(1) = 1 \tag{2.118}$$

Equations (2.117), (2.118) thus show that once we have determined the eigenvalue c and obtained y by integrating the appropriate compound matrix system which y satisfies, then $\mathbf{t}=[\tau_1, \tau_2, \tau_3, \tau_4]^T$ can be obtained directly by integrating (2.117) from x=1 to 0 without having first to compute ϕ. To test the effectiveness of this approach, we have computed τ using (2.117) for the eigenmode corresponding to

$$\alpha = 1, \quad R = 10^5, \quad \text{and} \quad c = 0.2375 + 0.0037i \tag{2.119}$$

The results we obtained for the Reynolds stress distribution $\mathbf{t}$ were found to be in excellent agreement with previous results (Drazin and Reid, 2004).

2.4   Conclusion

The Compound Matrix Method is a very efficient numerical method at large wavenumbers, where the standard shooting techniques fail or do not provide accurate results. Since it is essential to study linear stability over a wide range of wavenumbers for ascertaining the stability of the flow at those wavenumbers, this method is well-suited for linear stability analysis. At present the Compound Matrix Method is widely used to calculate the Evans function (Gubernov et al., 2003; Allen and Bridges, 2002), which is now a standard tool in spectral theory for calculating the unstable eigenvalues of the linear differential operators. More applications of the Compound Matrix Method for the solving Orr- Sommerfeld equation for high wave numbers are available (Sengupta, 1992). The Orr-Sommerfeld equation is an important equation in the area of hydrodynamics (Drazin and Reid, 2004). It is also an example of a stiff equation which requires orthogonalization to be undertaken to maintain the linear independence of the solutions. Solution of the Orr- Sommerfeld equation is difficult because of parasitic error growth and the Compound Matrix Method resolves this by reformulating the problem in a new set of variables. However, parasitic error also arises in the Compound Matrix Method when the wave number or Reynolds number is sufficiently high. In particular, the problem of evaluating the eigenfunctions become difficult. It is shown that by using the appropriate equation of the Compound Matrix Method one can avoid the problem of obtaining the spectral solution for large wave numbers. In Chapter-4 and Chapter-5, we highlight two more applications of the Compound Matrix Method, which form the core of this thesis.

Chapter 3

Local Instabilities In Free Shear Flows

3.1   Introduction

In many flows of interest, the mean-velocity profile is nonuniform in the streamwise direction, and in order to distinguish between local and global instability properties, it is first essential to assume that streamwise variations of the mean flow are slow over a typical instability wavelength. The terms "local" and "global" then refer to the instability of the local velocity profile and of the entire flow field, respectively. In this chapter, we will further characterize the local impulse response of the system within the parallel-flow approximation at each streamwise station.

First, it is appropriate to briefly recall the classical hydrodynamic instability description of open flows. Since several spatially developing shear flows are known to be extremely sensitive to external noise, many controlled experiments have been conducted to determine their response to different excitation frequencies. As a result, it has been customary to represent the downstream development of vortical structures as a collection of spatially growing instability waves of various frequencies (refer (Ho and Huerre, 1984) for a review of such analyses applied to mixing layers). In other words, experimental observations have, in general, been compared with the results of local spatial stability calculations (with given real frequency and unknown complex wave number) performed on the measured time-averaged mean velocity profile at each streamwise station. Such an approach has been reasonably successful in describing the evolution of vortices in forced experiments. For examples of this type of analysis, the reader is referred to (Crighton and Gaster, 1976) and (gaster, Kit, and Wygnanski, 1985) among many other similar studies. A large part of the hydrodynamic stability literature, however, has been devoted to temporal theory (with given real wave number and unknown complex frequency), where it is implicitly assumed that the flow develops from some given initial state. The following question may then be asked: What is the fundamental reason for adopting a spatial theory point of view in many open shear flows? It is argued here that the notions of local "absolute/convective" instability provide a rigorous justification for selecting spatial theory in specific open flows (homogeneous mixing layers, flat-plate wakes, uniform-density jets). More interestingly, application of these concepts to other open flows (bluffbody wakes, heated jets) leads to the conclusion that local spatial theory in the strict sense (real frequency) is not appropriate. Wave number

and frequency both need to be considered complex, and a global temporal instability may arise whereby the entire nonparallel mean flow admits self-sustained global modes with well-defined complex frequencies.

The impact of such concepts on the study of fluid-mechanical instabilities appears to be of much more recent origin. A spatio-temporal description of Tollmien-Schlichting wave packets in boundary layers was developed early on by (gaster, Kit, and Wygnanski, 1985), and a general formal methodology was proposed without explicitly introducing a definite distinction between the absolute or convective nature of the instability mechanism. The technique advocated by (Briggs, 1964) has been repeatedly implemented to analyze the receptivity of compressible shear flows to acoustic forcing. In geophysical fluid dynamics, (Thacker, 1976) and (Merkine, 1977) have determined the transition from absolute to convective instability in a two-layer model of the baroclinic instability. But, it is mostly in the last few decades that these issues have come to the foreground in the description of hydrodynamic instabilities in spatially evolving shear flows. The distinction between absolute and convective instabilities appears to have first been brought out in a general context in (Twiss, 1952) and (Landau and Lifshitz, 1959). It should be emphasized that plasma physicists have made extensive and seminal contributions to the theoretical foundations underlying these notions, and that they have applied them to the study of numerous plasma instabilities. For systematic developments of the main ideas, the reader is referred to the work of (Sturrock, 1958), (Briggs, 1964) and (Lifshitz and Pitaevskii, 1981).The complete and lucid review of Bers (Bers, 1983) is particularly recommended for an up-to-date account of theoretical efforts in the description of spatio-temporal plasma instabilities. The topic of absolute / convective instabilities has found its way into the mainstream of the plasma-physics literature: Presentations of the main ideas have appeared in the books by (Clemmow and Dougherty, 1969).

Local/global and absolute/convective instability concepts provide the necessary theoretical framework to classify different open shear flows according to the qualitative nature of their dynamical behavior. For instance, if the localized disturbances spread upstream and downstream and contaminate the entire parallel flow, the velocity profile is said to be locally absolutely unstable. Shear flows that are locally convectively unstable everywhere (e. g., mixing layers, flat-plate wakes) essentially display extrinsic dynamics, which is in contrast to the shear flows with a pocket of absolute instability of sufficiently large size (e. g., bluff-body wakes, hot or low-density jets) which displays intrinsic dynamics of the same nature as in closed-flow systems. Fluid particles are still advected downstream, but temporally growing global modes may be present. These flows behave as oscillators: The evolution of vortices does not rely on the spatial amplification of external perturbations but rather on the growth of initial disturbances in time. Furthermore, the distribution of global modes is synchronized in the streamwise direction. This class of open flows is particularly well suited to a nonlinear dynamical systems approach of the kind that has been implemented in closed systems. The onset of deterministic chaos, if it exists, is likely to be well defined in these systems: One expects a well-ordered sequence of bifurcations leading from a limit cycle (the global mode) to a low-dimensional strange attractor. The sensitivity of convectively unstable flows to external noise, on the other hand, makes it much more difficult to discriminate between low dimensional chaos arising from the flow dynamics and spatially amplified random noise. Finally, there exists a

third class of marginally globally stable flows where the local velocity profiles are, strictly speaking, locally convectively unstable in the entire field but absolute instability is incipient at some streamwise station. In such situations, global modes are often weakly damped in time, and they can be preferentially destabilized by applying external forcing in the vicinity of the global-mode frequency (More details on this final case provided in section 3.1.3). This chapter is organized as follows. In section 3.1.1, 3.1.2, 3.1.3, we discuss the Temporal Instability, Absolute / Convective Instability and the concept of Evanescent modes, respectively. In order to distinguish between each of these instabilities, a basic understanding of the branch/pinch point as well as the Cusp-Map diagram is developed in section 3.1.4 and section 3.1.5, respectively. The Briggs' Contour Integral Method, utilized to classify the flow-material parameters leading to the above mentioned stability-instability regimes, is explained in section 3.1.6, and this method is further elaborated through an example in section 3.1.7.

3.1.1 Temporal Instability

The classical linear stability theory of parallel shear flows is concerned with the development in space and time of infinitesimal perturbations around a given basic flow $U(y; Re)$ In the sequel, x, y, and t denote the streamwise direction, cross-stream direction, and time, respectively, and $U(y; Re)$ is the sole component of the basic flow in the x-direction. The basic state is parallel, i.e. it is assumed to be independent of x. Fluctuations are typically decomposed into elementary instability waves $\phi(y; \alpha) exp[i(\alpha x - wt)]$ of complex wave number α and complex frequency w. The cross-stream distribution $\phi(y; \alpha)$ is then shown in most cases to satisfy an ordinary differential equation of the Orr-Sommerfeld type. Enforcement of appropriate boundary conditions at, say, Y_l and Y_2 then leads to an eigenvalue problem whereby eigenfunctions $\phi(y; \alpha)$ exist only if α and w are constrained to satisfy a dispersion relation of the form

$$D[\alpha, w, \boldsymbol{M}] = 0. \tag{3.1}$$

where $\boldsymbol{M}$ is the vector of material and fluid parameters. For simple basic flows, this relation can be calculated explicitly. For more realistic velocity profiles, it is obtained by numerical integration of the Orr-Sommerfeld equation. *Temporal modes* $w(\alpha, Re)$ refer to cases where the complex frequency w is determined as a function of real wave number α. Conversely, *spatial branches* $\alpha(w; Re)$ are obtained by solving for complex wave numbers α when w is given real. In this section we deliberately ignore variations in the cross-stream direction y and only consider the spatio temporal evolution of instability waves in the (x, t)-plane. This projection greatly simplifies the presentation of the fundamental concepts without losing any of the essential characteristics of the instability. Thus, one may associate a differential or integro-differential operator $D[-i(\partial/\partial x), i(\partial/\partial t); \boldsymbol{M}]$ in physical space (x, t) to the dispersion relation (3.1) in spectral space $(\boldsymbol{M}, w)$, such that fluctuations $u(x, t)$ satisfy

$$D\left[-i\frac{\partial}{\partial x}, i\frac{\partial}{\partial t}; \boldsymbol{M}\right] u(x, t) = 0 \tag{3.2}$$

To solve the corresponding receptivity problem for the above equation, one introduces the Green's function, i.e. the impulse response $G(x, t)$ of the flow defined by

$$D\left[-i\frac{\partial}{\partial x}, i\frac{\partial}{\partial t}; R\right] G(x,t) = \delta(x)\delta(t) \tag{3.3}$$

with δ denoting the Dirac delta function. The basic flow is then said to be linearly stable if

$$\lim_{t\to\infty} G(x,t) = 0 \text{ along all rays } x/t = \text{ constant} \tag{3.4}$$

and it is linearly unstable if

$$\lim_{t\to\infty} G(x,t) = \infty \text{ along at least one ray } x/t = \text{ constant.} \tag{3.5}$$

3.1.2   Absolute and Convective Instability

Among linearly unstable flows, one must further distinguish between two types of impulse response: The basic flow is referred to as convectively unstable if

$$\lim_{t\to\infty} G(x,t) = 0 \text{ along the ray } x/t = 0 \tag{3.6}$$

and it is absolutely unstable if

$$\lim_{t\to\infty} G(x,t) = \infty \text{ along the ray } x/t = 0, \tag{3.7}$$

as shown in Fig 3.1. The above definitions can be illustrated on the linearized Ginzburg Landau model. The operator D then takes the form

$$D\left[-i\frac{\partial}{\partial x}, i\frac{\partial}{\partial t}; M\right] u(x,t) = \frac{\partial \psi}{\partial t} + V_g\frac{\partial \psi}{\partial x} \quad \frac{i}{2}V_{gg}\frac{\partial^2 \psi}{\partial x^2} + iV_{gr}(R\cdot R_e)\psi = 0 \tag{3.8}$$

where V_g is a real positive constant group velocity, and V_{gg} and V_{gr} are complex constants with $V_{gg.i} < 0$. When an appropriate cubic nonlinearity is added, this simple model is known to arise in many marginal-stability analyses of fluid-dynamical systems close to onset (Newell and Whitehead, 1969) and (Stewartson and Stuart, 1971). Typically, convectively unstable flows give rise to wave packets that move away from the source and ultimately leave the medium in its undisturbed state. Absolutely unstable flows, by contrast, are gradually contaminated everywhere by a point-source input. In order to distinguish between convective and absolute instabilities, it is further necessary to examine, according to definitions (3.6) and (3.7), the long-time behavior of the wave number α_0 observed along the ray $x/t = 0$ at a fixed spatial location. This complex α_0 has, by definition, a zero group velocity, i. e.,

$$\frac{\partial \omega}{\partial \alpha}(\alpha_0) = 0, \tag{3.9}$$

and the corresponding $\omega_0 = \omega(\alpha_0)$ is commonly called the absolute frequency. The absolute growth rate is then denoted by $\omega_{0,i} = \text{Imag}(\omega(\alpha_0))$. In other words, the absolute growth rate $\omega_{0,i}$ characterizes the temporal evolution of the wave number α_0 observed at a fixed station in the limit $t \to \infty$. By contrast, the maximum growth rate $\omega_{i,max}$ defined previously is observed following the peak of the wave packet. Just as the sign of $\omega_{i,max}$ determines the unstable/stable nature of the flow, the sign of
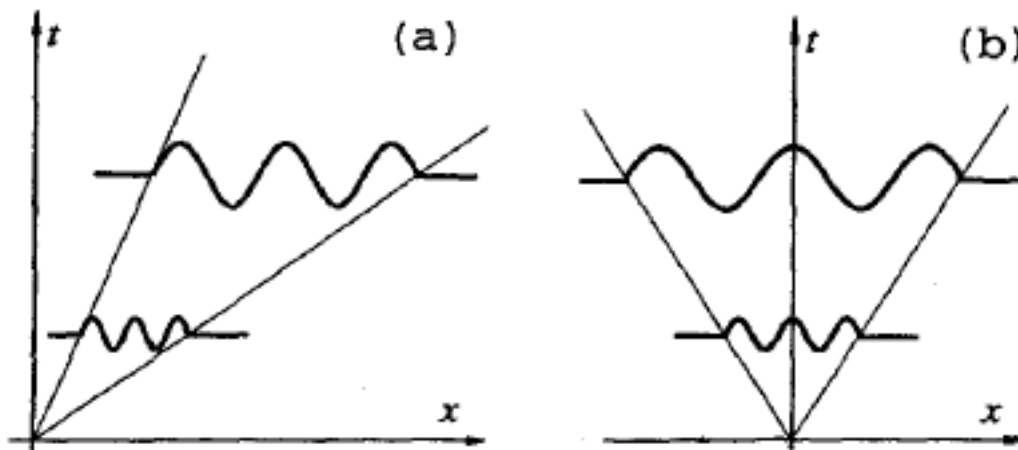
FIGURE 3.1: (a) Convective, (b) Absolute instability (Source (Schmid
and Henningson, 2001))

$\omega_{0,i}$ determines its absolute/convective nature. One therefore is led to the following
criterion:

$$\omega_{0,i} > 0 \qquad \text{absolutely unstable flow,}$$
$$\omega_{0,i} < 0 \qquad \text{convectively unstable flow.} \qquad (3.10)$$

3.1.3 Concept of Evanescent Modes

A flow field governed by the Navier-Stokes equations can sustain in general three dif-
ferent types of modal wave fields namely acoustic, vorticity and entropy waves (see
for example, Pierce (Pierce, 1981)). In the linear approximation these modal fields
are uncoupled except at boundaries or possibly at direct resonances. One speaks of a
direct resonance if in a physical system, which allows more than one wave mode, two
(or more) of these modes coalesce. In the present investigation we shall concentrate
on the coalescence of modes of the same wave type and in particular on the coa-
lescence of vorticity modes. If no or only very weak instabilities are present direct
resonance can be a rather powerful selection mechanism leading to algebraic growth
for small times or short distances and the corresponding potentially large amplitudes
may initiate the nonlinear solution long before the exponentially growing mode does.

The concept of direct resonance appears to have important consequences in the
generation of waves by wind, (e. g., Akylas (Akylas, 1982)), and in the stability
of locally parallel shear flows, (Benney and Gustavsson (Benny and Gustavsson,
1981), see also Gustavsson and Hultgren (Gustavsson and Hultgren, 1980), Gustavs-
son (Gustavsson, 1981) and Hultgren and Gustavsson (Hultgren and Gustavsson,
1981) as well as the articles by Akylas and Benney (Akylas and Benney, 1980; Aky-
las and Benney, 1982) on a weakly nonlinear theory of waves at direct resonance). In
the above parencited papers concerning the stability of parallel shear flows the reso-
nant forcing of the vertical vorticity (and hence the horizontal velocity components)
by the vertical velocity has been explored with the goal of elucidating the laminar-
turbulent transition process. This corresponds to a direct resonance between an Orr-
Sommerfeld and a vertical vorticity or so called 'Squire' mode. Research concerning
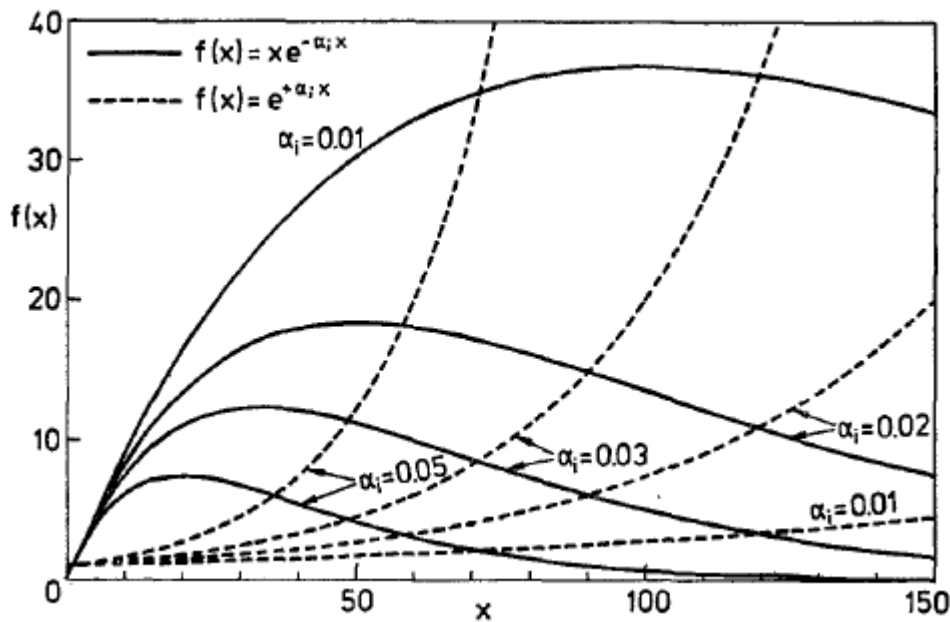
FIGURE 3.2:   Effect of direct resonance on amplitude evolution
(Source (Koch, 1986))

this so called Benney-Gustavsson resonance mechanism is very promising and has
been pursued extensively. However, the main interest of this thesis lies in finding out
whether the flow can support a direct resonance between two Orr-Sommerfeld modes
alone and whether such a resonance mechanism can be of physical importance.The
character of a direct resonance depends on the type of singularity in the dispersion
relation at the point of mode coalescence. It is usually determined by studying the
response to a point source in time and space. In a linear neutrally stable system the
'cut-off' phenomenon separating propagating from evanescent acoustic waves in a
hard-walled duct belongs to this category (Aranha, Yue, and Mei, 1982).

   If the two coalescing modes originate from waves propagating in the same direc-
tion as in the case of a convectively unstable flow the corresponding singularity is
of the double pole type. Such a disturbance will decay ultimately according to lin-
ear theory. However, the short-term algebraic growth associated with such a double
pole may be decisive and carry the system into the nonlinear state. Whether this is
physically possible is determined by the damping rate associated with the modal co-
alescence. If the damping rate is large such resonances are of importance in certain
linear optimization problems (an example is the (Cremer, 1953) for ducts with acous-
tically absorbing walls). If the coalescing modes are nearly neutral the corresponding
damping rates are very small and the algebraic growth may dominate the exponen-
tial decay locally. This is the case addressed by (Benny and Gustavsson, 1981) as
well as in the present investigation of plane Poiseuille and boundary-layer type mean
flows which are typical examples of convectively unstable flows. To understand the
concept of evanescent mode, Let us take an example of a function $f(x) = \exp(-\alpha_i x)$
This is demonstrated in Fig. 3.2 by plotting the functions $x \exp(\alpha_i x)$ and $\exp(-\alpha_i x)$
for various $\alpha_i = \text{Im}(\alpha)$. For large α_i high amplitudes $f(x)$ are quickly reached by
the exponentially growing mode $\exp(\alpha_i x)$. However if α_i is very small this growth
is very slow and therefore a direct resonance generating $x \exp(-\alpha_i x)$ can produce

large amplitudes much faster. Although these modes ultimately decay according to linear theory the locally high amplitudes may initiate the nonlinear state. In order to determine if this is possible for a given flow we have to find out, (i) under which conditions direct resonances exist, and (ii) how large the corresponding damping rates are.

3.1.4 Branch Points and Pinch Points

The simultaneous occurrence of a pinch point in the α-plane and a branch point in the w-plane can be explained as follows. A pinch point α^{pinch} in the complex α-plane is a special kind of saddle point satisfying the relation

$$D\left(\alpha^{pinch}, \omega^{cusp}\right) = 0 \quad \frac{\partial D}{\partial \alpha}\left(\alpha^{pinch}, \omega^{cusp}\right) = 0 \quad \frac{\partial^2 D}{\partial \alpha^2}\left(\alpha^{pinch}, \omega^{cusp}\right) \neq 0 \tag{3.11}$$

A Taylor series expansion of the dispersion relation in the neighborhood of the singularity $(\alpha^{pinch}, \omega^{cusp})$ then leads to

$$0 = \left.\frac{\partial D}{\partial \omega}\right|_0 (\omega - \omega^{cusp}) + \frac{1}{2}\left.\frac{\partial^2 D}{\partial \alpha^2}\right|_0 \left(\alpha - \alpha^{pinch}\right)^2 + \mathcal{O}\left((\omega - \omega^{cusp})^2, \left(\alpha - \alpha^{pinch}\right)^3\right) \tag{3.12}$$

This expression gives a relation between the neighborhood of ω^{cusp} in the w-plane and the neighborhood of α^{pinch} in the α-plane. The quadratic nature of the local map between the α and w-planes results in a square root singularity for the local map between the w and α-planes.

If the contour deformation procedure results in a pinch point in the α-plane, we are dealing with an absolute instability if the associated branch point in the w-plane lies above the imaginary w-axis. From the definition of absolute instability it is clear that such an instability depends on the existence of an unstable wave with zero group velocity. At an unstable pinch/branch point we have the group velocity, V_g, such that,

$$V_g = \frac{\partial \omega}{\partial \alpha} = \frac{\partial D}{\partial \alpha}\bigg/\frac{\partial D}{\partial \omega} = 0. \tag{3.13}$$

3.1.5 The Cusp Map

We have seen that the asymptotic space-time evolution of a linear instability is governed by the location of pinch points in the complex α-plane that are found by an analytic continuation of the Laplace inversion contour into the lower-half of w-plane. This technique requires solving the dispersion relation for the spatial wave number α as a function of the frequency w. This seems unfortunate, because the computation of w as a function of α is, in most cases, much easier. It is the goal of this section to introduce a method for detecting absolute instabilities that solely relies on a mapping from the α-plane to the w-plane. This technique is due to (Kupfer, Bers, and Ram, 1987) , who refer to it as the 'cusp map' in the complex-frequency plane.

We will start by examining the mapping from the α-plane to the w-plane. In general, dispersion relations are higher order polynomials (or transcendental) in the wave number α and thus the mapping of the F-contour into the w-plane is multivalued. Let us denote the image of F in the w-plane by $w(F)$. The reverse mapping of $w(F)$ back
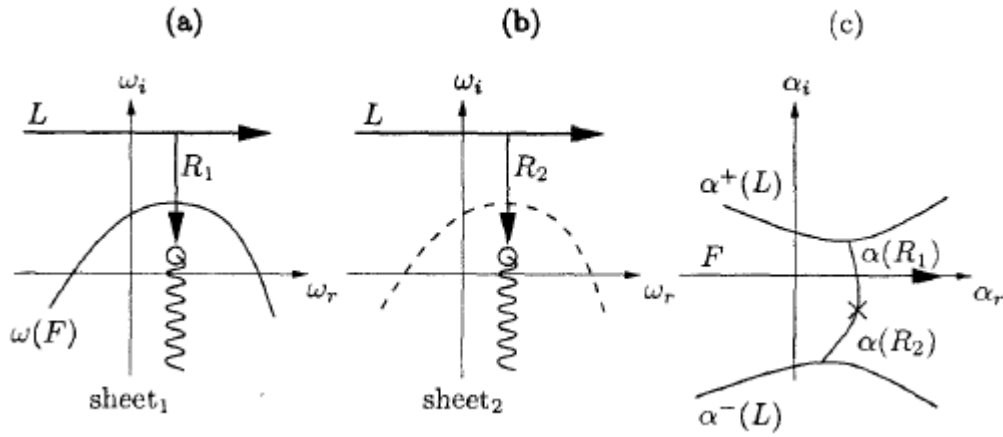
FIGURE 3.3:　 Sketch illustrating the cusp map method
(Source (Kupfer, Bers, and Ram, 1987)).

into the α-plane will result in n branches $\alpha_k(w(F))$ with n as the highest order of α
in the dispersion relation. Nevertheless, the original contour F is recovered by one of
the n branches To make the mapping of the F-contour into the w-plane single-valued
we introduce n Riemann shects in the complex w-plane and associate the n contours
in the multi-sheeted w-plane with the n branches $\alpha_k(w(F))$ in the α-plane. The map
between the w and α-plane is governed by the dispersion relation $D(\alpha, w) = 0$ For a
pinch point in the complex α-plane we have the additional constraints

$$\frac{\partial D(\alpha, \omega)}{\partial \alpha} = 0 \quad \frac{\partial^2 D(\alpha, \omega)}{\partial \alpha^2} \neq 0 \tag{3.14}$$

A point w_0 in the complex w-plane that satisfies these conditions for a corresponding
α_0 has only $n1$ image points in the complex α_0 plane. In other words, two sheets in
the w-plane connect at this specific point w_0 We will now concentrate on these two
sheets. Let us introduce a vertical ray that, connects the contour L in each of the two
sheets to the point w_0 (refer Fig. 3.3). We will call these rays R_1 and R_2. They will
help us determine whether the point w_0 in the w-plane corresponds to a pinch point
α_0 in the α-plane: If and only if the images of the rays R_1 and R_2 in the complex
α-plane, i.e., $\alpha(R_1)$ and $\alpha(R_2)$ in Fig. 3.3, originate on two different sides of F, the
branch point at $w = w_0$ corresponds to a pinch point in the α-plane. If the images
$\alpha(R_1)$ and $\alpha(R_2)$ originate on different sides of F, but connect at one single point
α_0 which is not on F, we must conclude that at least one of these images crosses F.
If more than one crossing occurs, the total number of crossings by both images must
be odd.

　This criterion forms the basis of the cusp map procedure: By counting the num-
ber of times that each vertical ray, R_1 and R_2, intersects the contour $w_k(F)$, we can
determine whether the branch point w_0 corresponds to a pinch point in the α-plane.
The procedure just described, which is completely general, may be used, together
with the following procedure, to determine the stability characteristics of any dis-
persion relation. The procedure requires mapping a section of the α-plane into a
specified region located beneath $w(F)$. A set of vertical rays along the range of un-
stable wave numbers is mapped into the w-plane. These rays, originally parallel in
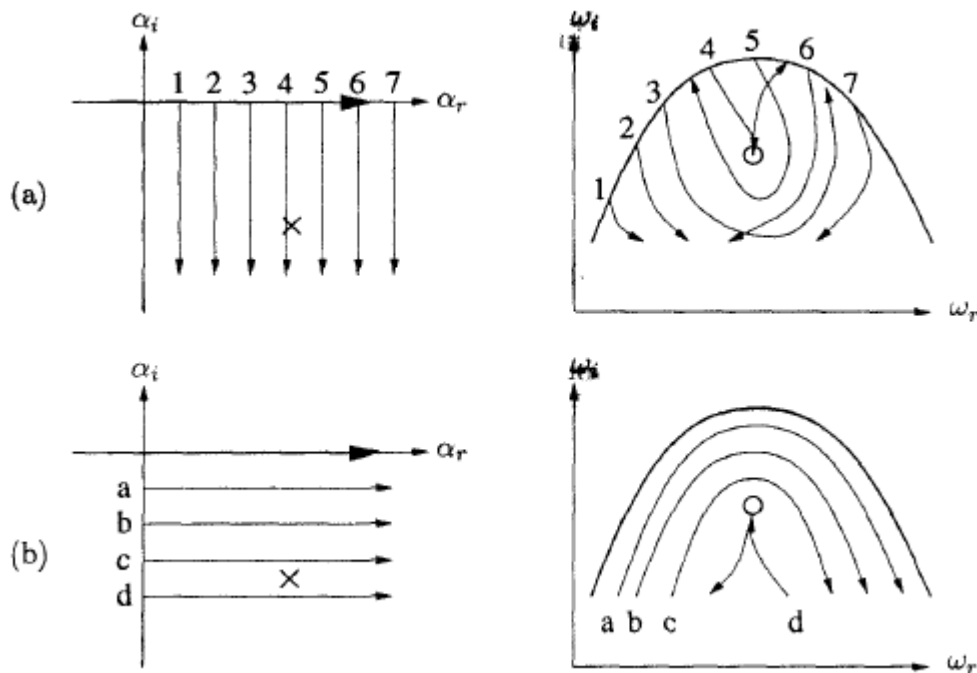
FIGURE 3.4: Outline of the numerical procedure for detecting branch points in the *w*-plane used in the cusp map method (Source (Kupfer, Bers, and Ram, 1987)).

the α-plane, may have images that intersect, thus indicating a branch point. The singularity is identified by the angle-doubling property of its local map. This is the case in Fig. 3.4, which shows the branch point nested at the edge of a cusp-like trajectory. If a branch cut is taken downward from the singularity, one obtains a mapping consistent with the multi-sheeted structure implied by the contour $w(F)$. In this case the branch point is covered only once by $w(F)$ and thus corresponds to a pinch point. In many problems it is simpler to replace the vertical rays shown in Fig. 3.4 with a set of horizontal contours that represent deformations of the Fourier integral path. In the *w*-plane, these contours will progress downward from $w(F)$ and form a cusp as they approach the singularity; see Fig. 3.4. Once again the branch point is located by the angle-doubling (-tripling, etc) property of its local map. This same procedure can be systematically generalized for dispersion relations with multiple unstable branches.

3.1.6 Briggs' Method

We will next derive general mathematical criteria based on the singularity structure of the dispersion relation in the complex w and α-planes to classify instabilities as convective or absolute. A crucial step in detecting absolute instabilities is locating pinch points in the complex a plane. A systematic way of accomplishing this was suggested by Briggs' (Briggs, 1964) , where we repeatedly solve for the spatial branches of the dispersion relation for frequencies w given along specified paths in the complex *w*-plane. For simplicity, we choose straight lines parallel to the imaginary *w*-axis. Mapping points along these w paths into the α-plane traces out spatial branches of the dispersion relation associated with the given temporal branches in
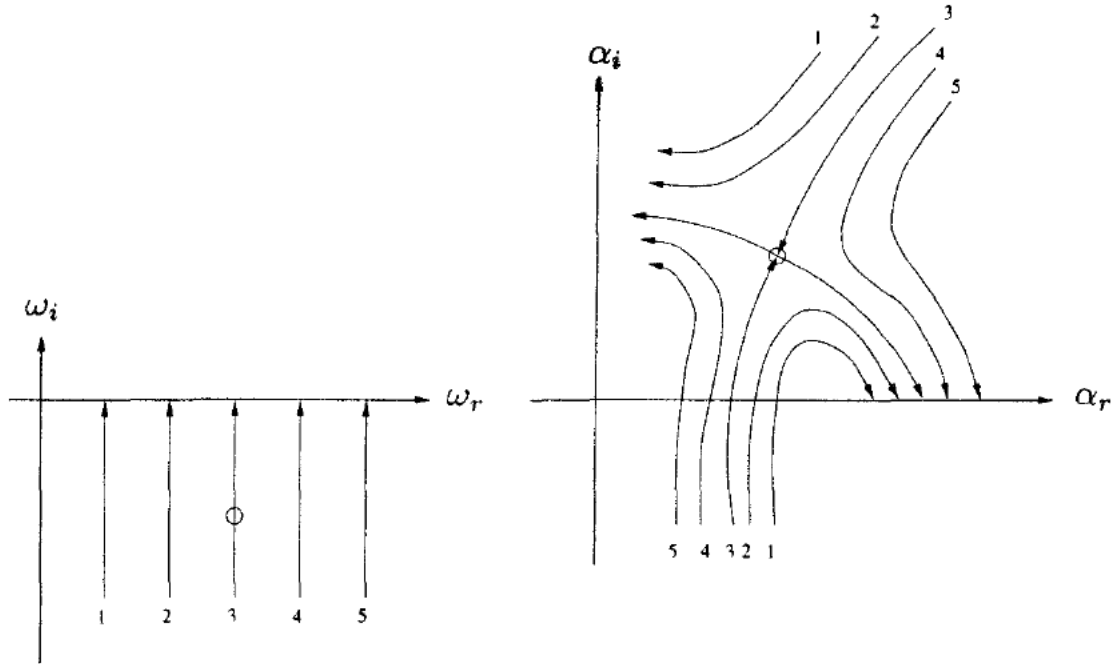
FIGURE 3.5: Illustration of the numerical procedure for detecting saddle points in the α-plane used in the Briggs' method (Source (Schmid and Henningson, 2001)).

the *w*-plane. By varying the real part of the *w* lines, we gradually visualize the map of the *w*-plane into the α-plane under the dispersion relation D(α,*w*) = 0. It should then be fairly straightforward to locate saddle points in the α-plane. An important restriction to keep in mind is that the saddle point has to consist of spatial branches that originate in different half-spaces. A saddle point clearly forms in the α-plane as the *w* lines are varied accordingly. Moreover, the two spatial branches forming the saddle point originate in two different half-spaces. The corresponding branch point in the *w*-plane, marked by a circle along the third ray (refer Fig. 3.5), lies below the real *w*-axis and thus does not constitute an absolute instability, according to Briggs' criterion.

We will start with the solution to the stability problem in Fourier-Laplace space. If we Fourier- and Laplace-transform Eqn. (3.3) and formally revert back to physical space, we have

$$G(x,t) = \frac{1}{4\pi^2} \int_L \int_F \frac{\exp[i(\alpha x - \omega t)]}{D(\alpha, \omega, \boldsymbol{M})} d\alpha d\omega \qquad (3.15)$$

where *L* and *F* denote the inversion contour in the Laplace-*w*-plane and the Fourier α-plane, respectively. Although the Fourier-Laplace integral (3.15) could be determined for all *x* and *t*, the complexity of the dispersion relation suggests a time-asymptotic solution of the integral. Moreover, the definition of convective and absolute instability as a limit process for large time also warrants an asymptotic approach in evaluating the Fourier-Laplace integral (3.15) The time-asymptotic evaluation of the integral expression for the Green's function will involve the deformation of the integration contours in the complex α and *w*-planes. By deforming the integration path through a saddle point in the a plane, we can use the method of steepest descent to evaluate the time-asymptotic behavior. If this evaluation will result in a divergent

integral, the flow under investigation is considered absolutely unstable according to the definition. If the asymptotic limit results in a convergent integral (in fact, in a zero integral), the flow is convectively unstable. Special care has to be taken when applying the method of steepest descent. We will come back to this issue later. Careful evaluation of the time-asymptotic behavior of the Fourier-Laplace integral (3.15) is accomplished using a method introduced by Briggs. In Briggs' method (Briggs, 1964) the wave number integral is chosen first,

$$\tilde{G}(x,\omega) = \frac{1}{2\pi} \int_F \frac{\exp[i\alpha x]}{D(\alpha,\omega,\boldsymbol{M})} d\alpha \qquad (3.16)$$

which is followed by the *w*-inversion

$$G(x,t) = \frac{1}{2\pi} \int_L \tilde{G}(x,\omega) \exp[-i\omega t] d\omega \qquad (3.17)$$

The method of analytic continuation is used to deflect the original L-contour in an attempt to lower it below the real *w*-axis (refer Fig. 3.6). If this is achieved, the exponent in the w-inversion integral (3.17) forces the integrand to vanish as $t \to \infty$; if not, the time-asymptotic discrete response is governed by the highest discrete singularity in the *w*-plane. Lowering the *w*-contour could fail if a singularity above the real *w*-axis is encountered. Because of the interconnection through the dispersion relation this singularity in the *w*-plane will have an associated singularity in the α-plane. We start by choosing the real α-axis as the inversion contour for the spatial part. This integration path maps through the dispersion relation to a curve in the *w*-plane denoted by $w(F)$. The temporal inversion contour has to lie above this curve in order to satisfy causality: The integration path for t < 0, which involves closure in the upper half-plane, cannot encircle any singularities, or, in other words, the integrand of the *w* integrall (3.17) has to be analytic in the *w*-half-space: $0 > \text{maxIm}(w(F))$ The temporal contour L can also be mapped back into the α-plane, resulting in the branches labeled $\alpha^+(L)$ and $\alpha^-(L)$. The spatial branch above the real axis is associated with the dynamics downstream of the origin, while the branch below the real α-axis governs the perturbation behavior upstream of the source. By analytic continuation we will try to lower the *w* inversion contour below the real axis. As we deform the *w*-contour, its image in the α-plane will also deform At some point, the original α-contour will be squeezed between the two branches, which will necessitate the deformation of the original α-contour as well. This will in turn modify the *w*-contour. By constantly adjusting the inversion contours and their maps into the associated plane, we may arrive at a situation where the spatial inversion contour is pinched between the two spatial branches, therefore prohibiting any further deformation without crossing singularities. If this occurs, the temporal inversion contour cannot be lowered any further due to formation of a branch point in the *w*-plane.

Convectively unstable modes are produced by α-roots which end up in a different half of the α-plane from the one in which they originate, when the L contour is deformed onto the real α-axis. The crossing of the real α-axis distinguishes them from evanescent modes. A fuller account of the theory is given by (Bers, 1983). An absolute instability eigenmode is formed from the merging of two eigenmodes. As such its occurrence may be viewed intuitively as a form of resonance between the modes; a
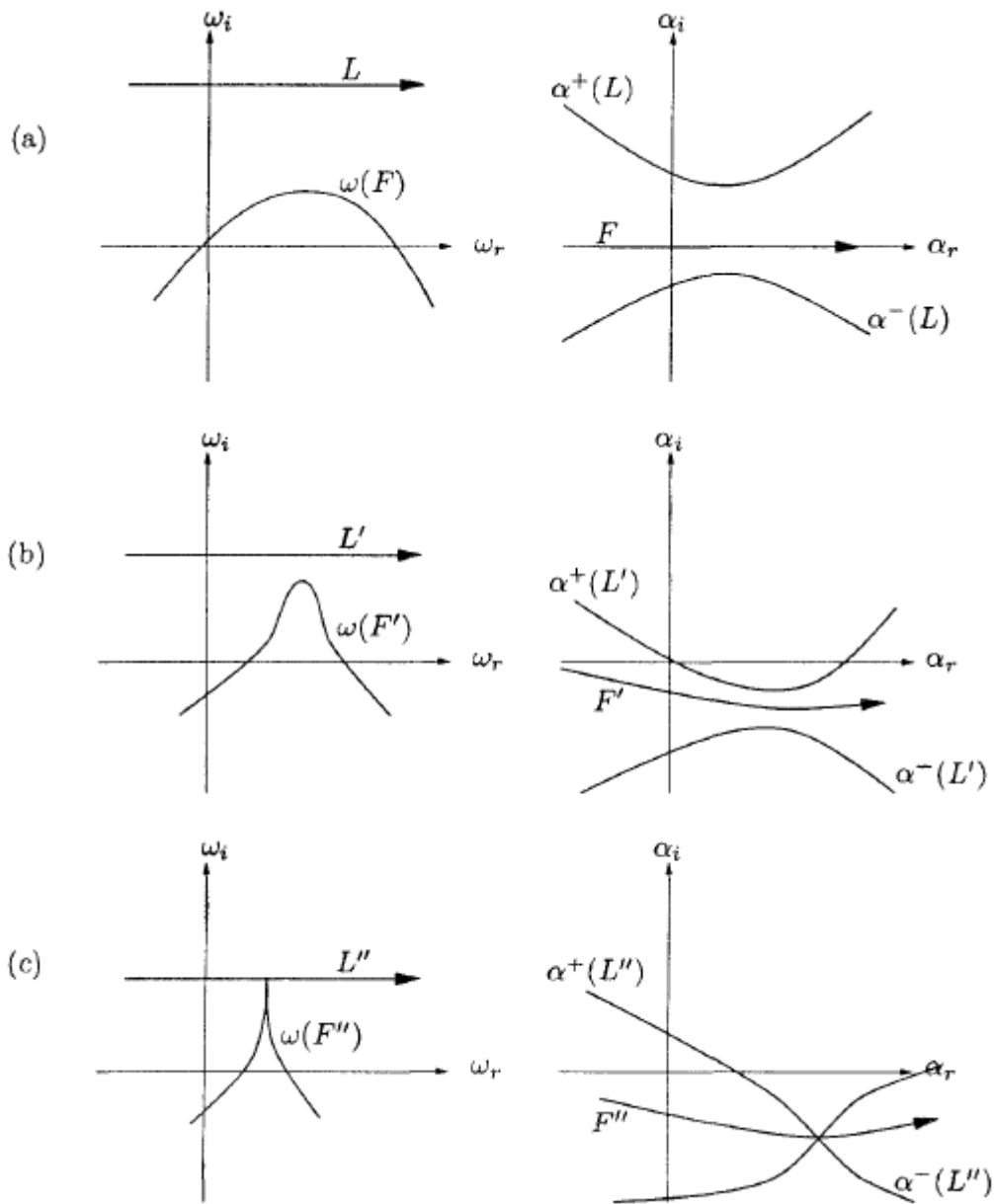
FIGURE 3.6: Sketch of contour deformation procedure for Briggs'
method.   Left: complex w-plane, right: complex α-plane
(Source (Schmid and Henningson, 2001)).
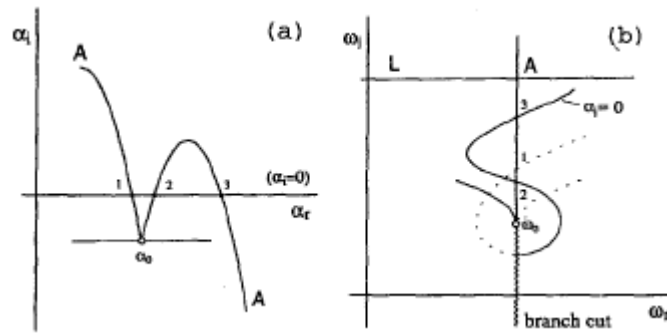
FIGURE 3.7: An example in schematic of an absolute instability created by the intersection of two α-roots with three crossing of the α_r-axis ($\alpha_i = 0$). The vertical ray from w_0 cuts the $\alpha_i = 0$ contour in the three places in the double-sheeted w-plane (Source (Yeo, Khoo, and Zhao, 1996)).

resonance which leads to growth, since the merged eigenmode has $w_i > 0$. Physically, the modal interaction associated with the merging takes place over the source of the perturbation. This is because the participating modes are from the upstream ($x_1 < 0$) and downstream ($x_1 > 0$) sides of the source. Thus the instability is localized with respect to the location of the source, and envelopes an ever increasing neighborhood of the perturbation source with time. A shear flow with a sizable pocket of absolute instability may display the dynamic characteristics of a closed-flow (compact) system. These unstable flows behave like an oscillator. A convectively unstable mode, on the other hand, has been shown to be associated with a sinusoidal wave which grows in amplitude as it travels away from the source, from which it also derives its frequency. A convectively unstable mode is essentially a driven mode. It decays to zero with time when the driving source is turned off; whereas an absolutely unstable mode is more akin to a self-sustaining temporal mode, and has been termed as such by Bers (Bers, 1983). When $(w_o)_i > 0$, a possible absolute instability is indicated. It is still necessary, however, to verify that the intersection arises from roots originating from opposite halves of the α-plane. For such an intersection to be possible, at least one of the α-roots must cross the α_r-axis of the α-plane at least once. An even number of crossing brings an α-root back into its original half of the α-plane, while an odd number brings it into the opposite half. The sum total of crossings must be an odd number for a genuine pinch point. The fulfillment of this requirement can be checked by drawing a straight ray from the suspected cusp point vertically upward (w_r = constant) and observing the number of times this ray intersects the image of the α_r-axis ($\alpha_i = 0$) in the w-plane (a double or multisheeted Reimann surface). This is because every crossing of the α_r-axis in the α-plane by the α-roots (as the w_i is varied with the lowering of the L contour) is reflected by a corresponding crossing of the image of the α_r-axis ($\alpha_i = 0$) in the w-plane by the vertical ray (which represents variation in w_i) in one of the Riemann sheets of the co-plane. Figure 3.7 presents a schematic example of the application of this criterion to a situation in which the intersecting pair of α-roots crosses the α_r-axis a total of three times. In this case the upward vertical ray emanating from the cusp point cuts the image of the α_r-axis ($\alpha_i = 0$) three times on the two Riemann sheets. When the Riemann sheets of the branch point w^{cusp} correspond to spatial branches located in the same α-plane for

high enough L, no pinching of F can occur as L is lowered. The corresponding branch point in the w-plane is not related to the absolute growth rate. Thus, care must be exercised to locate branch-point singularities pertaining to spatial branches originating from distinct halves of the α-plane. The vertical-ray criterion may also be used to distinguish genuine convective instabilities from evanescent modes.

We summarize the Briggs' method as follows: The necessary (but not sufficient) condition for the presence of absolute instability is the vanishing characteristic of the group velocity, v_g, at the saddle point in the α-plane or the branch point in the ω-plane ($v_g = \frac{\partial \omega}{\partial \alpha} = (\frac{\partial D}{\partial \alpha})/(\frac{\partial D}{\partial \omega}) = 0$ such that $\omega = D(\alpha)$). But the group velocity is zero at every saddle point, in particular where the two α-branches meet, independent of whether the branches originate from the same half of the α-plane (i. e., when evanescent modes are detected) or not. To overcome this inadequacy, Briggs (Briggs, 1964) devised the idea of analytic continuation in which the Laplace contour L, in equation (3.15), is deformed towards the ω_r axis of the complex ω-plane, with the simultaneous adjustment of the Fourier contour F in the α-plane to maintain the separation of the α-branches; those which originate from the top half (the upstream modes with $\alpha_i > 0$) from those which originate from the bottom half of the α-plane (or the downstream modes). The deformation of the F contour (while preserving causality) is inhibited, however, when the paths of the two α-branches originating from the opposite halves of the α-plane intersect each other, leading to the appearance of saddle points which are the *pinch point*, α^{pinch}. The concurrent branch point appearance in the ω-plane is the *cusp point*, ω^{cusp} (i. e., $D(\alpha^{\mathrm{pinch}}, \omega^{cusp}) = \frac{\partial D(\alpha^{\mathrm{pinch}}, \omega^{cusp})}{\partial \alpha} = 0$ but $\frac{\partial^2 D(\alpha^{\mathrm{pinch}}, \omega^{cusp})}{\partial \alpha^2} \neq 0$). Kupfer (Kupfer, Bers, and Ram, 1987) employed a local mapping procedure to conceptualize the stability characteristics of this branch point. Near a 'reasonably close' neighborhood of the pinch point, a local Taylor expansion yields a dispersion relation which has a second-order algebraic form in the ω-plane (and which is a first order saddle point in the α-plane), i. e., $(\omega - \omega^{cusp}) \sim (\alpha - \alpha^{\mathrm{pinch}})^2$. This period-doubling characteristics of the map causes the α_i-contours to 'rotate' around ω^{cusp}, forming a cusp. In the ω-plane, we draw a ray parallel to the ω_i-axis from the cusp point such that it intersects the image of the F-contour (or $\alpha_i = 0$ curve) and count the number of intersections (consequently, count the number of times both α-branches cross the α_r-axis before forming a pinch point in the α-plane, as shown in Figure 3.7). If the ray drawn from the cusp point intersects the image of the F contour in the ω-plane (or if either one or both the α-branches cross the α_r-axis) even number of times, then the flow dynamics correspond to an evanescent mode. Otherwise, in the case of odd intersections the observed cusp point is genuine, leading to either absolutely unstable system (in the upper half of the ω-plane) or convectively unstable system (in the lower half of the ω-plane); provided the system is temporally unstable.

3.1.7 An Example

To further demonstrate this important method, we will introduce a sample dispersion relation (taken from (Kupfer, Bers, and Ram, 1987)) and apply Briggs' method. The dispersion relation is a mathematical one; it is used here for demonstration purposes only. Its simplicity allows explicit solutions for the pinch point and branch point
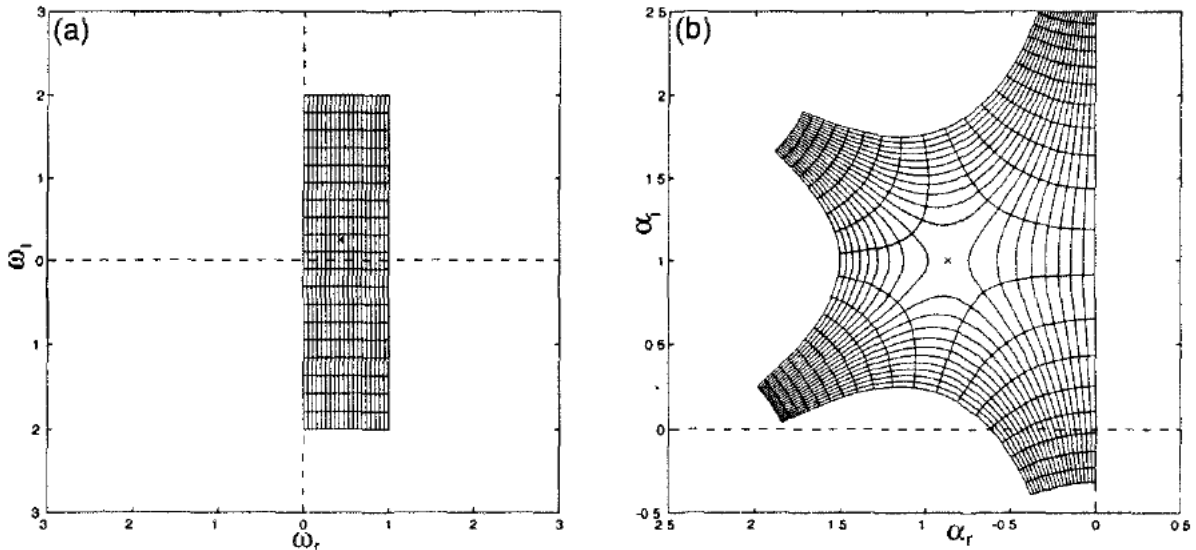
FIGURE 3.8: Map of the complex w-plane into the complex α-plane under the dispersion relation (3.18)(Source (Schmid and Henningson, 2001)).

locations. We consider

$$D(\omega, \alpha) = \omega - \left[\frac{1}{3}(\alpha - i)^3 + i - \alpha V\right] \tag{3.18}$$

where we have also introduced a parameter V. The pinch points and branch points can be found by solving $dw/d\alpha = 0$, which yields

$$\alpha_{1,2} = i \pm \sqrt{V} \tag{3.19}$$

for the pinch points and

$$\omega_{1,2} = (1 - V)i \mp \frac{2}{3}V\sqrt{V} \tag{3.20}$$

for the associated branch points in the w-plane. We set V = 0.75 and proceed with Briggs' method as outlined earlier We will map lines of constant w into the complex α-plane by solving the cubic dispersion relation (3.18).

Clearly, a saddle point forms in the complex α-plane that is marked by a symbol and corresponds to the solution of equation (3.19) for V = 0.75 (refer Fig. 3.8). Its branches originate in different half-spaces of the α-plane. The corresponding branch point in the w-plane is also marked. We see that the branch point is clearly above the real w-axis, proving the occurrence of an absolute instability. Admittedly, this example is fairly simplistic. It nevertheless demonstrates the usefulness of Briggs' method to detect absolute instabilities. More complicated dispersion relations can be contrived that challenge the readers' knowledge of analytic function theory.

The method just outlined for the computation of absolute and convective stability characteristics is closely related to the method of steepest descent. The method of steepest descent does not distinguish between branches originating in the same or different half-spaces. Additional analysis of the global topology of the phase function is necessary to focus on the correct type of saddle points in the α-plane. In fact, the integral representation of the Green's function solution suggests looking for saddle

points of the phase function and evaluating the integral asymptotically according to standard techniques. It is important to also consider the global topology of the phase function; not all points with $dw/d\alpha = 0$ are associated with absolute instabilities Failure to consider the global topology of the phase function may result in flawed calculations and incorrect conclusions about the absolute or convective nature of the instability (Huerre and Monkewitz, 1990). For a more detailed treatment, including numerical examples, the reader is referred to (Lingwood, 1997).

Chapter 4

Spatiotemporal linear stability of viscoelastic free shear flows: dilute regime

4.1   Introduction

In this chapter we report the temporal and spatio-temporal stability analyses of anti-symmetric, free shear, viscoelastic flows obeying the Oldroyd-B constitutive equation in the limit of low to moderate Reynolds number (*Re*) and Weissenberg number (*We*). Classical approaches to the viscoelastic instability studies involve identifying an equilibrium state, whose stability is studied through eigenvalue analysis by linearizing the governing equations. The eigenvalue analysis seek the least stable eigenmode of the linearized mass and momentum conservation equations suitably transformed to the Orr-Sommerfeld Equation (OSE) (Drazin and Reid, 2004; Sengupta, 2016) via parallel flow approximation. One of the features of traditional eigenvalue analysis is that the disturbance field is assumed to grow either in space or in time. Huerre and Monkewitz (Huerre and Monkewitz, 1990) have attempted to apply the combined spatio temporal theory to a restricted class of Newtonian mixing layers with the goal of determining a general criterion whereby a class of flows can be analyzed by either the spatial or temporal theory by inspecting the dispersion relation in the complex wave number-frequency plane. Some other applications as well as laboratory and numerical experiments on the stability studies of shear flows of Newtonian and non-Newtonian liquids are listed in (Batchelor, Moffatt, and Worster, 2002; Schmid and Henningson, 2001; Kalliadasis et al., 2012). However, the models and experiments listed in these references fail to present a comprehensive, spatio temporal analyses of plane, free shear flows in the form of an instability-phase diagram. Therefore a motivation of this chapter is to illustrate this phase diagram in the viscoelastic parameter space. The characterization of fluid flows as being absolutely or convectively unstable and the method of spatio temporal analysis by progressive moving of the isocontours in the complex frequency and wavenumber plane was first proposed by Briggs (Briggs, 1964) and later by Bers (Bers, 1983) in the context of plasma physics. Early numerical work focused on actively controlling the temporal instability in the inertial limit of free shear layer, polymer flow simulations via addition of polymers (Azaiez and Homsy, 1994a), the use of time dependent motion of the boundaries, the modification of the properties of the surfaces and including grooves and ribs (Stone et al., 2004). Rallison *et al.* detailed separate studies of

temporal as well as spatial instability in channel flows of dilute polymer solution, including stratified flows (Wilson and Rallison, 1999) and multilayer Couette and Poiseuille flows (Miller and Rallison, 2007), obeying either the Oldroyd-B, Upper Convected Maxwell or the Finitely Extensible Nonlinear Elastic (FENE) fluid constitutive equations. The literature on theoretical studies of the spatio temporal linear analysis of viscoelastic flows are more recent (Govindarajan and Sahu, 2013). In this chapter, we aim to address the following intriguing questions through combined linear spatio temporal stability analysis: What is the critical flow / polymer relaxation conditions for the onset of instability ? and more crucially What is the linear spatio temporal, time asymptotic response of the flow at the critical value of the material parameters ? In the next section, we delineate the model of the free shear layer flow coupled with the Oldroyd-B constitutive relation for the extra elastic stress tensor (§4.2.1) and the details of the linear stability analysis via the fourth order OSE (§4.2.2). A thorough description of the Briggs contour integral method to determine the existence of absolute instability, convective instability and evanescent modes in spatio temporal analysis in included in this section. In §4.3, we introduce the Compound Matrix Method to numerically integrate the resultant system of stiff differential equations for the auxiliary variables emerging from the Orr-Sommerfeld equation. Section 4 highlights the simulation results of the temporal (§4.4.1) and the spatio temporal (§4.4.2) stability analyses of anti-symmetric, free shear flows of polymeric liquids. This chapter concludes with a brief discussion of the implication of these results and the focus of our future direction (§4.5).

4.2 Mathematical model and linear stability analysis

Unlike Newtonian solvents, the stability predictions of polymeric liquids depend upon the details of the equations relating stress to the shear rate. The Oldroyd-B constitutive equations has its range of applicability limited to dilute solutions and moderate shear rates (Bird et al., 1987). It predicts no shear thinning, a constant first normal stress coefficient and a zero second normal stress coefficient. The numerical solution obtained by linearizing the Navier Stokes along with the extra stress constitutive equation (or the OSE stability equation) is reliable in describing the characteristics of the initial stages of the mixing layer transition (Bird, Armstrong, and Hassager, 1987). The linear stability results can be utilized as the initial-boundary conditions for DNS (Sengupta, 2016) or the large eddy simulation of polymeric liquids (Steinberg, 2018) in order to further study the flow evolving process downstream.

4.2.1 Mathematical model

For the mixing layer flow configuration it is customary to assume $\mathscr{U}_1$ (respectively $\mathscr{U}_2$) as the free-stream velocity of the upper (lower) flow. We denote $\mathscr{U}_0 = \frac{1}{2}(\mathscr{U}_1 - \mathscr{U}_2)$ as the free-stream velocity in a reference frame moving with the average velocity of the flow (i. e., $\frac{1}{2}(\mathscr{U}_1 + \mathscr{U}_2)$) and δ, the momentum thickness of the mixing layer.

The continuity and the momentum equations for an incompressible flow are,

$$\nabla \cdot \mathbf{v} = 0, \qquad \rho \frac{D\mathbf{v}}{Dt} = -\nabla p + \mathbf{v} \cdot \tau, \tag{4.1}$$

where $\mathbf{v}$ is the velocity vector, ρ the density, p the isotropic pressure and τ the extra stress tensor. Equations (4.1) are closed through the evolution equation for the extra stress tensor τ, written as the sum of the viscous, Newtonian stress, τ^s ($= \eta_s \mathbf{D}$, $\mathbf{D}$ is the shear rate tensor) and the elastic stress, τ^p ($= \eta_p \mathbf{A}$), where η_s, η_p are the solvent viscosity and the polymeric contribution to the shear viscosity, respectively. We let $\eta (= \eta_s + \eta_p)$ and $v (= \eta_s/\eta)$ denote the total viscosity and the viscous contribution to the total viscosity of the fluid, respectively. The constitutive equation for the extra stress tensor, τ, obeying the Oldroyd-B model then becomes,

$$\tau = \eta[v\mathbf{D} + (1 - v)\mathbf{A}], \tag{4.2}$$

where the tensor $\mathbf{A}$ satisfies the Upper Convected Maxwell equation,

$$\frac{\partial A}{\partial t} + \mathbf{v} \cdot \nabla \mathbf{A} - \nabla \mathbf{v}^T \cdot \mathbf{A} - \mathbf{A} \cdot \nabla \mathbf{v} = \frac{\mathbf{D} - \mathbf{A}}{\lambda}, \tag{4.3}$$

λ is the polymer relaxation time. Although the two basic ingredients of polymer rheology, anisotropy and elasticity, are properly described by the Oldroyd-B model, this constitutive relation fails in many circumstances, e. g., it fails to predict the physical value of the viscosity in extensional flow when the relaxation time of the polymer times the extension rate exceeds 0.5 (or when the elongational flow is strong enough to drive the two sides of the polymer dumbbell infinitely far apart from one another) (Bird et al., 1987).

4.2.2   Linear Stability Analysis

Using $\mathcal{U}_0$ and δ as the reference velocity and length scale, respectively, we characterize the non-dimensional form of equations (4.1), by the dimensionless numbers, $Re = \rho\delta\mathcal{U}_0/\eta$ and $We = \lambda\mathcal{U}_0/\delta$. We assume that the mean flow is two-dimensional (with x and y being the streamwise and spanwise directions in space, respectively) and quasi-parallel with its variation entirely in the spanwise direction, i. e.,

$$U(y) = \tanh(y), \ \Omega(y) = \tanh^2(y) - 1, \ \Psi(y) = \log(\cosh(y)), \tag{4.4}$$

where $U(y), \Omega(y), \Psi(y)$ are the dimensionless streamwise mean velocity (with zero spanwise mean velocity), spanwise mean vorticity and the associated streamfunction, respectively. Further, assume that the mean flow supports a two-dimensional disturbance field. The streamfunction and the extra stress tensor are represented by the base state profile $(\Psi(y), \mathbf{T}(y))$ plus a small perturbation, Fourier transformed in x and t as follows,

$$\psi(x, y, t) = \Psi(y) + \phi(y)e^{i(\alpha x - \omega t)},$$
$$\tau(x, y, t) = \mathbf{T}(y) + \varphi(y)e^{i(\alpha x - \omega t)}, \tag{4.5}$$

where $\phi(y), \varphi(y)$ are the spanwise perturbations in the streamfunction and the extra stress tensor and α, ω are the complex wavenumber and angular frequency, respectively. Note that (4.4) is a solution of the momentum equations for incompressible flow (4.1) provided that there is a dimensionless body force

$$\mathbf{f}(y) = \left(\frac{1-\nu}{Re}\mathbf{T}''_{12} - \frac{\nu}{Re}\Omega'' \right) \mathbf{e}_x, \tag{4.6}$$

where $\mathbf{T}_{12}$ is the shear component of the base state polymer stress and $()^n$ denote the nth derivative of any variable function with respect to y. The shear component of the base state polymer stress (i. e., the solution of equation (4.3) under the mean flow conditions (4.4)) is $\mathscr{O}(1)$ uniformly in the entire flow domain. Consequently, we argue that the correction due to the body force, $\mathbf{f}(y)$, is uniformly $\mathscr{O}(1/Re)$ in space. Rewriting equation (4.1) in the streamfunction-vorticity formulation and utilizing equations (4.2), (4.3), (4.4), (5.7), we arrive at the equation governing the perturbation of the streamfunction, given by the familiar fourth order OSE (Azaiez and Homsy, 1994a),

$$i\{(\alpha U - \omega)(\phi'' - \alpha^2\phi) - \alpha U''\phi\} - \frac{\nu}{Re}\left((\frac{d}{dy})^2 - \alpha^2 \right)^2 \phi =$$
$$\frac{1-\nu}{\mathscr{F}Re}\sum_{n=0}^{4}c_n\phi^{(n)}, \tag{4.7}$$

where the coefficients c_i's are

$$c_0(y) = \alpha^4 + \mathscr{F}^{(4)} - \alpha^2\left(\frac{\mathscr{F}''}{\mathscr{F}}\right)(\mathscr{F}-1)$$
$$- 2\alpha^2\left(\frac{\mathscr{F}'}{\mathscr{F}}\right)^2(\mathscr{F}^2+1) - 4\left(\frac{\mathscr{F}'}{\mathscr{F}}\right)\mathscr{F}''' - 3\frac{(\mathscr{F}'')^2}{\mathscr{F}}$$
$$+ 4\frac{(\mathscr{F}')^4}{\mathscr{F}^2} - 6\mathscr{F}''\left(\frac{\mathscr{F}'}{\mathscr{F}}\right)^2(\mathscr{F}-1),$$
$$c_1(y) = -2\alpha^2\left(\frac{\mathscr{F}'}{\mathscr{F}}\right)(\mathscr{F}-1) + 4\left(\frac{\mathscr{F}''}{\mathscr{F}}\right)\left(\frac{\mathscr{F}'}{\mathscr{F}}\right)(\mathscr{F}-1)^2 \tag{4.7a}$$
$$- 4\left(\frac{\mathscr{F}'}{\mathscr{F}}\right)^2(D_y\mathscr{F})(\mathscr{F}-1) + 2\left(\frac{\mathscr{F}'''}{\mathscr{F}}\right)(\mathscr{F}-1),$$
$$c_2(y) = -2\alpha^2 + 3\left(\frac{\mathscr{F}''}{\mathscr{F}}\right)(\mathscr{F}-1) + 2\left(\frac{\mathscr{F}'}{\mathscr{F}}\right)^2(\mathscr{F}-1)^2,$$
$$c_3(y) = 2\left(\frac{\mathscr{F}'}{\mathscr{F}}\right)(\mathscr{F}-1),$$
$$c_4(y) = 1,$$

and $\mathscr{F} = 1 + iWe(\alpha U - \omega)$, solved together with the vanishing boundary conditions for the free shear flow disturbance ($\phi \to 0, \phi' \to 0$ as $y \to \pm\infty$). In this chapter, we have limited the domain of integration in the spanwise direction to the upper half of the flow and analyzed only the anti-symmetric disturbance for the purpose

of illustrating the solution methodology. The boundary conditions are revised as follows,

$$\phi = \phi'' = 0 \quad \text{at} \quad y = 0 \tag{4.8a}$$

$$\phi = \phi' = 0 \quad \text{at} \quad y \to \infty. \tag{4.8b}$$

In § 4.3, we delineate a numerical solution procedure for solving the eigenvalue equation (4.7) together with the boundary conditions (4.8a)(4.8b).

4.3 Solution to the eigenvalue problem

The eigenvalues (i. e., the values of (α, ω) satisfying equation (4.7)) are found by examining the consequence of the far stream boundary condition, given by equation (4.8b), on the solution structure of the OSE. In the limit $y \to \infty$, we have $U(y) = 1$ and $U''(y) = 0$, which reduces the OSE to the following constant coefficient differential equation (Drazin and Reid, 2004),

$$\phi^{(4)} - 2\alpha^2 \phi'' + \alpha^4 \phi = \frac{iRe\mathscr{F}_\infty}{1 - \nu + \nu\mathscr{F}_\infty}(\alpha - \omega)(\phi'' - \alpha^2 \phi), \tag{4.9}$$

where $\mathscr{F}_\infty = 1 + We(\alpha - \omega)$. The solution to equation (4.9) can be obtained in the form $\phi = e^{\lambda y}$, with the characteristic roots given by $\lambda_{1,2} = \mp\alpha$ and $\lambda_{3,4} = \mp q$, where $q = \left[\alpha^2 + \dfrac{iRe\mathscr{F}_\infty}{1 - \nu + \nu\mathscr{F}_\infty}(\alpha - \omega)\right]^{1/2}$. The fourth order OSE (4.7) will have four fundamental solutions, $\{\phi_i\}_{i=1}^4$, i. e., $\phi = \sum_{i=1}^4 a_i\phi_i$. To satisfy the boundary condition (4.8b), one must have $a_2 = a_4 = 0$ for real $(\alpha, q) > 0$ which warrants a general solution of the form

$$\phi = a_1\phi_1 + a_3\phi_3. \tag{4.10}$$

Equation (4.10) is a non-trivial, admissible solution of the OSE, satisfying the zero boundary conditions at the centerline (i. e., at $y = 0$, equation (4.8a)) if and only if the determinant of the associated matrix of the linear algebraic system vanishes at $y = 0$, i. e.,

$$\left(\phi_1\phi_3'' - \phi_1''\phi_3\right)|_{y=0} = 0, \tag{4.11}$$

which is the dispersion relation of the problem. In the asymptotic limit of $Re \to \infty$, the eigenmodes of the free shear layer instability problems are such that $|q| \gg |\alpha|$. This enormous contrast between the two sets of roots of the characteristic equation (4.9) is the source of stiffness causing the fundamental solutions of the OSE to vary by several orders of magnitude in the entire physical domain, and thus necessitate the use of Compound Matrix Method (CMM) (Ng and Reid, 1985). In CMM, one works with a set of auxiliary variables which are combinations of the fundamental solutions

ϕ_1 and ϕ_3, namely

$$
\begin{aligned}
y_1 &= \phi_1\phi_3' - \phi_3\phi_1', \\
y_2 &= \phi_1\phi_3'' - \phi_3\phi_1'', \\
y_3 &= \phi_1\phi_3''' - \phi_3\phi_1''', \\
y_4 &= \phi_1'\phi_3'' - \phi_1''\phi_3', \\
y_5 &= \phi_1'\phi_3''' - \phi_1'''\phi_3', \\
y_6 &= \phi_1''\phi_3''' - \phi_1'''\phi_3'',
\end{aligned}
\tag{4.12}
$$

satisfying the corresponding first order ODEs,

$$
\begin{aligned}
y_1' &= y_2, \\
y_2' &= y_3 + y_4, \\
y_3' &= y_5 - \frac{(1-v)(c_1 y_1 + c_2 y_2 + c_3 y_3) + \mathscr{F}(i\mathrm{Re}(\alpha U - \omega + 2\alpha^2 v)y_2}{(1-v+\mathscr{F}v)}, \\
y_4' &= y_5, \\
y_5' &= y_6 + \frac{(1-v)(c_0 y_1 - c_2 y_4 - c_3 y_5) + \mathscr{F}(i\mathrm{Re}(\alpha U - \omega) + 2\alpha^2 v)y_4}{(1-v+\mathscr{F}v)} \\
&\quad + \frac{\mathscr{F}(i\mathrm{Re}[(\alpha U - \omega)\alpha^2 + \alpha U''] + \alpha^4 v)y_1}{(1-v+\mathscr{F}v)}, \\
y_6' &= \frac{(1-v)(c_0 y_2 + c_1 y_4 - c_3 y_6) + \mathscr{F}(i\mathrm{Re}[(\alpha U - \omega)\alpha^2 + \alpha U''])y_2}{(1-v+\mathscr{F}v)} \\
&\quad + \frac{\alpha^4 v y_2}{(1-v+\mathscr{F}v)}
\end{aligned}
\tag{4.13}
$$

Since at $y \to \infty$: $\phi_1 \sim e^{-\alpha y}$ and $\phi_3 \sim e^{-qy}$, we can estimate the free stream values of the unknowns,

$$
\begin{aligned}
y_1 &\sim (-q + \alpha)e^{-(\alpha+q)y}, \\
y_2 &\sim (q^2 - \alpha^2)e^{-(\alpha+q)y}, \\
y_3 &\sim (-q^3 + \alpha^3)e^{-(\alpha+q)y}, \\
y_4 &\sim (-\alpha q^2 + \alpha^2 q)e^{-(\alpha+q)y}, \\
y_5 &\sim (\alpha q^3 - \alpha^3 q)e^{-(\alpha+q)y}, \\
y_6 &\sim (-\alpha^2 q^3 + \alpha^3 q^2)e^{-(\alpha+q)y}.
\end{aligned}
\tag{4.14}
$$

Since all the variables in equation (4.14) attenuate at the same rate, the stiffness of the problem is removed by rescaling the variables, say with respect to y_1, so that the

(rescaled) free-stream conditions for solving equations (4.13) are

$$
\begin{aligned}
y_1 &= 1.0, \\
y_2 &= -(\alpha + q), \\
y_3 &= \alpha^2 + q\alpha + q^2, \\
y_4 &= q\alpha, \\
y_5 &= -q\alpha(\alpha + q), \\
y_6 &= (q\alpha)^2
\end{aligned}
\tag{4.15}
$$

The solution for equations (4.13) is obtained by marching backward from the free stream to the centerline, with the initial conditions provided by equations (4.15). A suitable value of (α, ω), or the eigenvalue for a given combination of material parameters $\mathbf{M}$ is obtained by enforcing the dispersion relation (equation (4.11)) in auxiliary variables, i. e.,

$$
y_2 = 0 \quad \text{at} \quad y = 0.
\tag{4.16}
$$

Now the task is of finding out the corresponding eigenfunction.This also can be done readily by noting that the eigenvector ϕ is a linear combination of ϕ_1 and ϕ_3 such that (Sengupta, 2016)

$$
\begin{aligned}
\phi &= a_1\phi_1 + a_3\phi_3, \\
\phi' &= a_1\phi_1' + a_3\phi_3', \\
\phi'' &= a_1\phi_1'' + a_3\phi_3'', \\
\phi''' &= a_1\phi_1''' + a_3\phi_3'''
\end{aligned}
\tag{4.17}
$$

One can eliminate a_1 and a_3 in many ways. This leads to the following differential equations for ϕ

$$
\begin{aligned}
y_1\phi'' - y_2\phi' + y_4\phi &= 0, \\
y_1\phi''' - y_3\phi' + y_5\phi &= 0, \\
y_2\phi''' - y_3\phi'' + y_6\phi &= 0, \\
y_4\phi''' - y_5\phi'' + y_6\phi' &= 0
\end{aligned}
\tag{4.18}
$$

In principle, having obtained y_1 to y_6 for all y's, it is possible to obtain ϕ by solving any one of the four equations listed above but the presence of four alternatives raises the question of which of these equations is more accurate and consistent for the solution process.

The eigenfunction, ϕ, are found using a suitable linear combination of ϕ_1 and ϕ_3, via equations (4.10), (4.12), (4.13), such that the characteristic roots at free stream (i. e., the solution to equation (4.9)) have a negative real part and the coefficients in the resulting differential equation do not vanish at the centerline. An equation satisfying these constraints was suggested by Davey (Davey, 1980) as follows,

$$
y_4\phi''' - y_5\phi'' + y_6\phi' = 0.
\tag{4.19}
$$

4.4   Results

In our numerical experiments, the zeros of the dispersion relation (equation (4.11), (4.16)) were found in the α/ω plane inside the region $|\omega_r| \leq 1.5, |\omega_i| \leq 1.5, |\alpha_r| \leq 3.0$ and $|\alpha_i| \leq 0.1$, using a discrete step-size of $\Delta\alpha_{r/i} = \Delta\omega_{r/i} = 5 \times 10^{-3}$. The free stream boundary conditions were applied at $\eta = 12$, which leads to the numerical value of the momentum thickness, $\delta = 0.30685$. Numerical integration from the free stream to the shear layer centerline was accomplished via the fourth order Runge Kutta time integration with discrete step-size of $\Delta y = 6.67 \times 10^{-4}$ in the tranverse direction. The eigenfunctions are found by numerically integrating equation (4.19) from the centerline to the free stream starting from the centerline conditions, equation (4.8a). The presence of only two free stream conditions (4.8b) imply that the eigenfunctions are scaled with respect to the centerline value of ϕ' (i .e., $\phi'(0)$). Hence, the results discussed in §4.4.1, 4.4.2, involving these eigenfunctions, are qualitative.

4.4.1   Temporal stability analysis

In this section we explore the stability of the solution of the OSE (equation (4.7)) by exclusively assigning ω to be a complex number. The temporal stability analysis in the inviscid limit was earlier studied by Azaiez (Azaiez and Homsy, 1994a). In this section, we revisit their work and derive similar conclusions in the regime of low to moderate Re and We. In Figure 4.1 we present the curves of the most unstable mode (i. e., ω_i^{Temp}, the largest positive imaginary component of any root of the dispersion relation (4.11)) versus the wavenumber, α_r. Note that, as We is increased, the range of the unstable wavenumbers is reduced and the entire temporally unstable spectrum is shifted towards longer waves (i. e., the region of instability is gradually concentrated around $\alpha_r = 0$). All these observations suggest a mechanism of elastic stabilization in non-Newtonian fluids which we elaborate in this section. Later, in §4.4.2, we outline how the nature of this instability changes from absolute instability to convective instability.

Further characterization of the presence of viscoelasticity on the flow is highlighted via the ratio of the transverse to the streamwise velocity fluctuations (Figure 4.2a) and the variations of the magnitude of the vorticity disturbance (Figure 4.2b). These figures are presented for six different combinations of (Re, We) evaluated at the peak of the most unstable mode $((\alpha^{\text{max}}, \omega^{\text{max}})$, refer Figure 4.1 caption for the respective numerical values). Figure 4.2a depicts the relative strength of the transverse velocity fluctuations versus tranverse spatial coordinates. We remark that at a lower value of We (e. g., $We = 1.0$) these relative fluctuations are significant within the viscous mixing region ($y \leq 1$) whereas at higher We values (e. g., $We = 40.0$) these fluctuations become important outside the mixing layer region and in a region where the fluid is essentially moving at the free-stream velocity (i. e., at $We = 40.0$ the velocity fluctuation ratio attains its maximum at $y \approx 3.8$ where the mean velocity $U_0(y)$ is 99% of its free-stream value). This study indicates the self-enhancing effects of polymer stretching (also known as the relaxation effect) in viscoelastic parallel shear flows of dilute solutions (Larson, Shaqfeh, and Mueller, 1990). This observation is
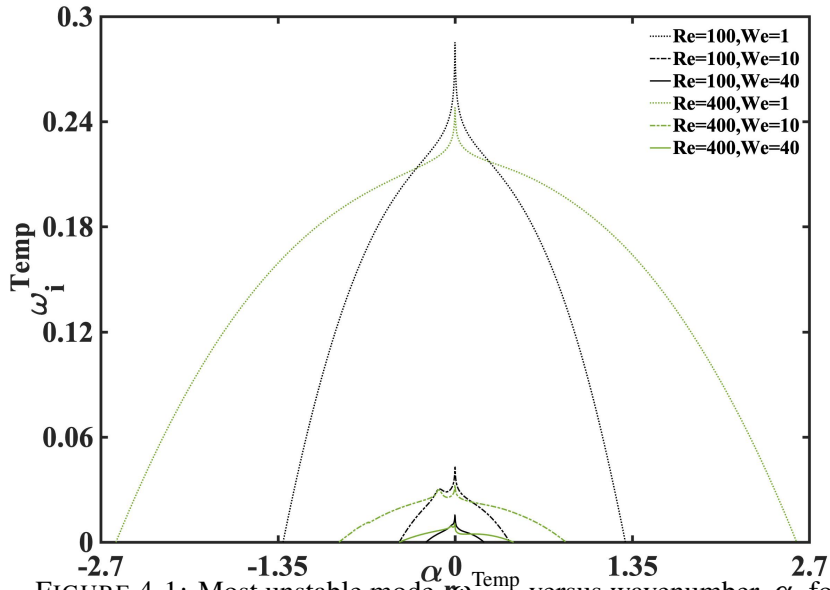
FIGURE 4.1: Most unstable mode, ω_i^{Temp} versus wavenumber, α_r for $We = 1$(dashed curve), $We = 10$ (dash-dotted curve), $We = 40$ (dotted curve) and for $Re = 100$ (black curve), $Re = 400$ (green curve). The peak of these curves are at $\alpha^{\text{max}} = -0.001$ and $\omega^{\text{max}} = 0.784 + 0.285i$ (for $Re = 100, We = 1$); $0.084 + 0.043i$ (for $Re = 100, We = 10$); $0.015 + 0.016i$ (for $Re = 100, We = 40$); $0.795 + 0.248\ i$ (for $Re = 400, We = 1$); $0.070 + 0.032i$ (for $Re = 400, We = 10$); $0.020 + 0.011i$ (for $Re = 400\quad We = 40$). The viscosity coefficient is fixed at $\nu = 0.5$.

further corroborated by observing the magnitude of the vorticity disturbance (Figure 4.2b). While at lower We ($We \leq 10.0$) the region of maximum magnitude of vorticity disturbance is inside the range $y \in [0, 1]$, at higher We this maximum occurs in the range, $y \geq 1$.

More insights about this mechanism of stabilization can be gained by comparing the contours of the rate of vorticity production (drawn at identically equal levels) for an arbitrary time in the streamwise versus transverse direction, at $Re = 400, We = 1.0$ (Figure 4.3a) and $Re = 400, We = 40.0$ (Figure 4.3b) evaluated at the eigenvalues corresponding to the peak of the most unstable mode (refer Figure 4.1 caption). Note that as We increases, the vorticity *structures* become larger and the contour spacing becomes wider. An equivalent outcome can be drawn by examining the root mean square of streamwise velocity fluctuations, $u_{\text{rms}}(0, y)$ (Figure 4.4a) and Residual Reynolds shear stress (Figure 4.4b) at a fixed streamwise location, $x_0 = 0$. Higher We begets a larger u_{rms} (e. g., $u_{\text{rms}} \approx 1.5, 6.0$ at $We = 1.0, 40$ respectively) and a lower residual Reynolds stresses. To summarize, the stretching of the polymers with increasing We brings about a normal stress anisotropy leading to a elastically loaded fluid: when the polymers stretch, elastic energy is stored in the sheared fluid. This energy is released after the fluid element has been adverted to other regions where the shear-induced stretching forces are smaller. Thus, an important mechanism of stabilization via elastic energy transfer is introduced. The same mechanism can be established by observing the variation of the viscoelastic fluid element moving from one region to another as shown in (Bird, Armstrong, and Hassager, 1987), and omitted for brevity.
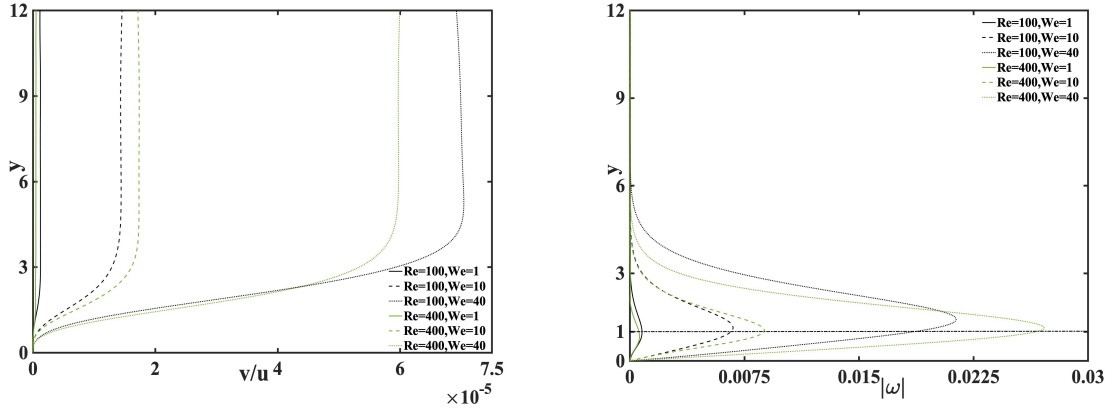
FIGURE 4.2: (a) The ratio of the transverse vs streamwise velocity disturbance, $\dfrac{u}{v} = -\dfrac{\phi'}{\alpha\phi}$ and (b) the variation of the magnitude of the vorticity disturbance, $|\omega| = |\alpha^2\phi - \phi''|$ in the transverse direction (refer equation (5.7)), evaluated at the peak of most unstable mode $(\alpha^{max}, \omega^{max})$ whose values are listed in Figure 4.1 caption. A horizontal line is drawn to distinguish the mixing region, $y \leq 1$. All curves are numerically estimated at the viscosity coefficient $\nu = 0.5$.
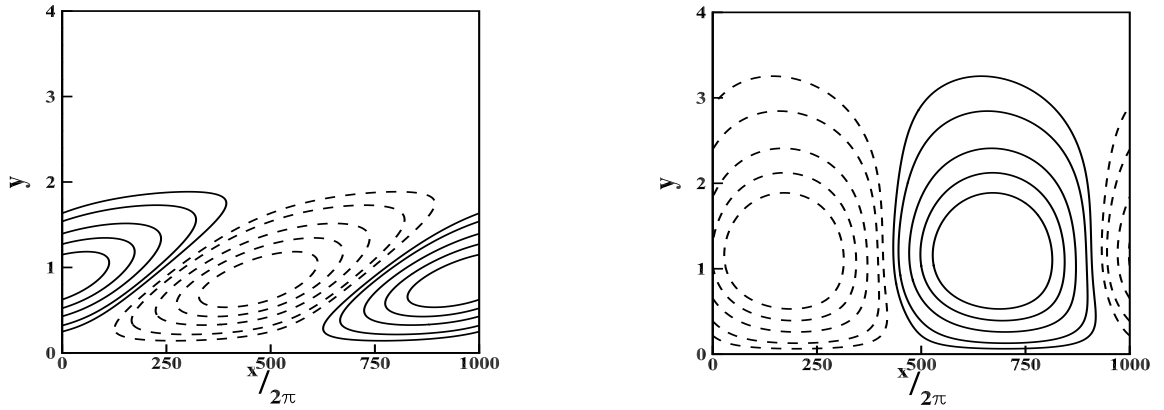
FIGURE 4.3: The rate of vorticity production contours $\dfrac{D\Omega}{Dt}(x, y) = i(D_{yy}\phi - \alpha^2\phi) \quad (\omega - U\alpha)e^{i\alpha x}$ in the streamwise versus transverse direction at (a) $Re = 400, We = 1$, and (b) $Re = 400, We = 40$, evaluated at the peak of the most unstable mode (refer Figure 4.1 caption). The contours are drawn at identically equal levels and the viscosity coefficient is fixed at $\nu = 0.5$ in both cases.
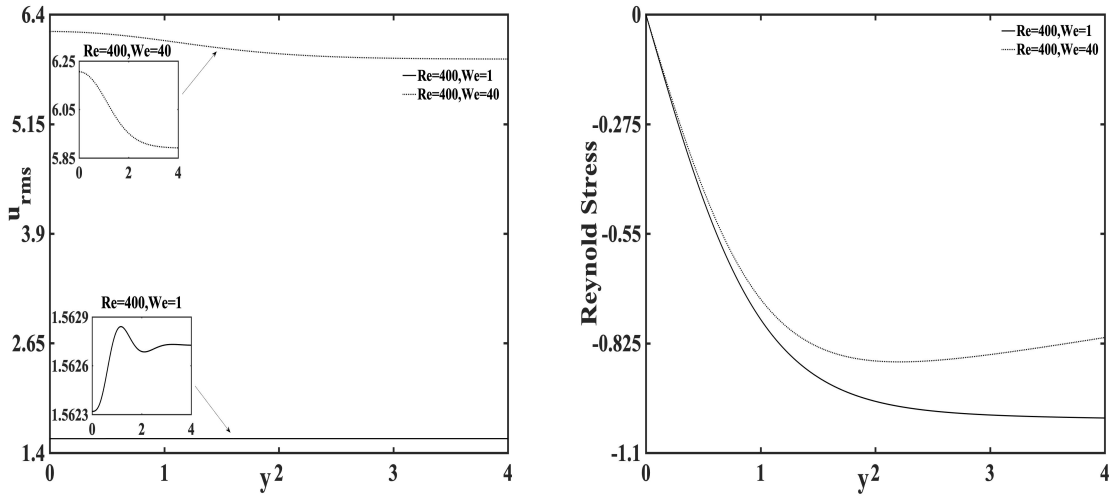
FIGURE 4.4: (a) Streamwise root mean square velocity fluctuations,

$$u_{\mathrm{rms}}(0,y) = \sqrt{\frac{1}{T}\int_0^T [u'(0,y,t)]^2 dt}$$ and (b) Residual Reynolds shear

stress $= \frac{1}{T}\left(\int_0^T (U(y)+u'(0,y,t))v'(0,y,t)dt\right) - U(y)$ evaluated at
a fixed streamwise location, $x_0 = 0$ and at the peak of the most un-
stable mode (refer Figure 4.1 caption). The inset in (a) shows the
maximum variation in $u_{\mathrm{rms}}(x,y)$ at $y \approx 1$, the edge of the mixing
layer. $u'(x,y,t)$ and $v'(x,y,t))$ are the streamwise and transverse ve-
locity fluctuations (equation (5.7)) at $Re = 400, We = 1$ (solid curve),
$Re = 400, We = 40$ (dotted curve) and at fixed viscosity coefficient,
$\nu = 0.5$. $U(y)$ is the mean flow (equation (4.4)). $T = (2\pi/\omega_r^{\mathrm{max}})$ is one
time period and ω_r^{max} is the real part of the angular frequency at the
peak of the most unstable mode.

4.4.2   Spatio temporal stability analysis

The spatio temporal analysis, where both ω and α are designated as complex numbers, is a step which is necessary to reveal the stability phase diagram in the flow-material parameter space (i. e., in the (Re, We, ν)-space, Figure 4.8). In the onset, we demonstrate an example of a cusp point in the ω-plane (Figure 4.5a) and the saddle point in the α-plane (Figure 4.6) which correspond to each other via the local angle-doubling map as indicated by Kupfer (Kupfer, Bers, and Ram, 1987) (details in § 4.2.2). To this end, a particular set of parameters are chosen for which the flow is absolutely unstable: $Re = 100, We = 1, \nu = 0.9$. First, the image of the dispersion relation at $\alpha_i = 0$ is obtained (Figure 4.5a). This curve is the root of the dispersion relation (equation (4.11)) with the maximum positive imaginary component of the frequency, ω_i^{max}, as outlined in §4.4.1. As we decrease the imaginary component of the wavenumber (for downstream mode in this example), the corresponding image in the ω-plane is observed. When α_i is sufficiently negative (e. g., $\alpha_i = -0.0301$), we detect the appearance of the cusp point at $\omega^{\text{cusp}} = 0.6268 + 0.2362i$. The pinch point in the α-plane (which is also the saddle point) corresponding to the cusp point in the ω-plane arises at $\alpha^{\text{pinch}} = -0.041 - 0.0301i$ (Figure 4.6). The pinch point is obtained by drawing the isocontours of ω_r (Figure 4.6a) and ω_i (Figure 4.6b) in the α-plane. Consequently, by drawing a ray parallel to the ω_i axis (Figure 4.5a), we note that this ray intersects $\alpha_i = 0$ curve only once (i. e., odd number of times), implying that the cusp point is genuine. Since the imaginary component of this cusp point is positive ($\omega_i^{\text{cusp}} = 0.2362$), the free shear viscoelastic fluid flow at $Re = 100, We = 1, \nu = 0.9$ is absolutely unstable.

Evanescent modes are also encountered in our analysis and to illustrate their existence we consider another example of the cusp point formation at $Re = 100$, $We = 1$ $\nu = 0.5$ (Figure 4.5b). In this case, a ray emerging from the cusp point and parallel to the ω_i axis, intersects the $\alpha_i = 0$ curve twice (i. e., even number of times), thereby establishing that this cusp point corresponds to an evanescent mode. Evanescent modes (also known as the direct resonance mode (Koch, 1986)) arises if the two coalescing modes (given by the solution to equation (4.7)) originate from waves propagating in the same direction (detailed discussion in §4.2.2). Linear stability theory predicts that these disturbances decay in the asymptotic limit of long time, but in the short term an algebraic growth associated with such a mode may be decisive to cause the transition to turbulence in receptivity studies (Lingwood, 1997).

In order to determine the range of Re (for fixed ν, and different We) for which the flow regimes are absolutely unstable, convectively unstable or temporally stable, we plot the absolute growth rate in Figure 4.7 (i. e., ω_i^{cusp}, which is the growth rate at the cusp point obtained by deforming the Fourier contour in the α-plane starting from the most unstable temporal mode, ω_i^{Temp} (refer §4.4.1 for finding the most unstable mode), as explained in the above two examples. We define Re_s (We_s) as the maximum critical Reynolds number (minimum critical Weissenberg number) for the flow to be temporally stable. Notice that the magnitude of the absolute growth rate (wherever it exists) predominantly decreases with increasing Re and with increasing We. Although the combined effect of these parameters on the flow stability are often reported in terms of the elasticity number ($E_l = We/Re$, which corresponds to the ratio of the time scale for the elastic stress evolution to the time scale for diffusion
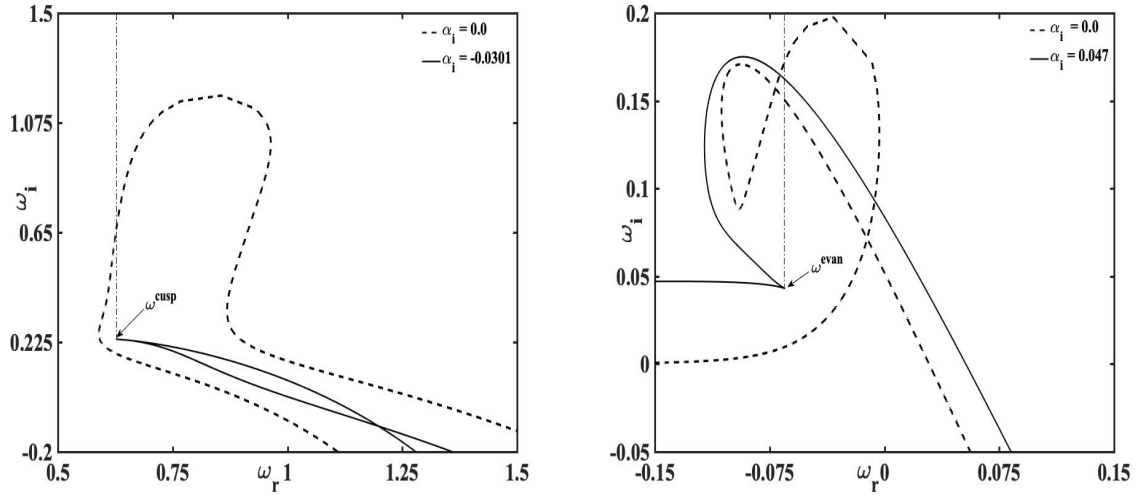
FIGURE 4.5: (a) Cusp point formation in $\omega-$plane for $Re = 100, We = 1, \nu = 0.9$. The cusp point is formed at $\omega^{cusp} = 0.6268 + 0.2362i$ with the corresponding pinch point at $\alpha^{pinch} = -0.041 - 0.0301i$. The ray drawn from the cusp point, parallel to the y-axis intersects the $\alpha_i = 0$ curve once (odd number of times), indicating a genuine cusp point, (b) Evanescent mode formation for $Re = 100, We = 1, \nu = 0.5$ at $\omega^{evan} = -0.0649 + 0.0430i$ and with the corresponding pinch point at $\alpha^{pinch} = -0.038 + 0.047i$. The ray drawn from this cusp point, parallel to the y-axis intersects the $\alpha_i = 0$ curve twice (even number of times).
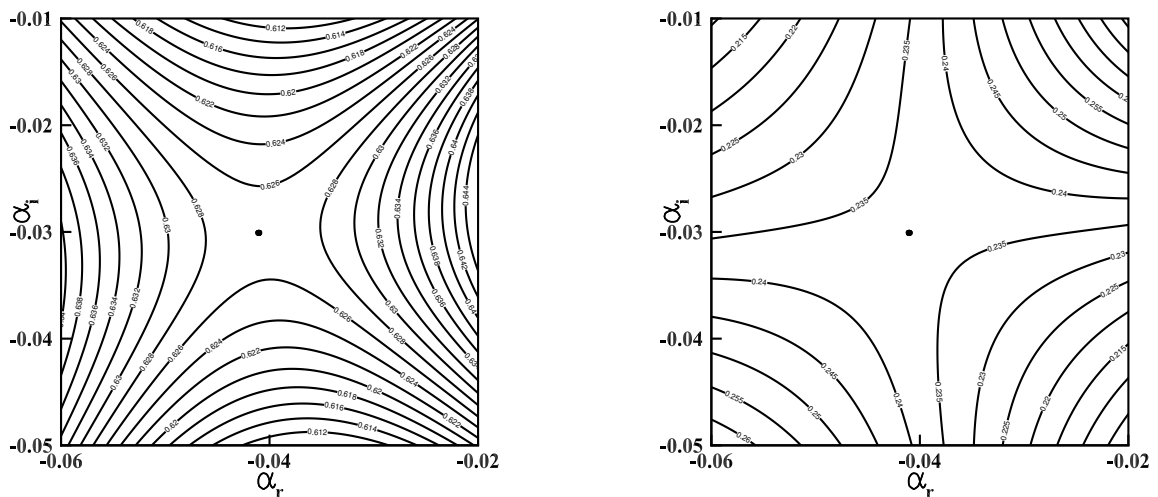
FIGURE 4.6: The pinch point, $\alpha^{pinch} = -0.041 - 0.0301i$, in the $\alpha-$plane corresponding to the cusp point as outlined in Figure 4.5a for $Re = 100, We = 1, \nu = 0.9$, which are demonstrated by drawing the iso-contours of (a) ω_r and (b) ω_i.

of momentum (Azaiez and Homsy, 1994a)), we elaborate the impact of these flow-material parameters via the stability phase-diagram, discussed next.
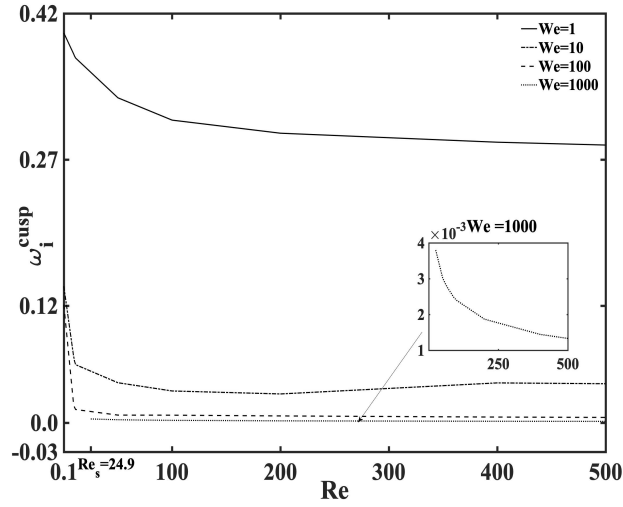
FIGURE 4.7: The cusp points, ω_i^{cusp} versus Re in regions of convective and absolute instabilities calculated at the viscosity coefficient $\nu = 0.35$.

We depict the boundaries of the temporally stable regions (**S**), convective instabilities (**C**), evanescent modes (**E**) and absolute instabilities (**A**) within a selected range of flow-material parameter space, i. e., $Re \in [0.1, 500]$, $We \in [1, 1000]$ and $\nu = 0.35$ (Figure 4.8a), $\nu = 0.20$ (Figure 4.8b). While We is similar to the Deborah number and is often confused with it in technical literature of dilute polymeric flows (Bird, Armstrong, and Hassager, 1987), they have different physical interpretations. *We* indicates the degree of anisotropy or orientation generated by the deformation and is appropriate to describe flows with a constant stretch history such as simple shear flows. In contrast, the Deborah number is used to describe flows with a non-constant stretch history, and physically represents the rate at which elastic energy is stored or released (Bird et al., 1987). The boundaries of temporally stable regions are estimated to reside within the range $We \in [We_s = 505, 1000]$, $Re \in [0.1, Re_s = 24.9]$ at $\nu = 0.35$ (refer Figure 4.8a) and $We \in [We_s = 455, 1000]$, $Re \in [0.1, Re_s = 20.1]$ at $\nu = 0.20$ (refer Figure 4.8b), respectively. The linear stability phase diagram for the free shear flow systems dominated by viscous stresses (i. e., the case in which $\nu > 0.35$), have revealed a similar transition scenario as highlighted in Figure 4.8a, 4.8b within an identical range of Re, We. Hence, the discussion of those phase diagrams are omitted in this chapter. Two conclusions can be deduced from these phase diagrams. First, since the boundary of the absolutely unstable region, (**A, E**), is not parallel to the y-axis, the authors surmise that the flow will be absolutely unstable for sufficiently high Re and irrespective of We. This assertion is supported by previous numerical studies of inviscid viscoelastic mixing layer in the limit of high Re, We such that the elasticity number is held fixed and finite (Azaiez and Homsy, 1994a). Second, unlike Newtonian fluids, viscoelastic liquids are either (absolutely/convectively) unstable for all Re (e. g., consider the region $We < 455$ in Figure 4.8a and 4.8b) or the transition to instability occurs at very low Re (e. g., $Re_s = 24.9, 20.1$ at $\nu = 0.35, 0.20$ and $We = 1000$, respectively). Further in the latter case, the transition is direct from temporally stable

region to absolutely unstable region for viscous stress dominated fluids (i. e., the case of $v = 0.35$, Figure 4.8a) while this transition is more gradual, $\mathbf{S} \to \mathbf{C} \to \mathbf{A}$ for elastic stress dominated fluids (i. e., the case of $v = 0.20$, Figure 4.8b). Although absolute instability is far more vicious than convective instability as the occurrence of absolute instability pervades the entire flow domain, convective instability can also cause transition to turbulence if sufficient spatial distance is given for the disturbance to grow (Huerre and Monkewitz, 1990). The second conclusion can be attributed to the fact that viscoelasticity dramatically exacerbates free shear flow instabilities arising from a combination of normal stress anisotropy and elasticity (Larson, 2000).
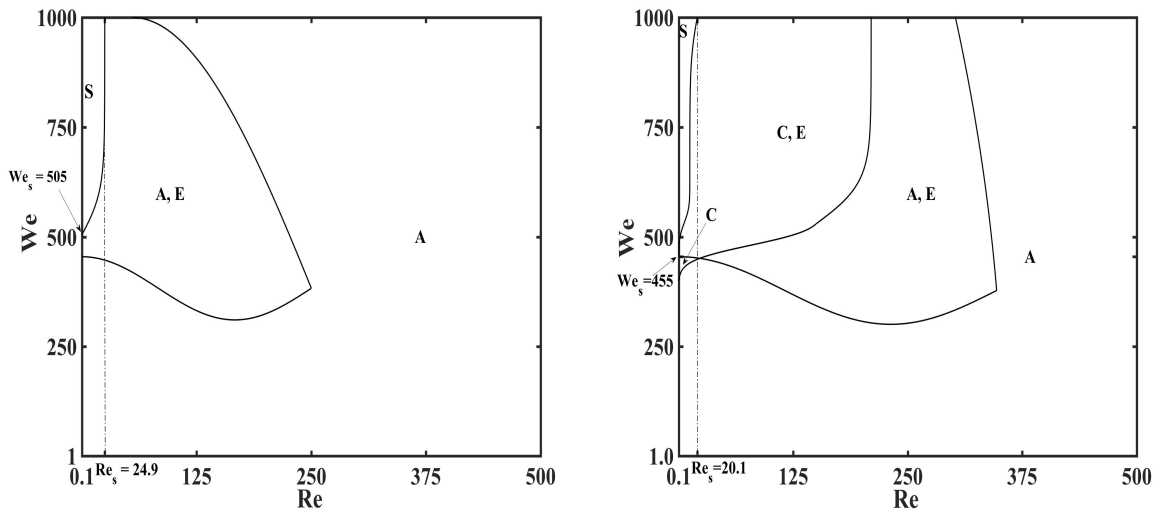
FIGURE 4.8: Viscoelastic free shear layer stability phase-diagram at (a) $v = 0.35$ and (b) $v = 0.20$, in the Re-We parametric space. The regions **S, C, A** are denoted by temporally stable, convectively unstable and absolutely unstable regions, respectively. The domains outlined by **A, E** and **C, E** are those where both the unstable and evanescent modes (denoted by **E**) are found.

We recapitulate our discussion by indicating some experimental findings which corroborate our numerical results, starting from the systematic studies of viscoelastic Taylor-Couette flows in 1990 by Larson (Larson, Shaqfeh, and Mueller, 1990). The important interpretation that emerged from their work and later extensions (Larson, 2000) was that when inertial effects are unimportant, viscoelastic flows can exhibit an elasticity driven instability and with appropriately prepared model polymer solutions, one can make quantitative contact between experiments and theoretical predictions using Oldroyd-B constitutive relation. More relevant experiments which will be analytically tackled (in our future research work) via the linear spatio temporal treatment outlined in this section, are the surface buckling instability (or the azimuthal compression in an inward radial flow) studies of an Oldroyd-B fluid (Podgorski and Belmonte, 2002), the viscoelastic RTI (Graham, 2003), the Rayleigh-Plateau, Saffman-Taylor and the Faraday instabilities (Lindner and Wagner, 2009).

4.5 Conclusions

This investigation addresses the linear, temporal and spatio temporal analyses of free shear flows of dilute polymeric liquids with anti-symmetric centerline conditions for low to moderate *Re* and *We*. §4.2 presented the free shear viscoelastic flow as well as the elements of the linear stability analysis via the solution of the Orr Sommerfeld equation, including the illustration of the Briggs contour integral method to determine the existence of absolutely unstable, convectively unstable and evanescent modes. §4.3 demonstrated the steps of the Compounded Matrix Method, utilized to numerical solve the resultant system of stiff differential equations. The numerical outcome, in a selected range of *Re* and *We*, highlight that with increasing *We* the region of temporal instability is gradually concentrated near zero wavenumber, the vorticity structures of the disturbance become larger and more widely spaced and the residual Reynolds stresses are lowered, all these observations indicating a mechanism of elastic stabilization in non-Newtonian free shear flows of dilute solutions. The spatio temporal analysis reveal that either the flow is unstable for all *Re* or the transition to instability transpires at comparatively low *Re* stipulating the significance of the intimately connected normal stress anisotropy, elasticity and the slow relaxation effects. Although the Oldroyd-B model describes well the behavior of polymeric liquids composed of a low concentration of high molecular weight polymer in a very viscous Newtonian solvent at moderate shear rates, more realistic description of polymeric solution and melts, including the effect of shear thinning, non-zero normal stress coefficient and stress overshoot in transient flows is missing and hence deserves a full numerical exploration in the near future, using a constitutive relation which incorporates these above mentioned features.

Chapter 5

Spatiotemporal linear stability of viscoelastic free shear flows: non-affine response regime

5.1 Introduction

The understanding of the hydrodynamic stability and the flow transition in free shear flows of viscoelastic liquids has continued to receive prolonged interest due to its practical applications in microfluidic mixing (Squires and Quake, 2005), viscoelastic stabilization via polymer addition (White and Mungal, 2008) and in shearing flows of viscoelastic biofluids, like mucus (Sircar and Roberts, 2016a), cartilage (Sircar et al., 2015) and adhesion-fragmentation transition in cells (Sircar and Bortz, 2013; Sircar, Younger, and Bortz, 2014; Sircar and Roberts, 2016b; Sircar et al., 2016). Most investigations of low to moderate Reynolds number (*Re*) have either focused on the linearized studies (Ray and Zaki, 2014), experimental analysis (Groisman and Steinberg, 1998) or the full Direct Numerical Simulations (DNS) (Yu and Phan-Thien, 2004) of the affine response of dilute polymeric liquids. However, in semi-dilute or moderately concentrated polymeric liquids, instabilities may arise due to flow induced inhomogeneities, and an improved understanding of the transition pathway of the non-affine or the non monotonic flow response in (but not limited to) strong elongational flow, is expedient.

The concepts of absolute and convective instabilities are well established to study the evolution of impulse disturbances in Newtonian flows. Absolute instability was earlier experimentally verified by Shoji *et. al* (Shoji et al., 2020) in liquid jets. There is also an extensive literature on Newtonian wakes and mixing layers, including the blunt body experiments listed by Oertel (Oertel, 1990), the linear analysis by Chomaz (Delbende and Chomaz, 1998) and Healy (Healy, 2009) and the DNS studies by Pier (Pier, 2008). Overall, these studies found a destabilizing effect of finite boundaries and an existence as well as a transition to absolute instability in the near wake region.

The spatiotemporal analysis of viscoelastic free shear layers (a transition region between two stream of different velocity) are more recent and scarce. An early experimental study by Vihinen *et. al* (Vihinen, Honohan, and Lin, 1997) reported absolute instability in viscoelastic liquid jets. Pipe reported a stabilizing effect of polymer addition in his experiments on viscoelastic cylindrical wakes, which is counteracted by shear thinning and a transition from convective to absolute instability at higher

polymer concentrations (Pipe, 2005). In contrast, the linear analysis of dilute mixing layers (Ray and Zaki, 2014) and dilute jets (Ray and Zaki, 2015; Alhushaybar and Uddin, 2019; Alhushaybari and Uddin, 2020) relay a significant range of parameters where viscoelasticity was found to be destabilizing. A recent DNS study of jets (M. C. Guimaraes and Silva, 2020) necessitates the use of an extra (convective) timescale to characterize the memory fading property of viscoelastic fluids.

In this Chapter, we have limited our focus on the linear spatiotemporal analyses of viscoelastic free shear layer, mainly within the regime of non-affine / non monotonic flow response. We characterize the fluid flows as being absolutely or convectively unstable and utilize the method of spatiotemporal analysis by progressive moving of the isocontours in the complex frequency and wavenumber plane, as proposed by Kupfer (Kupfer, Bers, and Ram, 1987). The next section describes the model of the viscoelastic free shear layer flow coupled with four constitutive relations for the extra elastic stress tensor for simultaneous comparison of results: Oldroyd-B, Upper Convected Maxwell (UCM), Johnson-Segalman (JS) at the slip parameter value, $a = 0.5$, and the linear Phan-Thien and Tanner (PTT) model at $a = 0.5$ and the elongation parameter explored within the range $\varepsilon \in [0, 0.99]$, although a detailed study is predominantly conducted at $\varepsilon = 0.5$ (§5.2.1) as well as the details of the linear stability analysis leading upto the fourth order Orr-Sommerfeld equation (OSE) (§5.2.6). §5.3 introduces the Compound Matrix Method (CMM) to numerically solve the resultant system of stiff ordinary differential equations (ODE) emerging from the OSE, rewritten in terms of the auxiliary variables. §5.4 showcases the simulation results including numerical method validation (§5.4.1), the temporal (§5.4.2) and the spatiotemporal stability analyses (§5.4.3), followed with a brief discussion on the implication of these results as well as the focus of our future direction (§5.5).

5.2 Mathematical model and linear stability analysis

Unlike Newtonian solvents, the transition to instability in polymeric liquids depends on the details of the equations relating stress to the shear rate. The linear PTT model properly describes the non-affine behavior of polymeric liquids composed of a low to moderate concentration of high molecular weight polymer in a very viscous Newtonian solvent at moderate shear rates, including the effect of shear thinning, non-zero normal stress coefficient and stress overshoot in transient flows (Yu and Phan-Thien, 2004). Further, this model predicts finite stress at finite strain rates for strong elongation flow, a feature which is achieved by constraining the length of the polymer chain to a maximum allowable length. The numerical solution obtained by linearizing the Navier Stokes along with the extra stress constitutive equation is reliable in describing the characteristics of the initial stages of the mixing layer transition (Bird, Armstrong, and Hassager, 1987). Hence, the linear stability results can be utilized as the initial-boundary conditions for Direct Numerical Simulation (Yu and Phan-Thien, 2004) or the Large Eddy Simulation of polymeric liquids (Steinberg, 2018) in order to further study the flow evolving process downstream.

5.2.1 Mathematical model

The continuity and the momentum equations for an incompressible flow in a free shear flow configuration are as follows,

$$\nabla \cdot \mathbf{v} = 0, \tag{5.1a}$$

$$\rho \frac{D\mathbf{v}}{Dt} = -\nabla p + \nabla \cdot \tau, \tag{5.1b}$$

where $\mathbf{v}$ is the velocity vector, ρ the density, p the isotropic pressure and τ the extra stress tensor, which is written as the sum of the viscous, Newtonian stress, τ^s $(= \eta_s \mathbf{D}$, where $\mathbf{D} = \nabla \mathbf{v} + \nabla \mathbf{v}^T$ is the rate of strain tensor) and the elastic stress, τ^p $(= \eta_p \mathbf{A})$. η_s, η_p are the solvent viscosity and the polymeric contribution to the shear viscosity, respectively. Introducing the parameters, $\eta (= \eta_s + \eta_p)$ and $\nu (= \eta_s / \eta)$, representing the total viscosity and the viscous contribution to the total viscosity, respectively, the extra stress tensor can be rephrased as follows,

$$\tau = \eta [\nu \mathbf{D} + (1 - \nu)\mathbf{A}]. \tag{5.2}$$

The tensor $\mathbf{A}$ satisfies the linear PTT equation (Yu and Phan-Thien, 2004),

$$(1 + \varepsilon \lambda \,\mathrm{tr}\mathbf{A})\mathbf{A} + \lambda \frac{DA}{Dt} = \mathbf{D}, \tag{5.3}$$

where the Gordon-Schowalter convected derivative, $\dfrac{DA}{Dt}$, is,

$$\frac{DA}{Dt} = \frac{\partial \mathbf{A}}{\partial t} + \mathbf{v} \cdot \nabla \mathbf{A} - \frac{1}{2}(\mathbf{W}^T + a\mathbf{D}) \cdot \mathbf{A} - \frac{1}{2}\mathbf{A} \cdot (\mathbf{W} + a\mathbf{D}). \tag{5.4}$$

$\mathbf{W} = (\nabla \mathbf{v} - \nabla \mathbf{v}^T)$ is the vorticity tensor, λ is the polymer relaxation time, a is a slip parameter characterizing the non-affine motion of the chains and $\varepsilon \in [0, 1]$ is a dimensionless parameter describing the maximum elongation of the polymer chains.

5.2.2 Oldroyd-B model

For $\varepsilon = 0, a = 1$ the motion is affine and the Johnson-Segalman model reduces to the Oldroyd-B model. The Oldroyd-B model describes well the behavior of polymeric liquids composed of a low concentration of high molecular weight polymer in a very viscous Newtonian solvent at moderate shear rates. But this constitutive relation fails in many circumstances, e. g., it fails to predict the physical value of the viscosity in extensional flow when the relaxation time of the polymer times the extension rate exceeds 0.5 (or when the elongational flow is strong enough to drive the two sides of the polymer dumbbell infinitely far apart from one another) (Bird et al., 1987). The other three models are also described as follows.

5.2.3 Upper Convected Maxwell model

An exception to the Oldroyd-B model is the UCM fluid ($\varepsilon = 0, a = 1, \nu = 0$), a case where the extra stress tensor is purely elastic. A UCM liquid predicts a quadratic shear rate dependence of the first normal stress difference and zero second normal

stress difference (which is a realistic behavior of polymer melts at moderated shear rates (Bird, Armstrong, and Hassager, 1987)), but a constant shear viscosity (or no shear thinning behavior). The upper-convected Maxwell (UCM) model is a generalisation of the Maxwell material for the case of large deformations using the upper-convected time derivative. The model was proposed by James G. Oldroyd. The concept is named after James Clerk Maxwell. The model can be written as:

$$\frac{\partial A}{\partial t} + \mathbf{v} \cdot \nabla \mathbf{A} - \nabla \mathbf{v}^T \cdot \mathbf{A} - \mathbf{A} \cdot \nabla \mathbf{v} = \frac{\mathbf{D} - \mathbf{A}}{\lambda}, \quad\quad (5.5)$$

where $\mathbf{A}$ is the stress tensor, $\mathbf{v}$ is the velocity vector and λ is the polymer relaxation time.

In the case of steady shear, the upper-convected Maxwell model predicts for the simple shear that shear stress to be proportional to the shear rate and the first difference of normal stresses $(T_{11} - T_{22})$ is proportional to the square of the shear rate, the second difference of normal stresses $(T_{22} - T_{33})$ is always zero. In other words, UCM predicts appearance of the first difference of normal stresses but does not predict non-Newtonian behavior of the shear viscosity nor the second difference of the normal stresses. In case of start-up of steady shear, the equation is only applicable, when the velocity profile in the shear flow is fully developed. Then the shear rate is constant over the channel height. If the start-up form a zero velocity distribution has to be calculated, the full set of PDEs has to be solved. In this case, only two components of the shear stress became non-zero for the UCM model. For the case of small deformation the nonlinearities introduced by the upper-convected derivative disappear and the model became an ordinary model of Maxwell material.

The UCM model recaptures all of the linear viscoelastic modelling and show Newtonian / Neo-Hookean behavior for the limiting case (slow / fast flow). Contrary to this, UCM model follows no shear rate dependence of viscosity and first normal stress difference (i.e no shear thinning) and the extensional thickening is too severe in this model. This model works for very dilute solutions ($< 0.5\%$ concentration) and dilute solutions with very high solvent viscosities (*Boger fluids*).

5.2.4   Johnson-Segalman model

The Johnson-Segalman (JS) fluid (an illustration of this model is highlighted via a fixed slip parameter, $a = 0.5$ and $\varepsilon = 0$) allows for a non-monotonic relationship between the shear stress and rate of shear in a simple shear flow, consequently explaining the 'spurt' phenomena or a dramatic increase of the volumetric flow rate (equivalently a jump in the strain rate) at a critical stress which is independent of molecular weight of the polymer (Malkus, Nohel, and Plohr, 1991). The equation for JS model is described in equation (5.4), where the left-hand-side of the equation is known as the Gordon-Schowalter (GS) convected derivative, in JSO models the nonaffine motion of polymer chains. They are not locked into a rubber network, which deforms with the flow, but rather the chains are allowed to slip past the continuum.

For $a = 1$ the motion is affine, and JS reduces to the Oldroyd-B model, which for $\mu_s = 0$ is the same as the upper-convected Maxwell model. Decreasing a increases the slippage, and softens the response of the material by increasing shear-thinning in shear flows, and reducing strain hardening in extensional flows. (The slip-parameter a should be restricted to $0.2 < a < 0.89$ for consistency with experiments using dilute solutions of a variety of commercial polymers. The ratio of the second normal stress difference to the first, equal to $-(1-a)/2$ for JS, was found to lie between -0.40 and -0.055, and to be independent of the shear-rate).

5.2.5 Phan-Thien Tanner model

Finally, the PTT model is derived from the Lodge-Yamamoto network theory by Phan-Thein and Tanner (Thien and Tanner, 1977). The model is an extension of the UCM model with the Gordon-Schowalter convected derivative written to include a function dependent on the trace of the polymer stress. The linear PTT model (illustrated via the model parameters $a = 0.5, \varepsilon \in [0, 0.99]$) is based on finitely extensible springs; it does reproduce shear-thinning and generally captures the instability transition more accurately than the Oldroyd-B as well as the JS model (Yu and Phan-Thien, 2004). Both the linear and exponential forms of the PTT model are extensively used (Thien, 1978). The quadratic form is far less widely mentioned in literature, but is used to model the wire-coating process (Ngamaramvaranggul and Webster, 2002). Both the affine ($a = 0$) and the non-affine ($a \neq 0$) PTT models are found in literature but the simpler affine model is more prevalent in the study of contraction and re-entrant corner flows (Evans, 2010). The PTT model improves upon the UCM model for modeling polymeric fluids since the UCM model over predicts stresses at large deformation rates, along with obtaining a closer fit to the real world normal stress differences.

5.2.6 Linear Stability Analysis

Consider the free-stream velocity in a frame moving with the average flow velocity, i. e., U ($= \frac{1}{2}(\mathscr{U}_1$ - $\mathscr{U}_2$), where $\mathscr{U}_1(\mathscr{U}_2)$ is the free-stream velocity of the upper(lower) flow), and the momentum thickness, δ (Azaiez and Homsy, 1994a). Utilizing U, δ as the reference velocity and the length scale, respectively, we nondimensionalize equation (5.1) and introduce the the dimensionless numbers, $Re = \rho \delta U / \eta$ and the Weissenberg number, $We = \lambda U / \delta$. Assuming that the mean flow is two-dimensional (with x and y being the streamwise parallel and transverse directions in space, respectively) and quasi-parallel with its variation entirely in the transverse direction, i. e.,

$$U(y) = \tanh(y), \ \Omega(y) = \tanh^2(y) - 1, \ \Psi(y) = \log(\cosh(y)), \qquad (5.6)$$

where $U(y), \Omega(y), \Psi(y)$ are the dimensionless streamwise parallel mean velocity (with zero transverse component), mean vorticity and the associated streamfunction, respectively. Further, assuming that the mean flow supports a two-dimensional disturbance field, the streamfunction and the extra stress tensor are represented by

the base state profile $(\Psi(y), \tau_0(y))$ plus a small perturbation, which is Fourier transformed in x and t as follows,

$$\psi(x,y,t) = \Psi(y) + \phi(y)e^{i(\alpha x - \omega t)},$$
$$\tau(x,y,t) = \tau_0(y) + \varphi(y)e^{i(\alpha x - \omega t)}, \tag{5.7}$$

where $\phi(y), \varphi(y)$ are the transverse perturbations in the streamfunction and the extra stress tensor and α, ω are the complex wavenumber and angular frequency, respectively. We note that equation (5.6) is a solution of the momentum equations for incompressible flow provided there is a dimensionless body force term on the right-hand-side of equation (5.1b) (Sircar and Bansal, 2019). We rephrase equations (5.1-5.4) in the streamfunction-vorticity formulation and avail equation (5.7) to arrive at the equation governing the perturbation of the streamfunction, given by the fourth order OSE (Azaiez and Homsy, 1994a).

$$\left\{ i\left[(\alpha U - \omega)(D^2 - \alpha^2) - \alpha D^2 U\right] - \frac{\nu}{Re}(D^2 - \alpha^2)^2 \right\}\phi = \frac{1-\nu}{\mathscr{F}Re}\sum_{n=0}^{4} c_n D^n \phi. \tag{5.8}$$

where $D^n(\cdot)$ denote the nth derivative of any variable function with respect to y, $D = {}^{d}/{}_{dy}$, $\mathscr{F} = 4d_0^3\left[aS_1S_2 + S_1S_3 + (1-a^2)S_1^2\right]^2\left[S_3 + (1+a)S_1\right]^2$ and the coefficients c_i's are listed as follows:

$$\begin{aligned}
c_0 &= \frac{-4(S_3 + (1+a)S_1)^2}{(4S_0^2 d_0^3(S_3 + (1+a)S_1)^2)}\Big[\big[S_0^2\big\{(D^2\tilde{A})d_0^2 - \tilde{A}d_0(D^2 d_0) - 2(D\tilde{A})d_0(Dd_0) + 2\tilde{A}(Dd_0)^2 + \alpha^2\tilde{A}d_0^2\big\} \\
&\quad + 2(1-a^2)i\alpha\big\{S_0\big((D^2U)(S_1 + S_3) + (DU)(DS_1 + DS_3)\big) - (DU)(S_1 + S_3)(DS_0)\big\}(\tilde{A})d_0^2 + 2(1- \\
&\quad a^2)i\alpha(DU)(S_1 + S_3)S_0\big\{(D\tilde{A})d_0^2 - 2\tilde{A}d_0(Dd_0)\big\}\big] + d_0^3\big[2S_0(S_3 + (1+a)S_1)\big\{2(S_1 + S_3)(S_2 - (1+ \\
&\quad a)S_1) + 1 + 2(S_3 + (1+a)S_1)(S_1 + S_3)\big\}i\alpha(1+a)(D^2\tau_0^{22}) + \big\{(2(S_1 + S_3)(S_2 - (1+a)S_1) + 1) - \\
&\quad 2(S_1 + S_3)(S_3 + (1+a)S_1)\big\}i\alpha(1-a)(D^2\tau_0^{11}) + \big\{(2(S_1 + S_3)(S_2 - (1+a)S_1) + 1)a + (S_1 + S_3) \\
&\quad (S_3 + (1+a)S_1)(1+a^2)\big\}4\alpha^2(D\tau_0^{12}) + 2\big\{2S_0(S_3 + (1+a)S_1)((DS_1 + DS_3)(S_2 - (1+a)S_1) + \\
&\quad (S_1 + S_3)(DS_2 - (1+a)DS_1)) - (2(S_1 + S_3)(S_2 - (1+a)S_1) + 1)((DS_0)(S_3 + (1+a)S_1) + S_0 \\
&\quad (DS_3 + (1+a)DS_1))\big\}(i\alpha((1+a)D\tau_0^{22} + (1-a)D\tau_0^{11}) + 4a\alpha^2\tau_0^{12}) + 4\big\{S_0(S_3 + (1+a)S_1)^2 \\
&\quad (DS_1 + DS_3) - (S_3 + (1+a)S_1)(S_1 + S_3)((DS_0)(S_3 + (1+a)S_1) + 2S_0(DS_3 + (1+a)DS_1))\big\} \\
&\quad (i\alpha((1+a)(D\tau_0^{22}) - (1-a)(D\tau_0^{11})) + 2(1+a^2)\alpha^2\tau_0^{12}) + 4S_0(S_3 + (1+a)S_1)(S_1 + S_3)(DS_3 \\
&\quad + (1+a)DS_1)(i\alpha((1+a)D\tau_0^{22} - (1-a)D\tau_0^{11}) + 2a\alpha^2\tau_0^{12})\big]\Big], \tag{5.9a}
\end{aligned}$$

$$c_1 = \frac{-4(S_3 + (1+a)S_1)^2}{(4S_0^2 d_0^3 (S_3 + (1+a)S_1)^2)} \left[\left[(S_0)^2 \left\{ 2(D\tilde{A})d_0^2 + (D^2\tilde{B})d_0^2 - \tilde{B}d_0(D^2 d_0) - 2(\tilde{A})d_0(Dd_0) - 2(D\tilde{B}) \right. \right. \right.$$

$$d_0(Dd_0) + 2(\tilde{B})(Dd_0) + \alpha^2 \tilde{B}d_0^2 \Big\} + 2(1-a^2)(i\alpha) \left\{ S_0((D^2U)(S_1 + S_3) + (DU)(DS_1 + DS_3)) - \right.$$

$$(DU)(S_1 + S_3)(D(S_0)) \Big\} \tilde{B}d_0^2 + 2(1-a^2)(i\alpha)(DU)(S_1+S_3)S_0 \left\{ (\tilde{A} + D\tilde{B})d_0^2 - (\tilde{B})d_0(Dd_0) \right\} \Big] + d_0^3$$

$$[2S_0(S_3 + (1+a)S_1) \left\{ (2(S_1 + S_3)(S_2 - (1+a)S_1) + 1 + 2(S_3 + (1+a)S_1)(S_1 + S_3))(i\alpha)(1+a)(1 \right.$$

$$- 2a)D\tau_0^{22} + (2(S_1 + S_3)(S_2 - (1+a)S_1) + 1 - 2(S_1 + S_3)(S_3 + (1+a)S_1))i\alpha(1-a)(1+2a)D\tau_0^{11}$$

$$+ (2a(S_1 + S_3)(S_2 - (1+a)S_1) + (S_1 + S_3)(S_3 + (1+a)S_1)(1+a^2))4\alpha^2\tau_0^{12} \Big\} + 2 \left\{ (DS_1 + DS_3) \right.$$

$$(S_2 - (1+a)S_1) + (S_1 + S_3)(DS_2 - (1+a)DS_1) - ((DS_0)(S_3 + (1+a)S_1) + S_0(DS_3 + (1+a)DS_1)$$

$$) \Big\} (2(S_1+S_3)(S_2-(1+a)S_1)+1)(2ai\alpha((1-a)\tau_0^{11} - (1+a)\tau_0^{22}) - \frac{4ai\alpha(1-\nu)}{ReE}) - 4 \left\{ ((DS_1 + DS_3)(S_3 \right.$$

$$+ (1+a)S_1) + (S_1 + S_3)(DS_3 + (1+a)DS_1)) - ((DS_0(S_3 + (1+a)S_1) + S_0(DS_3 + (1+a)DS_1))(S_1$$

$$+ S_3)(S_3 + (1+a)S_1) \Big\} \left(2ai\alpha((1-a)\tau_0^{11} + (1+a)\tau_0^{22}) + \frac{4i\alpha(1-\nu)}{ReE} \right) \right], \quad (5.9b)$$

$$c_2 = \frac{-4(S_3 + (1+a)S_1)^2}{(4S_0^2 d_0^3 (S_3 + (1+a)S_1)^2)} \left[\left[S_0^2 \left\{ \tilde{A}d_0^2 + 2(D\tilde{B})d_0^2 + (D^2\tilde{C})d_0^2 - \tilde{C}d_0(D^2 d_0) - 2\tilde{B}d_0(Dd_0) - \right. \right. \right.$$

$$2(D\tilde{C})d_0(Dd_0) + 2\tilde{C}(Dd_0)^2 + \alpha^2\tilde{C}d_0^2 \Big\} + 2(1-a^2)(i\alpha) \left\{ S_0((D^2U)(S_1 + S_3) + DU(DS_1 + \right.$$

$$DS_3)) - DU(S_1 + S_3)DS_0 \Big\} \tilde{C}d_0^2 + 2i\alpha(1-a^2)DU(S_1+S_3)S_0 \left\{ (\tilde{B} + D\tilde{C})d_0^2 - \tilde{C}d_0(Dd_0) \right\} \Big]$$

$$+ d_0^3 [2S_0(S_3 + (1+a)S_1) \left\{ (2(S_1 + S_3)(S_2 - (1+a)S_1) + 1 - 2(S_3 + (1+a)S_1)(S_1 + S_3) \right.$$

$$2ai\alpha(1-a)(\tau_0^{11}) - (2(S_1 + S_3)(S_2 - (1+a)S_1) + 1 + 2(S_1 + S_3)(S_3 + (1+a)S_1))2a(i\alpha)$$

$$(1+a)\tau_0^{22} - \left\{ (2(S_1+S_3)(S_2-(1+a)S_1) + 1)a + 2(S_1 + S_3)(S_3 + (1+a)S_1)) \right\} \frac{4i\alpha(1-\nu)}{ReE} - 4(1-a^2)$$

$$(S_1 + S_3)(S_3 + (1+a)S_1)(D\tau_0^{12}) \Big\} - 8(S_3 + (1+a)S_1)^2(1-a^2)\tau_0^{12}(S_0(DS_1 + DS_3) - (DS_0)(S_1 +$$

$$S_3))]], \quad (5.9c)$$

$$c_3 = -\frac{1}{(S_0 d_0^2)} \left[S_0 \left\{ (\tilde{B})d_0 + 2(D\tilde{C})d_0 - 2(\tilde{C})(Dd_0) \right\} + 2(1-a^2)(i\alpha)(DU)(S_1 + S_3)(\tilde{C})d_0 + 2d_0^2 \right.$$

$$(S_1 + S_3)(1-a^2)(\tau_0^{12}) \right], \quad (5.9d)$$

$$c_4 = -\frac{(\tilde{C})}{(d_0)}. \quad (5.9e)$$

where the following coefficients are used in the definition of c_i's above,

$$\tilde{A} = \left(\frac{(1-a)}{2}(DU) + \varepsilon\tau_0^{12}\right)\left(-\frac{A}{H}\right) + \left(\varepsilon\tau_0^{12} - \frac{(1+a)}{2}(DU)\right)\left(F_1 + \frac{(A)(G)}{H}\right) - (i\alpha)(D\tau_0^{12}) + \frac{(1-a)}{2}$$

$$\alpha^2\tau_0^{22} - \frac{(1+a)}{2}\alpha^2\tau_0^{11} - \frac{\alpha^2(1-v)}{ReE},$$

$$\tilde{B} = \left(\frac{(1-a)}{2}(DU) + \varepsilon\tau_0^{12}\right)\left(-\frac{B}{H}\right) + \left(\varepsilon\tau_0^{12} - \frac{(1+a)}{2}(DU)\right)\left(F_2 + \frac{(B)(G)}{H}\right),$$

$$\tilde{C} = \left(\frac{(1-a)}{2}(DU) + \varepsilon\tau_0^{12}\right)\left(\frac{C}{H}\right) - \left(\varepsilon\tau_0^{12} - \frac{(1+a)}{2}(DU)\right)\left(\frac{(C)(G)}{H}\right) + \frac{(1-a)}{2}\tau_0^{11} - \frac{(1+a)}{2}\tau_0^{22}$$

$$- \frac{(1-v)}{ReE},$$

$$A = \frac{2(1-a^2)}{(\varepsilon\tau_0^{11}(1-a) + (i\alpha(U-c) + \frac{(1-v)}{ReE} + \varepsilon(\tau_0^{11} + 2\tau_0^{22}))(1+a))}\left[(i\alpha(D\tau_0^{22}) + (1+a)\alpha^2\tau_0^{12})\varepsilon\tau_0^{11} - \right.$$

$$(i\alpha(D\tau_0^{11}) - (1-a)\alpha^2\tau_0^{12})(i\alpha(U-c) + \frac{(1-v)}{ReE} + \varepsilon(\tau_0^{11} + 2\tau_0^{22}))\left.\right],$$

$$B = \frac{-4i\alpha(1-a^2)}{(\varepsilon\tau_0^{11}(1-a) + (i\alpha(U-c) + \frac{(1-v)}{ReE} + \varepsilon(\tau_0^{11} + 2\tau_0^{22}))(1+a))}\left[(\varepsilon\tau_0^{11})(a\tau_0^{22} + \frac{(1-v)}{ReE}) + (a\tau_0^{11} + \frac{(1-v)}{ReE})\right.$$

$$(i\alpha(U-c) + \frac{(1-v)}{ReE} + \varepsilon(\tau_0^{11} + 2\tau_0^{22}))\left.\right],$$

$$C = 2(1-a^2)\tau_0^{12},$$

$$H = \frac{2(1-a^2)}{(\varepsilon\tau_0^{11}(1-a) + (i\alpha(U-c) + \frac{(1-v)}{ReE} + \varepsilon(\tau_0^{11} + 2\tau_0^{22}))(1+a))}\left[(i\alpha(U-c) + \frac{(1-v)}{ReE})^2 + 6\varepsilon((i\alpha)\right.$$

$$(U-c) + \frac{(1-v)}{ReE})(\tau_0^{11} + 2\tau_0^{22}) + 2(\varepsilon)^2(\tau_0^{11} + \tau_0^{22})^2\left.\right],$$

$$F_1 = \frac{(i\alpha((1+a)(D\tau_0^{22}) + (1-a)(D\tau_0^{11})) + 4a\alpha^2\tau_0^{12})}{(\varepsilon\tau_0^{11}(1-a) + (i\alpha(U-c) + \frac{(1-v)}{ReE} + \varepsilon(\tau_0^{11} + 2\tau_0^{22}))(1+a))},$$

$$F_2 = \frac{(2ai\alpha((1-a)\tau_0^{11} - (1+a)\tau_0^{22} - \frac{2(1-v)}{ReE}))}{(\varepsilon\tau_0^{11}(1-a) + (i\alpha(U-c) + \frac{(1-v)}{ReE} + \varepsilon(\tau_0^{11} + 2\tau_0^{22}))(1+a))},$$

$$G = \frac{((i\alpha(U-c) + 2\varepsilon\tau_0^{11} + \frac{(1-v)}{ReE})(1-a) + 2\varepsilon\tau_0^{22})}{(\varepsilon\tau_0^{11}(1-a) + (i\alpha(U-c) + \frac{(1-v)}{ReE} + \varepsilon(\tau_0^{11} + 2\tau_0^{22}))(1+a))},$$

$$d_0 = \frac{2(1-a^2)(DU)}{H}\left[(\frac{1-a}{2})(DU) + \varepsilon\tau_0^{12}\right] + S_1 + \frac{2(1-a^2)(DU)(G)}{H}\left[(\frac{1+a}{2})(DU) - \varepsilon\tau_0^{12}\right],$$

$$S_1 = i\alpha(U-c) + \frac{(1-v)}{ReE} + \varepsilon(\tau_0^{11} + \tau_0^{22}),$$

$$S_2 = \varepsilon(1-a)\tau_0^{11} - \varepsilon(1+a)\tau_0^{22},$$

$$S_3 = \varepsilon(1-a)\tau_0^{11} + \varepsilon(1+a)\tau_0^{22},$$

$$S_0 = aS_1S_2 + S_1S_3 + (1-a^2)S_1^2. \tag{5.10a}$$

along with the first derivatives,

$$DÃ = ((\frac{1-a}{2})(D^2U) + \varepsilon(D\tau_0^{12}))(-\frac{A}{H}) + ((\frac{1-a}{2})(DU) + \varepsilon\tau_0^{12})(\frac{(DH)A - H(DA)}{H^2}) + (\varepsilon(D\tau_0^{12})$$
$$- (\frac{1+a}{2})(D^2U))(F_1 + \frac{AG}{H}) + (\varepsilon\tau_0^{12} - (\frac{1+a}{2})(DU))(DF_1 + \frac{HA(DG) + HG(DA) - AG(DH)}{H^2})$$
$$- i\alpha(D^2\tau_0^{12}) + (\frac{1-a}{2})\alpha^2(D\tau_0^{22}) - (\frac{1+a}{2})\alpha^2(D\tau_0^{11}), \tag{5.11a}$$

$$D\tilde{B} = ((\frac{1-a}{2})(D^2U) + \varepsilon(D\tau_0^{12}))(-\frac{B}{H}) + ((\frac{1-a}{2})(DU) + \varepsilon\tau_0^{12})(\frac{(DH)B - H(DB)}{H^2}) + (\varepsilon(D\tau_0^{12})$$
$$- (\frac{1+a}{2})(D^2U))(F_2 + \frac{BG}{H}) + (\varepsilon\tau_0^{12} - (\frac{1+a}{2})(DU))(DF_2 + \frac{HB(DG) + HG(DB) - BG(DH)}{H^2}), \tag{5.11b}$$

$$D\tilde{C} = ((\frac{1-a}{2})(D^2U) + \varepsilon(D\tau_0^{12}))(\frac{C}{H}) + ((\frac{1-a}{2})(DU) + \varepsilon\tau_0^{12})(\frac{(DC)H - C(DH)}{H^2}) - (\varepsilon(D\tau_0^{12})$$
$$- (\frac{1+a}{2})(D^2U))(\frac{CG}{H}) - (\varepsilon\tau_0^{12} - (\frac{1+a}{2})(DU))(\frac{HC(DG) + HG(DC) - CG(DH)}{H^2}) + (\frac{1-a}{2})$$
$$(D\tau_0^{11}) - (\frac{1+a}{2})(D\tau_0^{22}), \tag{5.11c}$$

$$DA = \frac{2(1-a^2)}{(\varepsilon\tau_0^{11}(1-a) + (i\alpha(U-c) + \frac{(1-\nu)}{ReE} + \varepsilon(\tau_0^{11} + 2\tau_0^{22}))(1+a))^2}\Big[(\varepsilon\tau_0^{11}(1-a) + (i\alpha(U-c)+$$
$$\frac{(1-\nu)}{ReE} + \varepsilon(\tau_0^{11} + 2\tau_0^{22}))(1+a))\Big\{(i\alpha D^2\tau_0^{22} + (1+a)\alpha^2 D\tau_0^{12})(\varepsilon\tau_0^{11}) + (i\alpha D\tau_0^{22} + (1+a)\alpha^2\tau_0^{12})$$
$$(\varepsilon D\tau_0^{11}) - (i\alpha D^2\tau_0^{11} - (1-a)\alpha^2 D\tau_0^{12})(i\alpha(U-c) + \frac{(1-\nu)}{ReE} + \varepsilon(\tau_0^{11} + 2\tau_0^{22})) - (i\alpha D\tau_0^{11} - (1-a)$$
$$\alpha^2\tau_0^{12})(i\alpha(DU) + \varepsilon(D\tau_0^{11} + 2D\tau_0^{22})\Big\} - \Big\{(i\alpha D\tau_0^{22} + (1+a)\alpha^2\tau_0^{12})(\varepsilon\tau_0^{11}) - (i\alpha D\tau_0^{11} - (1-a)$$
$$\alpha^2\tau_0^{12})(i\alpha(U-c) + \frac{(1-\nu)}{ReE} + \varepsilon(\tau_0^{11} + 2\tau_0^{22}))\Big\}(2\varepsilon D\tau_0^{11} + (1+a)(i\alpha(DU) + 2\varepsilon D\tau_0^{22}))\Big], \tag{5.11d}$$

$$DB = \frac{-4i\alpha(1-a^2)}{(\varepsilon\tau_0^{11}(1-a) + (i\alpha(U-c) + \frac{(1-\nu)}{ReE} + \varepsilon(\tau_0^{11} + 2\tau_0^{22}))(1+a))^2}\Big[(\varepsilon\tau_0^{11}(1-a) + (i\alpha(U-c)+$$
$$\frac{(1-\nu)}{ReE} + \varepsilon(\tau_0^{11} + 2\tau_0^{22}))(1+a))\Big\{\varepsilon D\tau_0^{11}(a\tau_0^{22} + \frac{(1-\nu)}{ReE}) + a\varepsilon\tau_0^{11}D\tau_0^{22} + (aD\tau_0^{11})(i\alpha(U-c) + \frac{(1-\nu)}{ReE}$$
$$+ \varepsilon(\tau_0^{11} + 2\tau_0^{22})) + (a\tau_0^{11} + \frac{(1-\nu)}{ReE})(i\alpha(DU) + \varepsilon(D\tau_0^{11} + 2D\tau_0^{22}))\Big\} - (2\varepsilon D\tau_0^{11} + (i\alpha(DU) + 2\varepsilon$$
$$D\tau_0^{22})(1+a))\Big\{\varepsilon\tau_0^{11}(a\tau_0^{22} + \frac{(1-\nu)}{ReE}) + (a\tau_0^{11} + \frac{(1-\nu)}{ReE})(i\alpha(U-c) + \frac{(1-\nu)}{ReE} + \varepsilon(\tau_0^{11} + 2\tau_0^{22}))\Big\}\Big], \tag{5.11e}$$

$$DC = 2(1-a^2)(D\tau_0^{12}),\tag{5.11f}$$

$$DH = \frac{2(1-a^2)}{(\varepsilon\tau_0^{11}(1-a)+(i\alpha(U-c)+\frac{(1-\nu)}{ReE}+\varepsilon(\tau_0^{11}+2\tau_0^{22}))(1+a))^2}\Big[(\varepsilon\tau_0^{11}(1-a)+(i\alpha(U-c)+$$

$$\frac{(1-\nu)}{ReE}+\varepsilon(\tau_0^{11}+2\tau_0^{22}))(1+a))\Big\{2i\alpha(DU)(i\alpha(U-c)+\frac{(1-\nu)}{ReE})+6\varepsilon i\alpha(DU)(\tau_0^{11}+\tau_0^{22})+6\varepsilon(i$$

$$(U-c)+\frac{(1-\nu)}{ReE})(D\tau_0^{11}+D\tau_0^{22})+(4\varepsilon^2)(\tau_0^{11}+\tau_0^{22})(D\tau_0^{11}+D\tau_0^{22})\Big\}-(2\varepsilon(D\tau_0^{11})+(i\alpha(DU)+$$

$$2\varepsilon(D\tau_0^{22})(1+a))\Big\{(i\alpha(U-c)+\frac{(1-\nu)}{ReE})^2+6\varepsilon(i\alpha(U-c)+\frac{(1-\nu)}{ReE})(\tau_0^{11}+\tau_0^{22})+2\varepsilon^2(\tau_0^{11}+\tau_0^{22})^2\Big\}$$

$$\tag{5.11g}$$

$$DF_1 = \frac{1}{(\varepsilon\tau_0^{11}(1-a)+(i\alpha(U-c)+\frac{(1-\nu)}{ReE}+\varepsilon(\tau_0^{11}+2\tau_0^{22}))(1+a))^2}\Big[(\varepsilon\tau_0^{11}(1-a)+(i\alpha(U-c)+$$

$$\frac{(1-\nu)}{ReE}+\varepsilon(\tau_0^{11}+2\tau_0^{22}))(1+a))(i\alpha((1+a)D^2\tau_0^{22}+(1-a)D^2\tau_0^{11})+4a\alpha^2(D\tau_0^{12}))-(2\varepsilon(D\tau_0^{11})$$

$$+(i\alpha(DU)+2\varepsilon(D\tau_0^{22})(1+a))(i\alpha((1+a)D\tau_0^{22}+(1-a)D\tau_0^{11})+4a\alpha^2\tau_0^{12})\Big],$$

$$\tag{5.11h}$$

$$DF_2 = \frac{2ai\alpha}{(\varepsilon\tau_0^{11}(1-a)+(i\alpha(U-c)+\frac{(1-\nu)}{ReE}+\varepsilon(\tau_0^{11}+2\tau_0^{22}))(1+a))^2}\Big[(\varepsilon\tau_0^{11}(1-a)+(i\alpha(U-c)+$$

$$\frac{(1-\nu)}{ReE}+\varepsilon(\tau_0^{11}+2\tau_0^{22}))(1+a))((1-a)(D\tau_0^{11})-(1+a)(D\tau_0^{22}))-(2\varepsilon(D\tau_0^{11})+(i\alpha(DU)+2\varepsilon$$

$$(D\tau_0^{22}))(1+a))((1-a)\tau_0^{11}-(1+a)\tau_0^{22}-\frac{2(1-\nu)}{ReE})\Big],$$

$$DG = \frac{1}{(\varepsilon\tau_0^{11}(1-a)+(i\alpha(U-c)+\frac{(1-\nu)}{ReE}+\varepsilon(\tau_0^{11}+2\tau_0^{22}))(1+a))^2}\Big[(\varepsilon\tau_0^{11}(1-a)+(i\alpha(U-c)+$$

$$\frac{(1-\nu)}{ReE}+\varepsilon(\tau_0^{11}+2\tau_0^{22}))(1+a))((i\alpha(DU)+2\varepsilon(D\tau_0^{11}))(1-a)+2\varepsilon(D\tau_0^{22}))-((i\alpha(DU)+2\varepsilon$$

$$(D\tau_0^{22}))(1+a)+2\varepsilon(D\tau_0^{11}))((i\alpha(U-c)+\frac{(1-\nu)}{ReE}+2\varepsilon\tau_0^{11})(1-a)+2\varepsilon\tau_0^{22})\Big],$$

$$\tag{5.11i}$$

$$Dd_0 = DS_1 + 2(1-a^2)\Big[((\frac{1-a}{2})(D^2U)+\varepsilon(D\tau_0^{12}))(\frac{(DU)}{H})+((\frac{1-a}{2})(DU)+\varepsilon(\tau_0^{12}))$$

$$(\frac{(H(D^2U)-(DU)(DH))}{H^2})-((\varepsilon D\tau_0^{12}-(\frac{1+a}{2})(D^2U))(\frac{(DU)G}{H})+(\varepsilon\tau_0^{12}-(\frac{1+a}{2})(DU))$$

$$\frac{H(D^2U)G+H(DU)(DG)-(DH)(DU)G}{H^2})\Big],\tag{5.11j}$$

$$DS_1 = i\alpha(DU) + \varepsilon(D\tau_0^{11} + D\tau_0^{22}), \tag{5.11k}$$

$$DS_2 = \varepsilon(1-a)D\tau_0^{11} - \varepsilon(1+a)D\tau_0^{22}, \tag{5.11l}$$

$$DS_3 = \varepsilon(1-a)D\tau_0^{11} + \varepsilon(1+a)D\tau_0^{22}, \tag{5.11m}$$

and the first derivatives,

$$D^2\tilde{A} = ((\frac{1-a}{2})(D^3U) + \varepsilon(D^2\tau_0^{12}))(-\frac{A}{H}) + 2((\frac{1-a}{2})(D^2U) + \varepsilon(D\tau_0^{12}))(\frac{(DH)A - H(DA)}{H^2}) + ((\frac{1-a}{2})$$
$$(DU) + \varepsilon\tau_0^{12})\frac{H((D^2H)A - H(D^2A)) - 2(DH)((DH)A - H(DA))}{H^3} + (\varepsilon D^2\tau_0^{12} - (\frac{1+a}{2})(D^3U))(F_1 +$$
$$\frac{AG}{H}) + 2(\varepsilon D\tau_0^{12} - (\frac{1+a}{2})(D^2U))(DF_1 + \frac{HA(DG) + HG(DA) - AG(DH)}{H^2}) + (\varepsilon\tau_0^{12} - (\frac{1+a}{2})(DU))$$
$$(D^2F_1 + \frac{1}{H^3}(H^2(A(D^2G) + 2(DG)(DH) + G(D^2A)) - AGH(D^2H)) - 2(DH)(H(A(DG) + G(DA)) -$$
$$AG(DH))) - i\alpha D^3\tau_0^{12} + (\frac{1-a}{2})\alpha^2 D^2\tau_0^{22} - (\frac{1+a}{2})\alpha^2 D^2\tau_0^{11}, \tag{5.12a}$$

$$D^2\tilde{B} = ((\frac{1-a}{2})(D^3U) + \varepsilon(D^2\tau_0^{12}))(-\frac{B}{H}) + 2((\frac{1-a}{2})(D^2U) + \varepsilon D\tau_0^{12})(\frac{(DH)B - H(DB)}{H^2})$$
$$+ ((\frac{1-a}{2})(DU) + \varepsilon\tau_0^{12})(\frac{H(D^2H)B - H^2(D^2B) - 2(DH)(B(DH) - H(DB))}{H^3}) + (\varepsilon(D^2\tau_0^{12})$$
$$- (\frac{1+a}{2})(D^3U))(F_2 + \frac{BG}{H}) + 2(\varepsilon D\tau_0^{12} - (\frac{1+a}{2})(D^2U))(DF_2 + \frac{HB(DG) + HG(DB) - BG(DH)}{H^2})$$
$$+ (\varepsilon\tau_0^{12} - (\frac{1+a}{2})(DU))(D^2F_2 + \frac{1}{H^3}(H^2B(D^2G) + 2H^2(DG)(DB) + H^2G(D^2B) - BGH(D^2H)$$
$$- 2(DH)(HB(DG) + HG(DB) - BG(DH)))), \tag{5.12b}$$

$$D^2\tilde{C} = ((\frac{1-a}{2})(D^3U) + \varepsilon(D^2\tau_0^{12}))(\frac{C}{H}) + 2((\frac{1-a}{2})(D^2U) + \varepsilon(D\tau_0^{12}))(\frac{(DC)H - C(DH)}{H^2}) + ((\frac{1-a}{2})$$
$$(DU) + \varepsilon\tau_0^{12})\frac{H^2(D^2C) - CH(D^2H) - 2(DH)((DC)H - C(DH))}{H^3} - (\varepsilon D^2\tau_0^{12} - (\frac{1+a}{2})(D^3U))(\frac{CG}{H})$$
$$- 2(\varepsilon D\tau_0^{12} - (\frac{1+a}{2})D^2U)(\frac{HC(DG) + HG(DC) - CG(DH)}{H^2}) - (\varepsilon\tau_0^{12} - DU(\frac{1+a}{2}))$$
$$(\frac{H^2(C(D^2G) + 2(DG)(DC) + G(D^2C)) - CGH(D^2H) - 2(DH)(HC(DG) + HG(DC) - CG(DH))}{H^3})$$
$$+ (\frac{1-a}{2})D^2\tau_0^{11} - (\frac{1+a}{2})D^2\tau_0^{22}, \tag{5.12c}$$

$$D^2 G = \frac{1}{(\varepsilon \tau_0^{11}(1-a) + (i\alpha(U-c) + \frac{(1-\nu)}{ReE} + \varepsilon(\tau_0^{11} + 2\tau_0^{22}))(1+a))^3} \left[(\varepsilon \tau_0^{11}(1-a) + (i\alpha(U-c) + \right.$$

$$\frac{(1-\nu)}{ReE} + \varepsilon(\tau_0^{11} + 2\tau_0^{22}))(1+a)) \left\{ (\varepsilon \tau_0^{11}(1-a) + (i\alpha(U-c) + \frac{(1-\nu)}{ReE} + \varepsilon(\tau_0^{11} + 2\tau_0^{22}))(1+a)) \right.$$

$$((i\alpha(D^2 U) + 2\varepsilon D^2 \tau_0^{11})(1-a) + 2\varepsilon D^2 \tau_0^{22}) - (2\varepsilon D^2 \tau_0^{11} + (i\alpha(D^2 U) + 2\varepsilon D^2 \tau_0^{22})(1+a))$$

$$\left. ((i\alpha(U-c) + \frac{(1-\nu)}{ReE} + 2\varepsilon \tau_0^{11})(1-a) + 2\varepsilon \tau_0^{22}) \right\} - 2(2\varepsilon D \tau_0^{11} + (i\alpha(DU) + 2\varepsilon D \tau_0^{22})(1+a))$$

$$\left\{ (\varepsilon \tau_0^{11}(1-a) + (i\alpha(U-c) + \frac{(1-\nu)}{ReE} + \varepsilon(\tau_0^{11} + 2\tau_0^{22}))(1+a))(2\varepsilon D \tau_0^{22} + (i\alpha(DU) + 2\varepsilon D \tau_0^{11}) \right.$$

$$(1-a)) - (2\varepsilon D \tau_0^{11} + (i\alpha(DU) + 2\varepsilon D \tau_0^{22})(1+a))((i\alpha(U-c) + \frac{(1-\nu)}{ReE} + 2\varepsilon \tau_0^{11})(1-a) + 2\varepsilon \tau_0^2$$

$$(5.12\text{d})$$

$$D^2 F_1 = \frac{1}{(\varepsilon \tau_0^{11}(1-a) + (i\alpha(U-c) + \frac{(1-\nu)}{ReE} + \varepsilon(\tau_0^{11} + 2\tau_0^{22}))(1+a))^3} \left[(\varepsilon \tau_0^{11}(1-a) + (i\alpha(U-c) + \right.$$

$$\frac{(1-\nu)}{ReE} + \varepsilon(\tau_0^{11} + 2\tau_0^{22}))(1+a)) \left\{ (\varepsilon \tau_0^{11}(1-a) + (i\alpha(U-c) + \frac{(1-\nu)}{ReE} + \varepsilon(\tau_0^{11} + 2\tau_0^{22}))(1+a)) \right.$$

$$(i\alpha((1+a)D^3 \tau_0^{22} + (1-a)D^3 \tau_0^{11}) + 4a\alpha^2 D^2 \tau_0^{12}) - (2\varepsilon D^2 \tau_0^{11} + (i\alpha(D^2 U) + 2\varepsilon D^2 \tau_0^{22})(1+a))$$

$$\left. (i\alpha((1+a)D \tau_0^{22} + (1-a)D \tau_0^{11}) + 4a\alpha^2 D \tau_0^{12}) \right\} - 2(2\varepsilon D \tau_0^{11} + (i\alpha(DU) + 2\varepsilon D \tau_0^{22})(1+a)) \left\{ (\varepsilon \right.$$

$$\tau_0^{11}(1-a) + (i\alpha(U-c) + \frac{(1-\nu)}{ReE} + \varepsilon(\tau_0^{11} + 2\tau_0^{22}))(1+a))(i\alpha((1+a)D^2 \tau_0^{22} + (1-a)D^2 \tau_0^{11}) +$$

$$\alpha^2 D \tau_0^{12}) - (2\varepsilon D \tau_0^{11} + (i\alpha(DU) + 2\varepsilon D \tau_0^{22})(1+a))(i\alpha((1+a)D \tau_0^{22} + (1-a)D \tau_0^{11}) + 4a\alpha^2 \tau_0^{12})$$

$$(5.12\text{e})$$

$$D^2 C = 2(1-a^2)D^2 \tau_0^{12}, \qquad\qquad (5.12\text{f})$$

$$
D^2 A = \frac{2(1-a^2)}{(\varepsilon\tau_0^{11}(1-a)+(i\alpha(U-c)+\frac{(1-\nu)}{ReE}+\varepsilon(\tau_0^{11}+2\tau_0^{22}))(1+a))^3}\left[(\varepsilon\tau_0^{11}(1-a)+(i\alpha(U-c)+\frac{(1-\nu)}{ReE}\right.
$$

$$
+\varepsilon(\tau_0^{11}+2\tau_0^{22}))(1+a))\left\{(2\varepsilon D\tau_0^{11}+(i\alpha(DU)+2\varepsilon(D\tau_0^{22}))(1+a))((i\alpha D^2\tau_0^{22}+(1+a)\alpha^2 D\tau_0^{12})\right.
$$

$$
(\varepsilon\tau_0^{11})+(i\alpha D\tau_0^{22}+(1+a)\alpha^2\tau_0^{12})(\varepsilon D\tau_0^{11})-(i\alpha D^2\tau_0^{11}-(1-a)\alpha^2 D\tau_0^{12})(i\alpha(U-c)+\frac{(1-\nu)}{ReE}+\varepsilon
$$

$$
(\tau_0^{11}+2\tau_0^{22}))-(i\alpha D\tau_0^{11}-(1-a)\alpha^2\tau_0^{12})(i\alpha(DU)+\varepsilon(D\tau_0^{11}+2D\tau_0^{22})))+(\varepsilon\tau_0^{11}(1-a)+(i\alpha(U
$$

$$
-c)+\frac{(1-\nu)}{ReE}+\varepsilon(\tau_0^{11}+2\tau_0^{22}))(1+a))((i\alpha D^3\tau_0^{22}+(1+a)\alpha^2 D^2\tau_0^{12})(\varepsilon\tau_0^{11})+2(i\alpha D^2\tau_0^{22}+(1+a)\alpha^2
$$

$$
D\tau_0^{12})(\varepsilon D\tau_0^{11})+(i\alpha D\tau_0^{22}+(1+a)\alpha^2\tau_0^{12})(\varepsilon D^2\tau_0^{11})-(i\alpha D^3\tau_0^{11}-(1-a)\alpha^2 D^2\tau_0^{12})(i\alpha(U-c)+
$$

$$
\frac{(1-\nu)}{ReE}+\varepsilon(\tau_0^{11}+2\tau_0^{22}))-2(i\alpha D^2\tau_0^{11}-(1-a)\alpha^2 D\tau_0^{12})(i\alpha(DU)+\varepsilon(D\tau_0^{11}+2D\tau_0^{22}))-(i\alpha D\tau_0^{11}-
$$

$$
(1-a)\alpha^2\tau_0^{12})(i\alpha(D^2 U)+\varepsilon(D^2\tau_0^{11}+2D^2\tau_0^{22}))-((i\alpha D^2\tau_0^{22}+(1+a)\alpha^2 D\tau_0^{12})(\varepsilon\tau_0^{11})+(i\alpha D\tau_0^{22}
$$

$$
+(1+a)\alpha^2\tau_0^{12})(\varepsilon D\tau_0^{11})-(i\alpha D^2\tau_0^{11}-(1-a)\alpha^2 D\tau_0^{12})(i\alpha(U-c)+\frac{(1-\nu)}{ReE}+\varepsilon(\tau_0^{11}+2\tau_0^{22}))-(i\alpha
$$

$$
D\tau_0^{11}-(1-a)\alpha^2\tau_0^{12})(i\alpha(DU)+\varepsilon(D\tau_0^{11}+2D\tau_0^{22})))(2\varepsilon D\tau_0^{11}+(1+a)(i\alpha(DU)+2\varepsilon D\tau_0^{22}))-
$$

$$
((i\alpha D\tau_0^{22}+(1+a)\alpha^2\tau_0^{12})(\varepsilon\tau_0^{11})-(i\alpha D\tau_0^{11}-(1-a)\alpha^2\tau_0^{12})(i\alpha(U-c)+\frac{(1-\nu)}{ReE}+\varepsilon(\tau_0^{11}+2\tau_0^{22})))
$$

$$
(2\varepsilon D^2\tau_0^{11}+(1+a)(i\alpha(D^2 U)+2\varepsilon D^2\tau_0^{22}))\}-2(2\varepsilon D\tau_0^{11}+(i\alpha(DU)+2\varepsilon D\tau_0^{22})(1+a))\{((i\alpha
$$

$$
D^2\tau_0^{22}+(1+a)\alpha^2 D\tau_0^{12})(\varepsilon\tau_0^{11})+(i\alpha D\tau_0^{22}+(1+a)\alpha^2\tau_0^{12})(\varepsilon D\tau_0^{11})-(i\alpha D^2\tau_0^{11}-(1-a)\alpha^2 D\tau_0^{12})
$$

$$
(i\alpha(U-c)+\frac{(1-\nu)}{ReE}+\varepsilon(\tau_0^{11}+2\tau_0^{22}))-(i\alpha D\tau_0^{11}-(1-a)\alpha^2\tau_0^{12})(i\alpha(DU)+\varepsilon(D\tau_0^{11}+2D\tau_0^{22})))(\varepsilon\tau_0^{11}
$$

$$
(1-a)+(i\alpha(U-c)+\frac{(1-\nu)}{ReE}+\varepsilon(\tau_0^{11}+2\tau_0^{22}))(1+a))-((i\alpha D\tau_0^{22}+(1+a)\alpha^2\tau_0^{12})(\varepsilon\tau_0^{11})-(i\alpha D\tau_0^{11}
$$

$$
\left.\left.-(1-a)\alpha^2\tau_0^{12})(i\alpha(U-c)+\frac{(1-\nu)}{ReE}+\varepsilon(\tau_0^{11}+2\tau_0^{22})))(2\varepsilon D\tau_0^{11}+(1+a)(i\alpha(DU)+2\varepsilon D\tau_0^{22}))\right\}\right],
$$

$$
(5.12g)
$$

$$D^2H = \frac{2(1-a^2)}{(\varepsilon\tau_0^{11}(1-a) + (i\alpha(U-c) + \frac{(1-\nu)}{ReE} + \varepsilon(\tau_0^{11} + 2\tau_0^{22}))(1+a))^3}\Bigg[(\varepsilon\tau_0^{11}(1-a) + (i\alpha(U-c) + \frac{(1}{}$$

$$+ \varepsilon(\tau_0^{11} + 2\tau_0^{22}))(1+a))\bigg\{(\varepsilon\tau_0^{11}(1-a) + (i\alpha(U-c) + \frac{(1-\nu)}{ReE} + \varepsilon(\tau_0^{11} + 2\tau_0^{22}))(1+a))(2(i\alpha(U-c))$$

$$+ \frac{(1-\nu)}{ReE})i\alpha(D^2U) - 2\alpha^2(DU)^2 + 6\varepsilon i\alpha(D^2U)(\tau_0^{11} + \tau_0^{22}) + 12\varepsilon i\alpha(DU)(D\tau_0^{11} + D\tau_0^{22}) + 6\varepsilon(i\alpha(U)$$

$$+ \frac{(1-\nu)}{ReE})(D^2\tau_0^{11} + D^2\tau_0^{22}) + 4\varepsilon^2(D\tau_0^{11} + D\tau_0^{22})^2 + 4\varepsilon^2(\tau_0^{11} + \tau_0^{22})(D^2\tau_0^{11} + D^2\tau_0^{22})\bigg\} - (2\varepsilon(D^2\tau_0^{11} + D^2$$

$$+ i\alpha(D^2U)(1+a))((i\alpha(U-c) + \frac{(1-\nu)}{ReE})^2 + 6\varepsilon(i\alpha(U-c) + \frac{(1-\nu)}{ReE})(\tau_0^{11} + \tau_0^{22}) + 2\varepsilon^2(\tau_0^{11} + \tau_0^{22})^2$$

$$(D\tau_0^{11} + D\tau_0^{22}) + i\alpha DU)(1+a))\bigg\{(\varepsilon\tau_0^{11}(1-a) + (i\alpha(U-c) + \frac{(1-\nu)}{ReE} + \varepsilon(\tau_0^{11} + 2\tau_0^{22}))(1+a))(2(i\alpha)$$

$$(i\alpha(U-c) + \frac{(1-\nu)}{ReE}) + 6\varepsilon i\alpha DU(\tau_0^{11} + \tau_0^{22}) + 6\varepsilon(i\alpha(U-c) + \frac{(1-\nu)}{ReE})(D\tau_0^{11} + D\tau_0^{22}) + 4\varepsilon^2(\tau_0^{1}$$

$$(D\tau_0^{11} + D\tau_0^{22})\bigg\} - (2\varepsilon D\tau_0^{11} + (i\alpha(DU) + 2\varepsilon D\tau_0^{22})(1+a))((i\alpha(U-c) + \frac{(1-\nu)}{ReE})^2 + 6\varepsilon(i\alpha(U-c) +$$

$$(\tau_0^{11} + \tau_0^{22}) + 2\varepsilon^2(\tau_0^{11} + \tau_0^{22})^2)\bigg\}\Bigg], \tag{5.12h}$$

$$D^2F_2 = \frac{2ai\alpha}{(\varepsilon\tau_0^{11}(1-a) + (i\alpha(U-c) + \frac{(1-\nu)}{ReE} + \varepsilon(\tau_0^{11} + 2\tau_0^{22}))(1+a))^3}\Bigg[(\varepsilon\tau_0^{11}(1-a) + (i\alpha(U-c) + \frac{(1}{}$$

$$+ \varepsilon(\tau_0^{11} + 2\tau_0^{22}))(1+a))((\varepsilon\tau_0^{11}(1-a) + (i\alpha(U-c) + \frac{(1-\nu)}{ReE} + \varepsilon(\tau_0^{11} + 2\tau_0^{22}))(1+a))((1-a)(D^2$$

$$- (1+a)(D^2\tau_0^{22})) - (2\varepsilon(D^2\tau_0^{11}) + (i\alpha(D^2U) + 2\varepsilon(D^2\tau_0^{22}))(1+a))((1-a)\tau_0^{11} - (1+a)\tau_0^{22} - \frac{2(1}{Re}$$

$$- 2(2\varepsilon D\tau_0^{11} + (i\alpha DU + 2\varepsilon D\tau_0^{22})(1+a))((\varepsilon\tau_0^{11}(1-a) + (i\alpha(U-c) + \frac{(1-\nu)}{ReE} + \varepsilon(\tau_0^{11} + 2\tau_0^{22}))(1$$

$$((1-a)D\tau_0^{11} - (1+a)D\tau_0^{22}) - (2\varepsilon D\tau_0^{11} + (i\alpha DU + 2\varepsilon D\tau_0^{22})(1+a))((1-a)\tau_0^{11} - (1+a)\tau_0^{22} - \frac{2(1-}{Re}$$

$$\tag{5.12i}$$

$$D^2d_0 = D^2S_1 + 2(1-a^2)\Bigg[((\frac{1-a}{2})(D^3U) + \varepsilon(D^2\tau_0^{12}))(\frac{(DU)}{H}) + 2((\frac{1-a}{2})(D^2U) + \varepsilon(D\tau_0^{12}))$$

$$(\frac{(H(D^2U) - (DU)(DH))}{H^2}) + (\frac{H(H(D^3U) - (DU)(D^2H)) - 2(DH)(H(D^2U) - (DH)(DU))}{H^3})$$

$$((\frac{1-a}{2})(DU) + \varepsilon\tau_0^{12}) - \bigg\{((\varepsilon D^2\tau_0^{12} - (\frac{1+a}{2})(D^3U))(\frac{(DU)G}{H}) + 2(\varepsilon D\tau_0^{12} - (\frac{1+a}{2})(D^2U))$$

$$(\frac{H(D^2U)G + H(DU)(DG) - (DH)(DU)G}{H^2}) + (\varepsilon\tau_0^{12} - (\frac{1+a}{2})(DU))\frac{1}{H^3}(H(H(D^3U)G + 2H(D^2$$

$$(DG) + H(DU(D^2G) - G(DU)(D^2H) - 2(DH)(H(D^2U)G + H(DU)(DG) - (DU)(DH)G)))\bigg\}\Bigg]$$

$$\tag{5.12j}$$

$$D^2B = \frac{-4i\alpha(1-a^2)}{(\varepsilon\tau_0^{11}(1-a) + (i\alpha(U-c) + \frac{(1-v)}{ReE} + \varepsilon(\tau_0^{11} + 2\tau_0^{22}))(1+a))^3} \Big[(\varepsilon\tau_0^{11}(1-a) + (i\alpha(U-c)+$$

$$\frac{(1-v)}{ReE} + \varepsilon(\tau_0^{11} + 2\tau_0^{22}))(1+a))((2\varepsilon D\tau_0^{11} + (i\alpha(DU) + 2D\tau_0^{22})(1+a))(\varepsilon D\tau_0^{11}(a\tau_0^{22} + \frac{(1-v)}{ReE}) +$$

$$a\varepsilon\tau_0^{11}D\tau_0^{22} + aD\tau_0^{11}(i\alpha(U-c) + \frac{(1-v)}{ReE} + \varepsilon(\tau_0^{11} + 2\tau_0^{22})) + (a\tau_0^{11} + \frac{(1-v)}{ReE})(i\alpha(DU) + \varepsilon(D\tau_0^{11}$$

$$+ 2D\tau_0^{22})) + (\varepsilon\tau_0^{11}(1-a) + (i\alpha(U-c) + \frac{(1-v)}{ReE} + \varepsilon(\tau_0^{11} + 2\tau_0^{22}))(1+a))(\varepsilon(D^2\tau_0^{11})(a\tau_0^{22} + \frac{(1-v)}{ReE})$$

$$+ 2a\varepsilon(D\tau_0^{11})(D\tau_0^{22}) + a\varepsilon\tau_0^{11}(D^2\tau_0^{22}) + (aD^2\tau_0^{11})(i\alpha(U-c) + \frac{(1-v)}{ReE} + \varepsilon(\tau_0^{11} + 2\tau_0^{22})) + 2aD\tau_0^{11}$$

$$(i\alpha(DU) + \varepsilon(D\tau_0^{11} + 2D\tau_0^{22})) + (a\tau_0^{11} + \frac{(1-v)}{ReE})(i\alpha(D^2U) + \varepsilon(D^2\tau_0^{11} + 2D^2\tau_0^{22})) - (2\varepsilon D^2\tau_0^{11} +$$

$$(i\alpha(D^2U) + 2\varepsilon D^2\tau_0^{22})(1+a))(\varepsilon\tau_0^{11})(a\tau_0^{22} + \frac{(1-v)}{ReE}) + (a\tau_0^{11} + \frac{(1-v)}{ReE})(i\alpha(U-c) + \frac{(1-v)}{ReE} + \varepsilon(\tau_0^{11}$$

$$+ 2\tau_0^{22}))) - (2\varepsilon D\tau_0^{11} + (i\alpha(DU) + 2\varepsilon D\tau_0^{22})(1+a))(\varepsilon D\tau_0^{11})(a\tau_0^{22} + \frac{(1-v)}{ReE}) + a\varepsilon\tau_0^{11}D\tau_0^{22} +$$

$$aD\tau_0^{11}(i\alpha(U-c) + \frac{(1-v)}{ReE} + \varepsilon(\tau_0^{11} + 2\tau_0^{22})) + (a\tau_0^{11} + \frac{(1-v)}{ReE})(i\alpha(DU) + \varepsilon(D\tau_0^{11} + 2D\tau_0^{22})))) -$$

$$2(2\varepsilon D\tau_0^{11} + (i\alpha(DU) + 2\varepsilon D\tau_0^{22})(1+a))(\varepsilon D\tau_0^{11}(a\tau_0^{22} + \frac{(1-v)}{ReE}) + a\varepsilon\tau_0^{11}D\tau_0^{22} + aD\tau_0^{11}(i\alpha(U-c)$$

$$+ \frac{(1-v)}{ReE} + \varepsilon(\tau_0^{11} + 2\tau_0^{22})) + (a\tau_0^{11} + \frac{(1-v)}{ReE})(i\alpha(DU) + \varepsilon(D\tau_0^{11} + 2D\tau_0^{22})) - (2\varepsilon D\tau_0^{11} + (i\alpha DU$$

$$+ 2\varepsilon D\tau_0^{22})(1+a))(\varepsilon\tau_0^{11}(a\tau_0^{22} + \frac{(1-v)}{ReE}) + (a\tau_0^{11} + \frac{(1-v)}{ReE})(i\alpha(U-c) + \frac{(1-v)}{ReE} + \varepsilon(\tau_0^{11} + 2\tau_0^{22}))))$$

$$(5.12\text{k})$$

The components of the base state extra elastic stress tensor, τ_0, is given by

$$\tau_0^{11} = \frac{1}{24\varepsilon^2 a^2 (\frac{ReE}{(1-v)})^4 M_1^{\frac{1}{3}}} \Big[2(2)^{\frac{1}{3}}\varepsilon^2 (\frac{ReE}{(1-v)})^6 (1+a)^4 - 4(2)^{\frac{1}{3}}\varepsilon^2 (\frac{ReE}{(1-v)})^6 (1+a)^2 (1-a^2) + 2(2)^{\frac{1}{3}}\varepsilon^2$$

$$(\frac{ReE}{(1-v)})^6 (1-a^2)^2 - 6(2)^{\frac{1}{3}}\varepsilon^2 (\frac{ReE}{(1-v)})^8 (1+a)^4 (1-a^2)U^2 + 12(2)^{\frac{1}{3}}\varepsilon^2 (\frac{ReE}{(1-v)})^8 (1+a)^2 (1-a^2)^2$$

$$U^2 - 6(2)^{\frac{1}{3}}\varepsilon^2 (\frac{ReE}{(1-v)})^8 (1-a^2)^3 U^2 - 8a\varepsilon(1+a)(\frac{ReE}{(1-v)})^3 M_1^{\frac{1}{3}} + (2M_1)^{\frac{2}{3}} \Big],$$

$$\tau_0^{22} = -\frac{(1-a)}{(1+a)}\tau_0^{11},$$

$$\tau_0^{12} = \frac{DU(1 - (1-a)\tau_0^{11}(\frac{ReE}{(1-v)}))}{(1 + \varepsilon(\frac{ReE}{(1-v)})(\tau_0^{11} + \tau_0^{22}))}, \qquad (5.13)$$

where the coefficient M_1 in the base stress, is given by

$$M_1 = 16\varepsilon^3 (\frac{ReE}{(1-v)})^9 a^3 (1+a)^3 \Big[(27a\varepsilon + 9(1-a^2))(\frac{ReE}{(1-v)})^2 U^2 + 1 + 3(3)^{\frac{1}{2}} (\frac{ReE}{(1-v)})(27\varepsilon^2$$
$$(\frac{ReE}{(1-v)})^2 a^2 U^4 + (1-a^2)(U + (\frac{ReE}{(1-v)})^2 (1-a^2)U^3)^2 + 2a\varepsilon(U^2 + 9(\frac{ReE}{(1-v)})^2 (1-a^2)U^4))^{\frac{1}{2}}\Big].$$
(5.14)

Following the usual Newtonian development (Azaiez and Homsy, 1994a), we assume that $\phi = \phi_r + i\phi_i$ (the subscript r/i from this point onwards will denote the real and the imaginary components) and ϕ_r and ϕ_i (both real valued functions) are even and odd functions of y respectively. Thereby, we restrict the domain of integration to the upper half of the flow such that the boundary conditions at $y = 0$ (or the so called centerline conditions), are altered as follows,

$$\phi_i = \phi_i'' = 0 \tag{5.15a}$$
$$\phi_r' = \phi_r''' = 0. \tag{5.15b}$$

The far stream boundary conditions (or the conditions at $y \to \infty$) is given by

$$\phi_{r/i} = \phi_{r/i}' = 0. \tag{5.16}$$

In § 5.3, we detail a solution procedure for solving the eigenvalue problem (5.8-5.16).

5.3 Solution to the eigenvalue problem

The primary step in evaluating the eigenvalues (α, ω) and the eigenfunction, ϕ, describing the disturbance field (satisfying equation (5.8)) is to probe the ramification of the far stream boundary conditions (5.16) by using the mean flow information at far stream, i. e., $\lim y \to \infty : U(y) = 1, U''(y) = 0$, which simplifies the OSE (5.8) to the following constant coefficient ODE (Sengupta, 2012),

$$\phi^{(4)} - 2\alpha^2 \phi'' + \alpha^4 \phi = \frac{iReS_\infty}{(1-v) + vS_\infty}(\alpha - \omega)(\phi'' - \alpha^2 \phi), \tag{5.17}$$

where $S_\infty = 1 + We(\alpha - \omega)$. The solution to equation (5.17) can be derived by setting $\phi = e^{\lambda y}$, such that one gets the characteristic roots as $\lambda_{1,2} = \mp\alpha$ and $\lambda_{3,4} = \mp Q$, where $Q = \Big[\alpha^2 + \frac{iReS_\infty(\alpha - \omega)}{(1-v) + vS_\infty}\Big]^{\frac{1}{2}}$. The fourth order OSE (5.8) has four fundamental solutions, i. e. $\{\phi_i\}_{i=1}^4$, whose asymptotic variation with $y \to \infty$ is: $\phi_{1,2} \sim e^{\mp\alpha y}$; $\phi_{3,4} \sim e^{\mp Qy}$. Then the general solution which satisfies the far stream conditions (5.16) for real $(\alpha, Q) > 0$, is of the form

$$\phi = a_1 \phi_1 + a_3 \phi_3. \tag{5.18}$$

Equation (5.18) admits a non-trivial solution of the OSE, satisfying the far stream condition (5.16) and the centerline conditions (5.15a, 5.15b) if and only if the determinant of the associated matrix of the linear algebraic system given by equation (5.18), vanishes at $y = 0$, or

$$\left(\phi_1\phi_3'' - \phi_1''\phi_3\right)|_{y=0} = 0, \tag{5.19}$$

for the odd component (equation (5.15a)) and

$$\left(\phi_1'\phi_3''' - \phi_1'''\phi_3'\right)|_{y=0} = 0, \tag{5.20}$$

for the even component (equation (5.15b)), respectively. Equations (5.19, 5.20) serve as the dispersion relation of the problem and will be solved simultaneously. The stiffness of the OSE (5.8) (e. g., in the case of far stream eigenmodes in the limit $Re \to \infty$, we see that $|Q| \gg |\alpha|$, leading to an immense contrast between the two sets of characteristic roots of equation (5.17)) thereby causing the solution components corresponding to the different fundamental solutions to lose linear independence. This source of parasitic error growth necessitates the use of CMM (Ng and Reid, 1985), where one works with a set of following auxiliary variables,

$$y_1 = \phi_1\phi_3' - \phi_3\phi_1', \quad y_2 = \phi_1\phi_3'' - \phi_3\phi_1'', \quad y_3 = \phi_1\phi_3''' - \phi_3\phi_1''',$$
$$y_4 = \phi_1'\phi_3'' - \phi_1''\phi_3', \quad y_5 = \phi_1'\phi_3''' - \phi_1'''\phi_3', \quad y_6 = \phi_1''\phi_3''' - \phi_1'''\phi_3'', \tag{5.21}$$

satisfying the initial value problem (IVP) (Sircar and Bansal, 2019),

$$y_1'=y_2,$$
$$y_2'=y_3 + y_4,$$
$$y_3'=y_5-\left[\frac{(1-\nu)(c_1y_1+c_2y_2+c_3y_3)-\mathscr{F}(iRe(\alpha U-\omega+2\alpha^2\nu)y_2}{(1-\nu)c_4+\mathscr{F}\nu}\right],$$
$$y_4'=y_5,$$
$$y_5'=y_6+\left[\frac{(1-\nu)(c_0y_1-c_2y_4-c_3y_5)+\mathscr{F}(iRe(\alpha U-\omega)+2\alpha^2\nu)y_4}{(1-\nu)c_4+\mathscr{F}\nu}\right.$$
$$\left.+\frac{\mathscr{F}(iRe[(\alpha U-\omega)\alpha^2+\alpha U'']+\alpha^4\nu)y_1}{(1-\nu)c_4+\mathscr{F}\nu}\right],$$
$$y_6'=\frac{(1-\nu)(c_0y_2+c_1y_4-c_3y_6)+\mathscr{F}(iRe[(\alpha U-\omega)\alpha^2+\alpha U''])y_2}{(1-\nu)c_4+\mathscr{F}\nu}$$
$$+\frac{\mathscr{F}\alpha^4\nu y_2}{(1-\nu)c_4+\mathscr{F}\nu}, \tag{5.22}$$

where the initial conditions are estimated by substituting the free stream values of the unknown (i. e., in the limit $y \to \infty$ substitute $\phi_1 \sim e^{-\alpha y}$ and $\phi_3 \sim e^{-Qy}$ in equation (5.21)) and normalizing with respect to one of the variables (e. g., y_1) to remove stiffness. The rescaled initial conditions for solving equations (5.22) are

$$y_1 = 1.0, \quad y_2 = -(\alpha + q), \quad y_3 = \alpha^2 + q\alpha + q^2,$$
$$y_4 = q\alpha, \quad y_5 = -q\alpha(\alpha + q), \quad y_6 = (q\alpha)^2 \tag{5.23}$$

The numerical solution for IVP (5.22, 5.23) is obtained by marching backward from the free stream to the centerline. A suitable value of the eigenpair (α, ω) is obtained by enforcing the dispersion relation (equations (5.19, 5.20)) in auxiliary variables and solving simultaneously, i. e.,

$$\text{Re}(y_2) = 0 \quad \text{at} \quad y = 0 \quad \text{for odd component,} \tag{5.24a}$$

$$\text{Re}(y_5) = 0 \quad \text{at} \quad y = 0 \quad \text{for even component,} \tag{5.24b}$$

respectively. $\text{Re}(\cdot)$ denotes the real part of the complex valued function.

5.4 Results

The zeros of the dispersion relation (equation (5.24)) were explored within the complex $\alpha - \omega$ plane inside the region $-0.02 \leq \omega_r \leq 0.13, -1.6 \leq \omega_i \leq 0.25, \alpha_r \leq 1.6$ and $|\alpha_i| \leq 0.02$. Previous results indicate that the influence of viscoelasticity is fully captured by the modified elasticity number, $E = \frac{(1-\nu)We}{Re}$, a parameter representing the ratio of the fluid relaxation time to the characteristic time for vorticity diffusion Ray and Zaki, 2014. We highlight our instability results versus this parameter. The continuation curves in §5.4.2 and 5.4.3 are depicted within the range $E \in [10^{-3}, 5.0]$ using a discrete step-size of $\triangle E = 10^{-3}$. The numerical solution of the IVP (5.22, 5.23) was determined via the fourth order Runge Kutta integration with a step-size of $\triangle y = 2.2 \times 10^{-3}$. The integration domain was truncated at $\eta = 12.0$ (a point at which the free stream boundary conditions (5.16) were imposed), which leads to a value of the momentum thickness (the reference length scale introduced in §5.2.6), $\delta = 0.30685$. The results in §5.4.2 and §5.4.3 are compared at two different values of Re (i. e., $Re = 40$ and $Re = 400$) as well as, at $\nu = 0.3$ (the elastic stress dominated case) and at $\nu = 0.7$ (the viscous stress dominated case).

5.4.1 Numerical method validation

First, our numerical method outlined in §5.3 is validated by reproducing the absolute and the convective instability results for (a) inviscid mixing layers investigated by Huerre and Monkewitz (Huerre and Monkewitz, 1985) or the Rayleigh instability equation (figure 5.1a), and (b) spatially developing viscoelastic Oldroyd-B mixing layers probed by Ray and Zaki (Ray and Zaki, 2014) (figure 5.1b), using the non-dimensional base-state velocity profile given by

$$U(y) = 1 + S \tanh\left(\frac{y}{2}\right), \tag{5.25}$$

where the parameter S is the ratio of the difference and the sum of the free-stream velocities of the upper and the lower half. In figure 5.1a, we recover the familiar curve of the cusp / pinch points for different complex pairs (α, ω) determined by the numerical integration of the inviscid Rayleigh equation together with the exponentially decaying far stream boundary condition, equation (5.16). Note the crossover from the real-ω axis at the critical value, $S = 1.315$, highlighting a transition from convective instability (i. e., $\omega_i^{\text{cusp}} < 0$) to absolute instability at this value. Figure 5.1b presents the evolution of the critical value of S versus the elasticity number, E, at

$\nu = 0.5$ and $Re = 50, 100, 400, 1000$ for an Oldroyd-B fluid. First, notice the reduction at low elasticity number regime, $E < 0.1$, followed by an enhancement of absolute instability, with increasing E (i. e., the critical value of S eventually drops with increasing E). Second, note that the elasticity number is the dominant flow parameter measuring viscoelasticity while the Reynolds number has negligible influence beyond $Re \geq 400$. A more detailed outlook of the influence of viscoelasticity is acquired by examining the temporal growth rates, described in the next section.
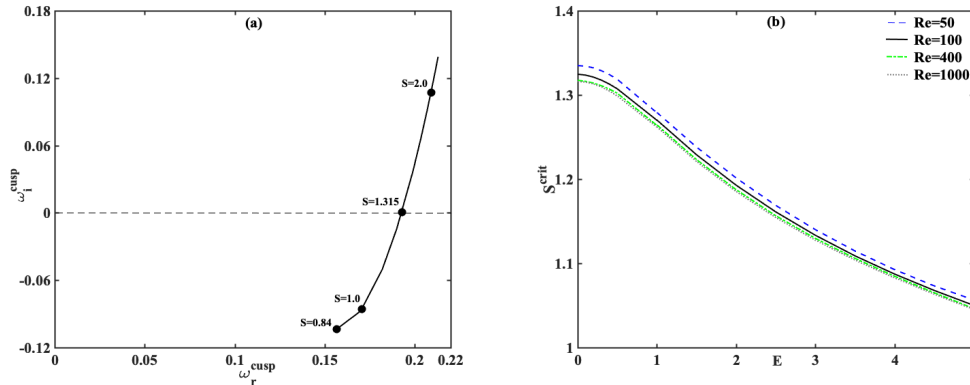
FIGURE 5.1: (a) Locus of the cusp points of the Rayleigh equation in ω-plane at critical values of the parameter, S, and (b) the critical values of S versus elasticity number, E, of the OSE (equation (5.8)) for Oldroyd-B fluids, at $\nu = 0.5$ and $Re = 50, 100, 400, 1000$. The mean velocity profile is given by equation (5.25).

5.4.2 Temporal stability analysis

A positive sign of the temporal growth rate indicates whether absolute instability is possible. The temporal stability analysis for viscoelastic free shear flows in the dilute regime, for low to moderate Re and We, was earlier studied by us (Sircar and Bansal, 2019). In the limit of large Re and We such that $We/Re \sim \mathcal{O}(1)$, Azaiez conducted the temporal stability analysis through an elastic Rayleigh equation and concluded elasticity as the controlling flow parameter within the dilute flow regime (Azaiez and Homsy, 1994a). In this study, we extend these ideas within the non-affine / non-monotonic response regime. Figure 5.2 presents the solution of the OSE (5.8) for purely real wavenumbers, α_r (third column), while allowing angular frequency to be complex number. The other two columns in figure 5.2 are the temporal growth rate or the largest positive imaginary component of any root of the dispersion relation (5.24), ω_i^{Temp} (second column) and the corresponding real part of the frequency (first column). The four models are shown using solid line (Oldroyd-B fluids), dotted line (UCM fluids), dash-dot line (JS fluids, $a = 0.5$) and dashed line (PTT fluids, $a = 0.5, \varepsilon = 0.5$).

First, notice the instability curves (in particular the curves for the UCM fluid) do not start at the same point near $E = 0$. Readers are reminded that the simulation starts at $E_0 = 10^{-3}$, i. e., $E \equiv 0$ (the Newtonian case) is not considered in the present discussion. Further note that the viscous stress dominated case at $Re = 40$, with the exception of the UCM fluid, is unstable in the limit $E \to 0$ (figure 5.2h). This instability occurs at short wavelength (i. e., large α_r, figure 5.2i) and low frequency (i. e.,

small $|\omega_r|$, figure 5.2g). In the dilute regime, the shear flow instabilities were found to arise at zero elasticity number, through a combination of instability via normal stress anisotropy and elasticity (Sircar and Bansal, 2019). In the non-affine regime, we surmise a similar operative mechanism. The overall trend, for large values of E, is that elasticity is stabilizing for UCM fluids (figures 5.2b,e,h,k), stabilizing for PTT fluids at higher Re (figures 5.2e,k) but has negligible small (although stabilizing) influence on Oldroyd-B and JS fluids (ω_i^{Temp} curve is nearly flat in the range $E \geq 3.5$). The mechanism of this elasticity-induced stabilization is well documented by Hinch in an appendix to Azaiez (Azaiez and Homsy, 1994a), and is akin to the action of a 'surface tension'. The stretched polymers contribute to an effective tension along the vibrating membrane that is the shear layer, and this tension damps the perturbations. This important analogy with the surface tension helps to provide a physical explanation for the influence of viscoelasticity on mixing layer stability, in the large-E limit.

The JS as well as the PTT fluids at $Re = 40$ shows a non-monotonic behavior at low to intermediate values of E (figures 5.2b,h) with alternating regimes of stability followed by instability, a feature typical of semi-dilute or moderately concentrated polymeric liquids. These fluctuations are characterized at short wavelengths (figures 5.2c,i) and low frequency (figures 5.2a,g). However, the PTT model 'overestimates' ('underestimates') the instability predicted by the JS model for elastic stress dominated (viscous stress dominated) case at low to intermediate values of E (i. e., compare dashed and the dash-dot curves in figures 5.2b,e versus figures 5.2h,k). In addition, within the range $E \geq 3.5$, while the stability of the Oldroyd-B as well as the JS fluid is almost exclusively a function of E (figures 5.2b,e,h,k), the PTT model produces a more complicated behavior, dependent on all the three parameters, E, Re, ν. The reason for these observations is explained as follows. The JS model is derived from a kinetic theory in which the polymers are represented as beads connected by springs and this underlying assumption of infinitely extensible springs is limiting in the JS model. The finitely extensible (nonlinear) springs of the PTT model arrests the infinite stresses at finite strain rate in extensional flows, leading to a complex pattern described above.

In particular, the PTT results (compared with the JS results at $\nu = 0.7, Re = 400$, figure 5.3a) indicate that a realistic value of the maximum elongation, ε, can induce a significant stabilizing influence of elasticity for large values of E. For small values of ε (i. e., $\varepsilon \leq 0.1$), results are close to those obtained with the JS model. As ε is increased, the (nonlinear) stiffness of the polymer molecules is increased, and one expects a reduction in the (stabilizing) influence of elasticity. We have considered several values of ε, but are particularly interested in results for $\varepsilon = 0.5$. Previous analysis of viscoelastic mixing layers in high Weissenberg number flows have used values between $\varepsilon = 0.3$ and $\varepsilon = 0.7$ (Hagen and Renardy, 1997).

We gain a better understanding of these results and construct a criteria for the recovery of the 'JS behavior' by examining the base-state polymer stresses, τ_0. In steady homogeneous shear flow, the behavior of the base-state polymer stress in the PTT mixing layer is closely related to the standard viscometric results which, in succession, depends on the non-dimensional shear rate (Ferras et al., 2019). At low shear rates, the elongation of the PTT springs is modest, and the PTT and JS models produce similar results. At higher shear rates, the springs become more stretched,
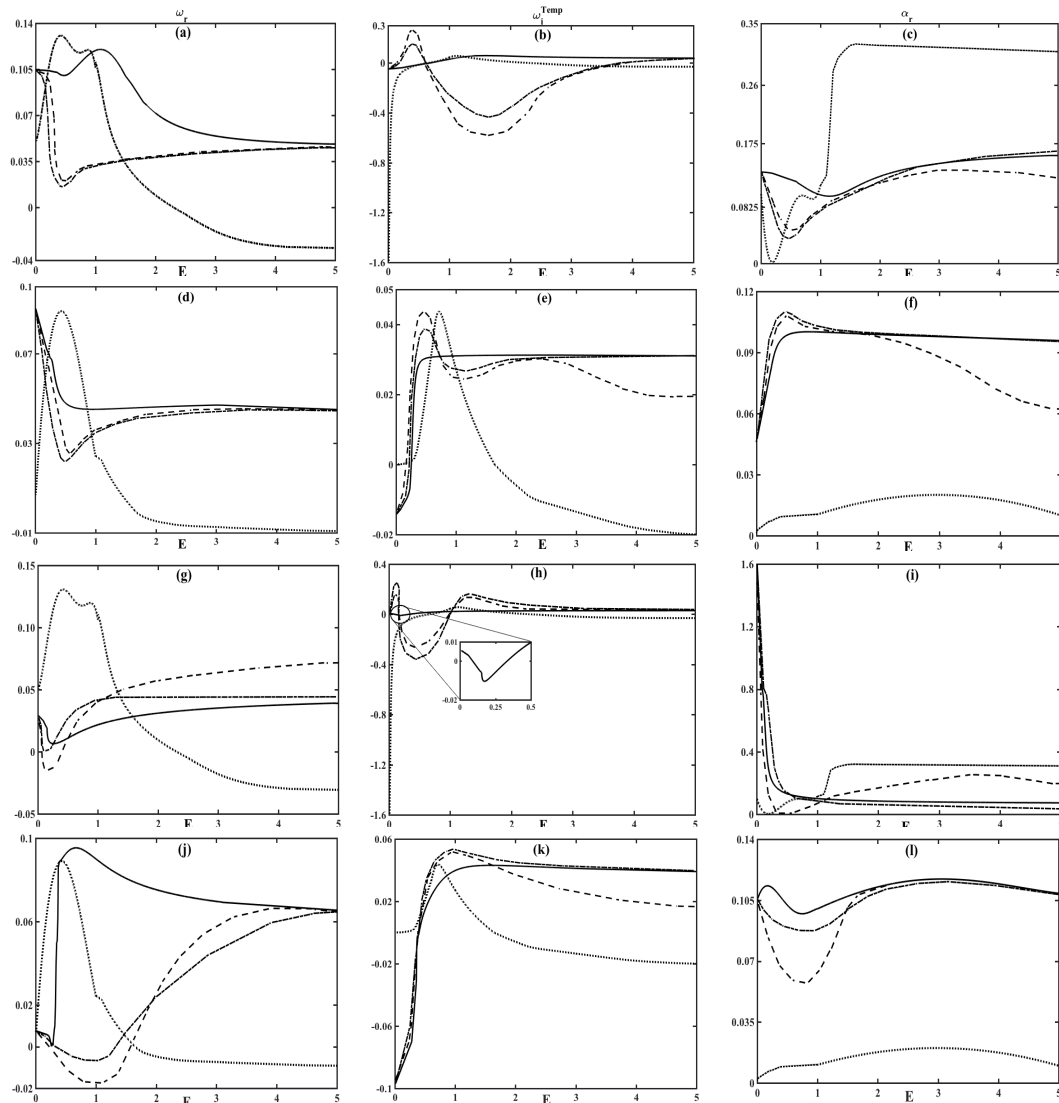
FIGURE 5.2: The frequency, ω_r, (first column); most unstable mode, ω_i^{Temp}, (second column); wavenumber, α_r (third column) for parameters (a-c) $v = 0.3$, $Re = 40$, (d-f) $v = 0.3$, $Re = 400$, (g-i) $v = 0.7$, $Re = 40$ and (j-l) $v = 0.7$, $Re = 400$ versus the elasticity number, E, using using solid, dotted, dash-dot and dashed curves for Oldroyd-B, UCM, JS (at $a = 0.5$) and PTT fluids (at $a = 0.5, \varepsilon = 0.5$), respectively.

nonlinear elasticity becomes important, and the PTT polymer stress components become attenuated relative to their JS counterparts. These trends are present in the tanh mixing layer as well, though the velocity gradient is not constant, and the polymer stress depends on the local shear rate. The role of elongation must also be considered, and using Eqs. (5.13), the ratio of the JS and PTT stress components can be shown to be functions of the shear rate, $\zeta \equiv \varepsilon E U_y$. Figure 5.3b presents the base stresses at $v = 0.7, Re = 400$, with respect to this shear rate at the centerline, $\zeta = \zeta_c = \varepsilon E$. Unsurprisingly, when the shear rate, ζ_c, is small, there is little difference between the PTT and the JS models, but at larger values of ζ_c, the JS stress is larger. We can foresee that the relative attenuation of the base stresses as ζ_c is increased, is connected to the stabilizing influence of elasticity which was observed in our temporal stability results. Conversely, we would expect to recover the JS behavior if ζ_c is less than some critical value, $\zeta_c^* = 0.126$, i. e., the ratio of all the base stresses are less than 90% beyond this critical value of ζ_c. A better characterization of these instabilities are revealed through the spatiotemporal analysis in §5.4.3.
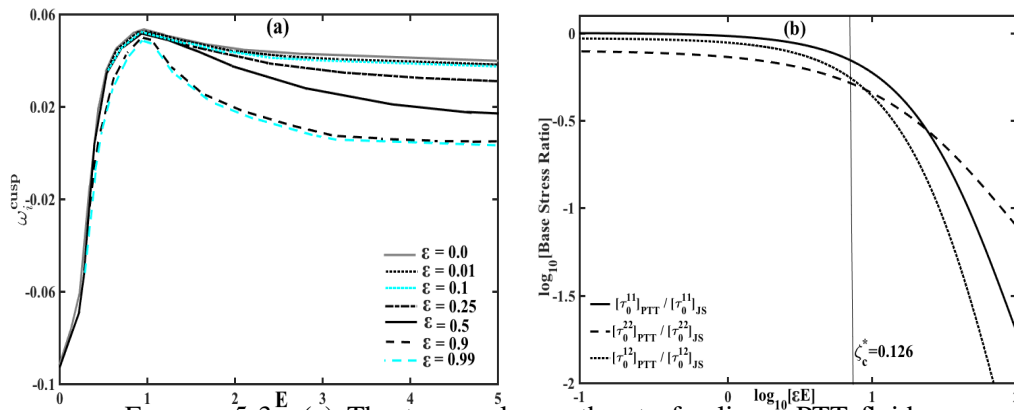
FIGURE 5.3: (a) The temporal growth rate for linear PTT fluids, ω_i^{Temp} versus E, and (b) the log-log plot of the ratio of the PTT versus JS base stresses as a function of the centerline shear rate. Other parameters are fixed at $a = 0.5, v = 0.7, Re = 400$ and $\varepsilon = 0.5$ for plot (b).

5.4.3 Spatiotemporal stability analysis

Spatiotemporal analysis is typically relevant when one introduces an impulse excitation locally in a flow and observes how that disturbance evolves. In an effort to determine the range of E (for fixed Re and v) for which the flow regimes are absolutely unstable, convectively unstable or temporally stable, we recover the absolute growth rate (or the growth rate at the cusp point, ω_i^{cusp}, figure 5.4) starting from the most unstable temporal mode, ω_i^{Temp}. The cusp point in the $\omega-$plane is a saddle point satisfying the criteria, $D(\alpha, \omega^{cusp}) = \frac{\partial D(\alpha, \omega^{cusp})}{\partial \alpha} = 0$ but $\frac{\partial^2 D(\alpha^{pinch}, \omega^{cusp})}{\partial \alpha^2} \neq 0$ (where $D(\alpha, \omega) = 0$ is the dispersion relation). However, not all cusp points are unstable and, in particular, the evanescent modes are segregated from the regular cusp points using the Briggs idea of analytic continuation (Kupfer, Bers, and Ram, 1987). While the Oldroyd-B model is presumed to represent the dilute polymeric liquids, the linear PTT model (due to the finite, nonlinear elongation of the polymer chains

at $a = 0.5, \varepsilon = 0.5$) portrays the instability transition for moderately concentrated polymeric liquids. A discontinuity in the curves in figure 5.4 indicates a region of temporal stability.

The instability pattern shown in figure 5.4 is a result of a complex interplay between the inertial forces (proportional to Re) and the normal stress anisotropy through elasticity (proportional to E). For example, within the lower elastic number regime (i. .e., $E < 0.5$) the dilute polymeric liquids display constricted regions of temporal stability at higher value of Re (comparing the solid curve at $Re = 40$ (figure 5.4a) versus the curve at $Re = 400$ (figure 5.4b)). Similarly, the viscous stress dominated case reveals (convective) instability at lower value of Re and E (figure 5.4c). Clearly, while the former observation is the result of inertia, the latter is the outcome of instability generated via polymer elasticity. Analogous with the temporal stability analysis, we find that the absolute growth rate of the PTT fluids in the high elastic number regime is always lower than the JS fluids. This is because the finite elongation attribute of the PTT fluids is able to rein in the large elastic stress gradient buildup.

To explore the nature of these instabilities, we compute the boundaries of the temporally stable regions (**S**), convective instabilities (**C**), evanescent modes (**E**) and absolute instabilities (**A**) within a selected range of flow-elasticity parameter space, i. e., $Re \in [0.1, 400], E \in [10^{-3}, 5]$ and $\nu = 0.3$ (figure 5.5a) and $\nu = 0.7$ (figure 5.5b). The boundaries of the temporally stable, convectively unstable and absolutely unstable region, for dilute liquids in the elastic stress dominated case (figure 5.5a) are numerically estimated to reside within the range $E < 0.3$, approximately $0.3 \leq E \leq 1.5$ and $E > 1.5$ (for all values of Re), respectively. In contrast, the concentrated polymeric liquids exhibit temporal stability and absolute instability in a confined region, i. e., $E < 0.1$ and $E > 4$, respectively. For the viscous stress dominated case (figure 5.5b), the dilute as well as the concentrated liquid reveals convective instability within the range $Re < 150$ and $E < 0.1$ (including in the limit $Re \ll 1$) which is followed with alternating regions of (temporal) stability and (convective) instability for larger values of E. Absolute instability is unveiled by the Oldroyd-B fluids for $E > 1.5$ and by the PTT fluids for $E > 1.0$, for practically all values of Re.

We discuss the significance of the temporal stability analysis (figure 5.2) as well as the spatiotemporal phase diagram (figure 5.5) in relation to the experiments for Newtonian as well as viscoelastic flow past a cylinder, since the shear layer instability is closely related to the instability of the cylinder wakes (Pipe, 2005). In the case of Newtonian wakes for $Re < 1$, the flow past a cylinder is steady and without recirculation (Taneda, 1956). The emergence of a locally, convectively unstable wake is detected at $Re \approx 5$, whereby the selected perturbation are amplified and convected downstream but ultimately leave the flow undisturbed (Monkewitz, 1988). The locally most unstable part of the wake becomes absolutely unstable at $Re \approx 25$, although this is not sufficient for self-sustained global oscillations of the wake. At $Re \approx 47$ the region of absolute instability in the wake is large enough for the wake to sustain time-amplified oscillations, which is followed by the onset of the laminar two-dimensional von Kármán instability (J. M. Chomaz and Redekopp, 1988). This transition to global instability has been ascribed to a supercritical Hopf bifurcation towards a limit cycle (Provansal, Mathis, and Boyer, 1987) and the linear stability analysis appears to faithfully describe the Newtonian wake dynamics, 'unreasonably' far above the global instability threshold of Re (Oertel, 1990).
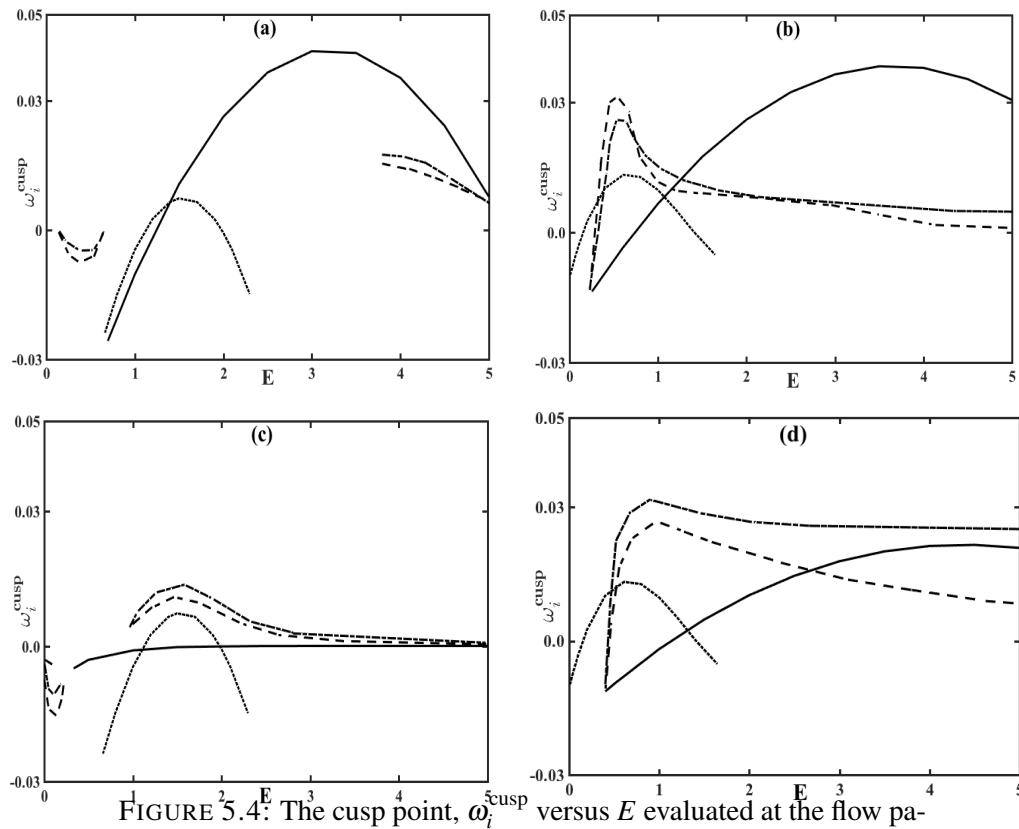
FIGURE 5.4: The cusp point, ω_i^{cusp} versus E evaluated at the flow parameters, (a) $\nu = 0.3, Re = 40$, (b) $\nu = 0.3, Re = 400$, (c) $\nu = 0.7, Re = 40$, and (d) $\nu = 0.7, Re = 400$, shown using solid, dotted, dash-dot and dashed curves for Oldroyd-B, UCM, JS (at $a = 0.5$) and PTT fluids (at $a = 0.5, \varepsilon = 0.5$), respectively.

In contrast, first notice that all four stress constitutive relations in the phase diagram in figure 5.5 indicates a convectively unstable region for moderate values of E. For the elastic stress dominated case, figure 5.5a, this region lies in the range $0.6 \le E \le 0.7$ (Oldroyd-B), $E_0 \le E \le 0.1$ (UCM), $0.5 \le E \le 0.6$ (JS and PTT); and for the elastic stress dominated case, figure 5.5b, this region lies in the range $0.8 \le E \le 1.1$ (Oldroyd-B), $E_0 \le E \le 0.1$ (UCM), $0.5 \le E \le 0.6$ (JS and PTT); for significantly larger values of Re (i. e., $Re > 47$). This observation is in congruence with the early experimental studies of viscoelastic vortex street highlighting the reduction in the vortex shedding frequency (related to the temporal growth rate in the present study) (Kalashnikov and Kudin, 1970), as well as in the intensity of the vorticity (Cadot and Kumar, 2000), namely the origin of inertial turbulence modified by elasticity. Second, notice the appearance of convectively unstable region for the viscous stress dominated case, for small values of E and in the limit $Re \to 0$. This result corroborates the experimental findings of McKinley *et al.* (McKinley, Armstrong, and Brown, 1993) showing instability induced by elasticity for viscoelastic flow past a cylinder at $Re \ll 1$ as well as the findings of Coelho and Pinho (Coelho and Pinho, 2003) showing a significant destabilization of the wake for shear-thinning, elastic fluids at $Re < 40$, in other words the presence of elastic turbulence.

Two other observations are noteworthy: first, the Oldroyd-B, JS and the PTT models suggest absolute instability for sufficiently large values of E (i. e., $E > 4$ ($E > 1.5$) for the elastic (viscous) stress dominated case, figure 5.5a versus 5.5b) and second, the presence of a temporally stable region for the JS and PTT models for the elastic stress dominated case (figure 5.5a), approximately within the range $0.6 < E < 4$ and $Re < 100$. While the former observation signifies a pathway to elastoinertial turbulence (appearing at moderate Re and large E) which characterizes the maximum drag reduction state and even originates in linear instability studies of pipe flows (Chaudhary et al., 2021), the latter observation indicates an intricate tug-of-war between the inertial destabilization and elastic stabilization. While the presence of the first region was recently substantiated (Samanta et al., 2013), a comprehensive experimental ratification of the second region is eagerly awaited.
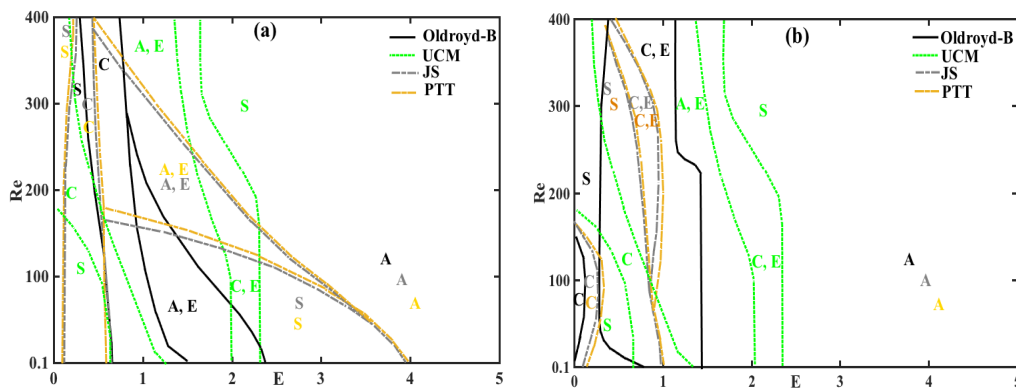
FIGURE 5.5: Viscoelastic free shear flow stability phase diagram at (a) $\nu = 0.3$, and (b) $\nu = 0.7$, in the E–Re parametric space. The regions **S**, **C** and **A** are denoted by temporally stable, convectively unstable and absolutely unstable regions, respectively. The domains outline by (**A**, **E**) and (**C**, **E**) are those where both the stable and evanescent modes (denoted by **E**) are found.

5.5 Conclusions

This investigation addresses the linear, temporal and the spatiotemporal analyses of free shear flows of dilute as well as moderately concentrated polymeric liquids for low to moderate Reynolds number and Elasticity number, by capturing the non-affine flow response of a 'tanh' base flow mixing velocity profile. Section 5.2 presented the viscoelastic free shear flow model as well as the elements of the linear stability analysis via the solution of the Orr-Sommerfeld equation. Section 5.3 demonstrated the steps of the Compound Matrix Method, utilized to numerically solve the resultant system of stiff differential equations. The temporal stability analysis in section 5.4.2, indicates (a) elastic stabilization at higher values of elasticity number and (b) a non-monotonic instability pattern at low to intermediate values of elasticity number for the JS as well as the PTT model. The spatiotemporal phase diagram in section 5.4.3 divulge the familiar regions of inertial and elastic turbulence, a recently verified region of elastoinertial turbulence and the unfamiliar temporally stable region for intermediate values of Reynolds and Elasticity number.

Although this study provides an improved understanding of the linear dynamics of mixing layers for dilute to moderately concentrated polymeric liquids, a number of simplifying assumptions were made, and the relaxation of these assumptions paves a way for further progress. Understanding the importance of base flow spreading, confinement and nonlinearity as well as the consideration of the shear flows of polymer melts (or fluids with very large viscosity) are of substantial importance. Finally, we note that we have considered only the two-dimensional instabilities which is a common simplification in the absolute / convective instability studies of Newtonian flows where Squire's transformation can be applied (Squires and Quake, 2005). A modified Squire's transformation for Oldroyd-B fluids also exist (Bistagnino et al., 2007), but we are not aware of a similar result for the PTT model. Hence, a consideration of the three-dimensional instability modes in future studies with the PTT model may be worthwhile.

Chapter 6

Conclusions: challenges faced and future problems

6.1 Introduction

In the first part of this final chapter, we discuss the challenges and the difficulties faced in the numerical simulations as well as the linearized approximations of the free shear flows. In the second part of this chapter, we review three different types of viscoelastic surface instabilities which will form the basis of our future investigation: The Rayleigh-Plateau, the Saffman-Taylor and the Faraday instabilities. These instabilities are classical examples of hydrodynamic surface instabilities, whose complete theoretical description is still lacking.

6.2 Challenges faced in viscoelastic fluid simulations

Some of the most challenging problems in the numerical simulation of viscoelastic flows are associated with singularities or boundary layers which occur in the high Weissenberg number limit. Another challenge is the reentrant corner singularity which arises in contraction flows. The stresses and deformation rates at a reentrant corner are infinite, and therefore the local Weissenberg number at the corner is infinite, regardless of what the global Weissenberg number of the flow is. The numerical resolution of the corner singularity has been problematic, and the upper convected Maxwell model has been particularly recalcitrant. A third difficulty in numerical simulations is the resolution of the stress boundary layers on walls: a feature more pronounced for the upper convected Maxwell model.

6.2.1 High Weissenberg Number problem

In many ways, the problem of high Weissenberg number problem for viscoelastic flows is similar to high Reynolds number problem for Newtonian flows. The first thing one does when dealing with a problem involving a small parameter is to set this parameter equal to 0. Thus, for high Reynolds number flows, the first step is to investigate what happens when viscosity is neglected entirely; this leads to the Euler equations. Below, we shall see that there is a counterpart of the Euler equations for the high Weissenberg number limit in viscoelastic flows. Rather curiously, the high Weissenberg number limit of the upper convected Maxwell fluid is actually related

to the Euler equations (Sengupta, 2012). The Euler equations, however, cannot describe all the relevant features of high Reynolds number hydrodynamics. First, the Euler equations require fewer boundary conditions than the Navier-Stokes equations. This leads to boundary layers in which viscous effects cannot be neglected. We shall see that boundary layers also arise in high Weissenberg number flows, even though these elastic boundary layers have nothing to do with satisfying boundary conditions (Azaiez and Homsy, 1994b). Another problem with the Euler equations is that they allow a lot of nonuniqueness. For instance, in the flow through a pipe, the Euler equations allow an arbitrary steady parallel velocity profile, plus a multitude of unsteady and nonparallel flows. Just from the Euler equations we can, therefore, learn nothing about the velocity profile which actually establishes itself in a high Reynolds number pipe flow.We shall find a similar situation in the case of high Weissenberg number flows.

6.2.2   Corner Singularities

Interest in the mechanics of viscoelastic flow past sharp corners has been stimulated by attempts at numerical solution of axisymmetric and plane flow through sudden contractions (Boger and Walters, 1993). The difficulties encountered in obtaining convergent solutions for Oldroyd fluids and its generalizations at large values of the Weissenberg number has been widely documented (Keunings, 1989). There is still no general agreement regarding the convergence problems, although most investigators believe that the major difficulty is associated with the resolution of very large stress gradients emanating from comer singularities.

Knowledge of the behavior in the neighborhood of a comer would enable the construction of elements that incorporate the strength of the singularity. This problem is unsolved in general and remains one of the most pressing outstanding issues in viscoelastic fluid mechanics. Most of the attention has focused on fluids for which the retardation time is equal to zero. It is easily shown for $a = -1$ that the stream function cannot be expressed as a power in distance from the comer. (G. G. Lipscomb, 1987) have shown that for a "second-order fluid," the strength of the stress singularity is twice that of the Newtonian fluid; this leads in some cases to a nonintegrable stress. Their finite-element simulations for a Maxwell fluid are consistent with this ordering up to the element closest to the comer, and they conclude that even when the stress is integrable, it would exceed the known bond strength of the materials (hence requiring relaxation of the no-slip condition). (Davies, 1988) has obtained a complete solution for the corotational derivative ($a = 0$). The comer stresses for $a = 0$ are in fact bounded, but values of a close to zero are unlikely to be of physical significance. There is widespread speculation that the presence of the retardation time ensures that the stress singularity will be of the same order as that for a Newtonian fluid.

6.2.3   High Weissenberg Number boundary layer

In contrast to the case of high Reynolds number flows, the boundary layers observed in viscoelastic flows have nothing to do with boundary conditions. The boundary condition in both cases is the no-slip condition. The elastic boundary layers, however, showno steep gradient of velocity; instead, it is primarily the stresses which

change radically across the boundary layer. Indeed, the boundary layer is found even if the velocity field is prescribed and only the integration of stresses from the constitutive law is considered. The physical reason for the formation of a stress boundary layer is as follows: at the wall, the velocity is 0. Hence, the stresses are determined completely by the local velocity gradient, and they are given by the steady viscometric functions. At some distance from the wall, however, the memory of the fluid is important, and the stresses are determined by the velocity gradients over some distance along the streamline. If the Weissenberg number is large, this leads to a sharp transition in stress behavior close to the wall.

6.3 Future problems: spatiotemporal analysis for viscoelastic surface instabilities

In this section, we review three typical hydrodynamic surface (or more general interfacial) instabilities: the Rayleigh–Plateau instability, the Saffman–Taylor instability and the Faraday instability. These instabilities were chosen as they are each representative of a more general class of pattern-forming systems and I intend to investigate each. Here we discuss the modifications of these instabilities that occur when using viscoelastic fluids instead of simple Newtonian liquids.

6.3.1 Rayleigh-Plateau instability

6.3.1.1 Newtonian liquids

A liquid column with a free surface always disintegrates into smaller droplets because surface tension leads to minimization of the surface-to-volume ratio. Rayleigh showed that the size R of the droplets is determined by the wave length λ of the sinusoidal distortion with the fastest growth rate. For the inertia-dominated case, i.e., for low viscosity liquids, one finds $\lambda \approx 9r$ with the radius r of the column. For the pending droplet, a similar scenario holds. When a pending droplet is fed quasistatically via a syringe pump, it starts to fall if gravitation overcomes capillary forces. However, as soon as the droplet begins to fall, surface tension again leads to minimization of its surface area and acts as the main pinching force (Clanet and Lasheras, 1999; Rothert, Richter, and Rehberg, 2003; Wagner et al., 2005). Thus, the primary stages of the pinch-off of a droplet can be modeled as a Rayleigh instability. The thinning dynamics of the neck radius, shown in Fig. 6.1, can be fitted with an exponential law corresponding to exponential growth of the amplitude of the most unstable wavelength. The growth rates fit well with the predictions made by Rayleigh's theory (Wagner et al., 2005).

During the final stages of the pinch-off process in the nonlinear regime, the situation becomes very different. The system no longer reflects the original geometry, e. g., the diameter of the nozzle, but instead depends on material parameters (density, surface tension and viscosity) only. The dynamics of this finite time singularity in which the minimum neck diameter reaches zero in finite time can be described by self-similarity solutions. For the low viscosity and thus inertia-dominated regime, which applies in the case of water, it follows that the minimum neck radius approaches zero such that $r(t) \sim (t - t_c)^{2/3}$ (Fig. 6.1) (Eggers, 1993).
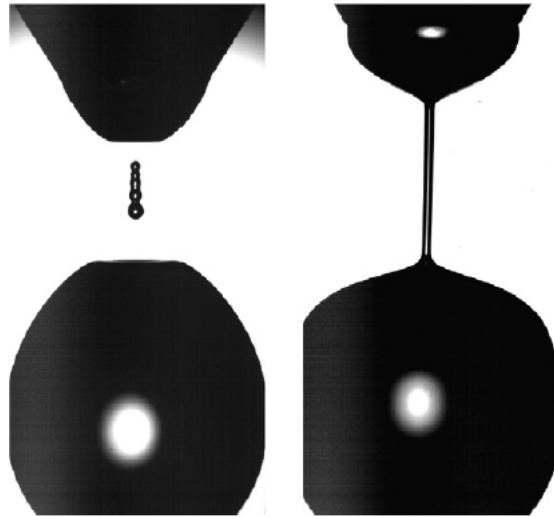
FIGURE 6.1: Left image: Water droplet falling from nozzle. Right image: Same experiment repeated after the addition of 100 ppm polymer solution, mol. weight 4×10^6 g/mol (Source (Lindner and Wagner, 2009)).
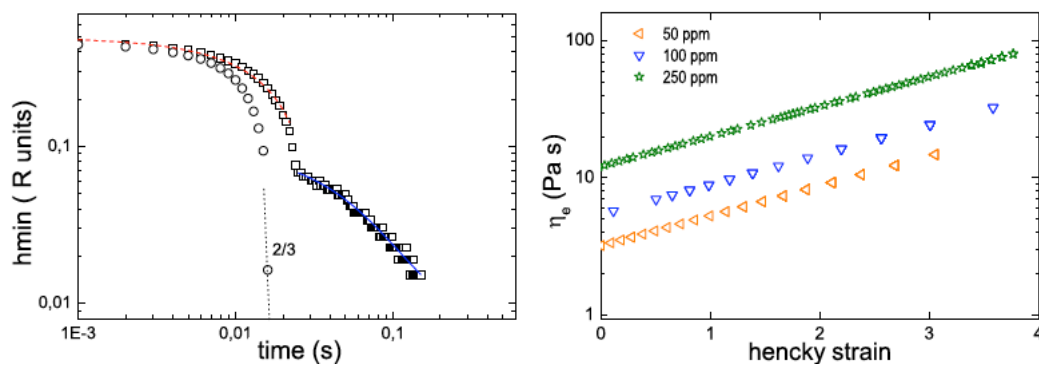
FIGURE 6.2: Left image: Minimum neck diameter h_{min} vs. time for water (○) and 100 ppm polymer solution (mol. weight 4×10^6 g/mol) in water (□). Right image: The elongational viscosity for different concentrations of the polymer solution as a function of the Hencky strain, a measure of elongation (Source (Lindner and Wagner, 2009)).

6.3.1.2 Polymeric liquids

The effect of elasticity on the (linear) dynamics of the Rayleigh-Plateau instability can be best studied theoretically by use of the (linear) Maxwell model. Chang et al. (Chang, Demekhin, and Kalaidin, 1999) performed a linear stability analysis and predicted slight variations of the critical wave numbers and of the growth rates due to linear elasticity.

In the experiments presented in Fig. 6.1, solutions of the flexible polymer at low concentrations (10-2000 ppm) in a low viscosity solvent were used. In these solutions, elastic contributions at small deformations are weak and, as a consequence, the complex viscosity η^* is difficult to determine by small amplitude oscillatory shear rheometry. This means that, for small deformation, the polymers do not affect the flow. Indeed, the experimental results (refer Fig. 6.2) show that the dynamics of the primary stages of the detachment process are not altered. Only when the flow (and

thus the elongation) is strong enough do the polymers become stretched, interrupting the finite time singularity of the pinch-off process. Instead, one observes the formation of a filament and an abrupt transition to a new exponential regime with a much larger time scale. This inhibition of the finite time singularity was first observed by Amarouchene et al. (Amarouchene et al., 2001).

This is a surprising observation because it means that the elastic stresses in the liquid that balance the stresses from the surface tension are much higher than for the case of the pure solvent (Fig. 6.2). Still, the shear viscosity of the sample is close to the solvent viscosity. The solution to this apparent contradiction is the following: any type of flow can be divided into a rotational and an elongational part. The elongational part stretches the polymers and induces stresses. The rotational part, e. g., in shear flow, causes the polymers to tumble and stresses are averaged out to a large degree. In the filament, the flow is purely elongational and stretches the polymers most efficiently. This leads to the so called elongational viscosity η_e. For Newtonian liquids, the elongational viscosity η_e is directly given by geometrical considerations and it follows $\eta_e = 3\eta_{shear}$. The factor 3 is called the Trouton ratio. For polymers, the situation is less clear and measurements of the elongational viscosity are non-trivial. The growing elastic stresses in the filament stabilize the flow, since any distortions would lead to further stresses. This makes the filament very robust and we might expect a Rayleigh-Plateau-like instability to be observed only at the very end of the thinning process when the polymers are fully stretched and elastic stresses cannot increase further. However, in most of the experiments, a more or less irregular instability scenario is observed at the very end of the thinning process and singular 'beads' grow on the filament. In a numerical study, Chang et al. (Chang, Demekhin, and Kalaidin, 1999) predicted that the filament should start to disintegrate from both ends where it is connected to the falling droplet and the reservoir in the nozzle. At these points, the curvature and surface stresses are maximal. Experimentally, Oliveira et al. (Oliveira and McKinley, 2005; Oliveira, Yeh, and McKinley, 2006) found an iterative process between generations of larger and smaller beads, but their range of observations was limited. Experimental data obtained by Sattler et al. (Sattler, C.Wagner, and Eggers, 2008) indeed revealed an instability process that was triggered from the ends. In contrast to previous studies, in which the plates where pulled apart abruptly, in these experiments the separation was performed very gently in order to prevent any additional distortions. Though in most of the experiments singular droplets grew on the filament, it was possible to observe the exponential growth of a coherent sinusoidal pattern (Sattler, C.Wagner, and Eggers, 2008). The inverse growth rate of the pattern was found to be $1/\omega = 9.3 \pm 0.1$ ms. Linear stability of a viscous fluid thread [1] predicts $\omega = \gamma/(6R_0\eta_{eff})$, resulting in an estimated extensional viscosity of $\eta_{eff} = 9$ Pa s ± 2, more than one order of magnitude smaller than the extensional viscosity $\eta_E(12\mu$ m$) = 100$ Pa s estimated above, but nevertheless four orders of magnitude higher than the shear viscosity. The exponential regime was followed by the final shrinking of the remaining thread between the beads, which followed a linear law as expected for highly viscous liquids (Eggers, 1997; Rothert, Richter, and Rehberg, 2003).

Finally, we outline the answer to the question of how the filament finally breaks. For polymer concentrations greater than 1000 ppm, it was observed that the liquid filament connecting two beads did not break; instead, a pattern that resembles

a solid fiber. The beads sit alongside the filament; experiments on fluid drops on a fiber (Carroll, 1986) show that there must be a finite contact angle between the drops and the filament for such a symmetry breaking to occur. It follows that the thin filament must have formed a (solid) phase different from that of the drops (James and Saringer, 1980). Our interpretation of this experimental data is that, due to the coupling of stress fluctuations and concentration fluctuations, a flow-driven phase separation takes place. Microscopically, one can imagine that while solvent drains from the filament, the polymers become entangled, leading to even higher polymer concentration and increased entanglement, i.e., flow-induced phase separation takes place (Kume et al., 1997). Further evidence for this concentration process was found in (Sattler, Kityk, and Wagner, 2007), where birefringence measurements were performed to examine molecular conformations in the break-up process. Evaporation can be excluded as a factor in the formation of solid fibers, based on experiments in a two-fluid system.

6.3.2 Saffman-Taylor instability

6.3.2.1 Newtonian liquids

The classical Saffman-Taylor instability occurs when, for example, air pushes a viscous fluid in a narrow channel of height b and width W, a so-called Hele-Shaw cell. In the following, the viscosity of air is neglected and the viscosity of the viscous liquid is given by η. The surface tension between the two fluids is σ and the viscous liquid is considered to perfectly wet the channel.

Flow in the confined geometry is then governed by Darcy law, which gives the mean velocity (averaged over the thickness of the channel) of the fluid as a function of an applied pressure gradient: $\mathbf{V} = -\frac{b}{12\eta}\nabla p$. The incompressibility of the fluid reads $\nabla \cdot \mathbf{V} = 0$ and one thus deals with growth in a Laplacian pressure field $\nabla p = 0$. The pressure jump at the interface is given by $\delta p = \sigma(\frac{2}{b} + \kappa)$, with κ being the curvature in the direction of the channel width, once again using a two-dimensional approximation. Together with the boundary conditions, this set of equations completely determines the problem.

When the less viscous fluid pushes the more viscous fluid, an initially straight interface becomes unstable. Small perturbations lead to an increased pressure gradient and a higher velocity in front of the perturbations and are thus amplified. Surface tension, on the other hand, stabilizes the initially straight interface. The competition between viscous and capillary forces leads to the emergence of a characteristic length scale that can be calculated using linear stability analysis (Chuoke, Meurs, and Poel, 1959). The maximum growth rate is found for a wavelength $l_c = \pi b/\sqrt{Ca}$ with capillary number $Ca = \eta U/\sigma$. The small fingers grow and begin to compete with the more advanced fingers, screening the less advanced fingers. In a linear channel of width W, one finally observes a single finger propagating through the cell, the result of a nonlinear growth process. An example of initial finger growth and finger competition, together with the growth rate obtained from the linear stability analysis, can be seen in Fig. 6.3 left. The relative width of the single finger λ, defined as the ratio between the finger width w and the cell width W, is given by the control parameter $1/B = 12Ca(W/b)^2$, that is, the ratio between the two length scales of the system W and l_c. Representation of the results obtained using different fluids (and
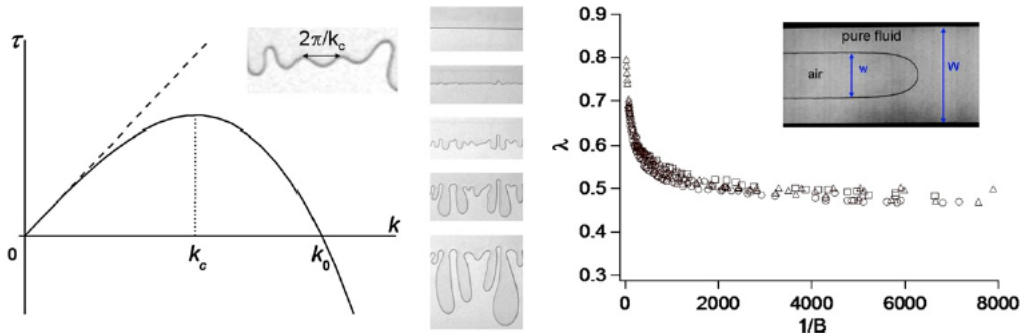
FIGURE 6.3: Left image: Growth rate τ as a function of the wave number k. The most unstable wavelength l_c is given by $2\pi/k_c$. Inset: Snapshots of the destabilization of the planar front between air and silicon oil. Right image: Relative finger width λ as a function of surface tension for air pushing silicon oils of different viscosities in channels of different geometries. Inset: snapshot of a finger advancing into a linear cell (Source (Lindner, Bonn, and Meunier, 2000)).

thus different surface tensions or different viscosities) and different cell geometries as a function of the control parameter $1/B$ shows that the results fall on a universal curve (see Fig. 6.3 right). With increasing velocity U of the finger tip, viscous forces become increasingly important compared to capillary forces and the relative finger width decreases. At high velocity, the finger width does not, however, tend to zero but stabilizes near a plateau value at $\lambda = 0.5$.

This instability was described by Saffman and Taylor in 1958 (Saffman and Taylor, 1958); however, finger selection remained a puzzle for several decades. Neglecting surface tension, Saffman and Taylor found a family of analytical solutions of the shape of the interface given by $x = \frac{W(1-\lambda)}{2\pi} \ln[\frac{1}{2}(1 + \cos\frac{2\pi y}{\lambda W})]$ that agrees well with experimental observations. This treatment does not, however, explain the selection of a given finger width. For this, one must take the surface tension into account. This was done numerically by McLean and Saffman in 1981 (McLean and Saffman, 1981). The selection process was solved analytically only much later (Combescot et al., 1986) and was attributed to the fact that the surface tension represents a singular perturbation leading to a solvability condition at the finger tip. It is this condition that selects the finger from the family of solutions found by Saffman and Taylor.

The Saffman-Taylor problem is ideally not a two-dimensional problem. In reality, there is a thin wetting film that remains between the advancing finger and the glass plates. The thickness of this film, according to the Bretherton law, is proportional to $Ca^{2/3}t/R = 0.643(3Ca)^{2/3}$ (Tabeling and Libchaber, 1986). As a consequence, the pressure jump at the interface is continuously modified. This three-dimensional effect leads to the slight modification of the finger width observed between different experimental geometries, as observed in Fig. 6.3.

6.3.2.2 Polymeric liquids

When performing experiments in dilute solutions of xanthane, one observes a strong modification of the selection process. As can be seen in the snapshot in Fig. 6.4 left, at high velocity, fingers are found to be significantly narrower than the classical limit of $\lambda = 0.5$. This observation can be qualitatively linked to the behavior of the
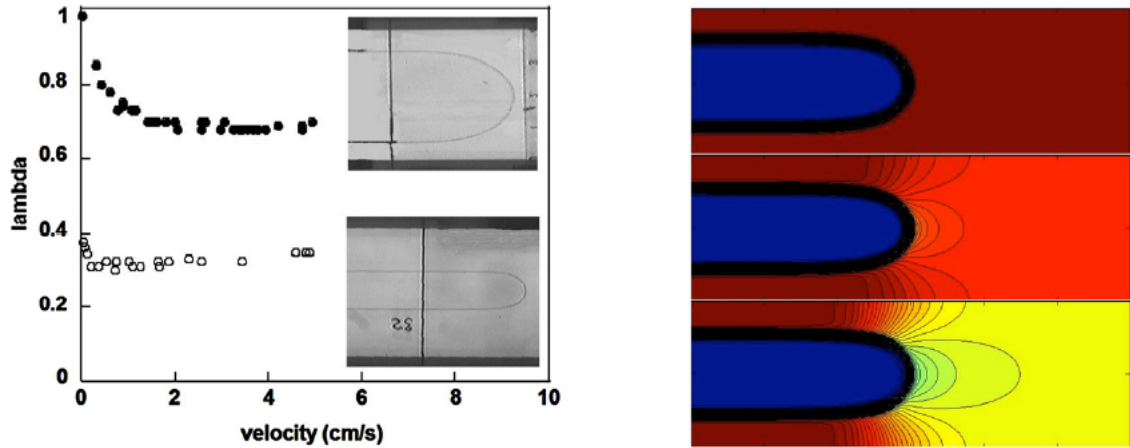
FIGURE 6.4: Left image: Relative finger width as a function of the velocity for solutions of xanthane (○) at 1000 ppm and (●) at 50 ppm. Inset: snapshots of fingers in the two solutions at high velocity. Right image: Viscosity in front of the advancing finger in a shear thinning fluid found from numerical simulations. The shear thinning effect increases from top to bottom. Red corresponds to high viscosities and yellow to low viscosities. (Source (Kondic, Shelley, and Muhoray, 1998)).

shear thinning fluid pushed by the finger in the Hele-Shaw cell. Numerical simulations (Kondic, Shelley, and Muhoray, 1998) show that the viscosity is not uniform throughout the cell (see Fig. 6.4 right); regions of high fluid velocity and thus high shear rate have a low viscosity. This is essentially the case in front of the finger tip and the system becomes anisotropic, leading to finger narrowing.

For weak shear thinning, it is shown (Lindner et al., 2002) that simply replacing in the control parameter $1/B$ the constant viscosity η by a shear-dependent viscosity $\eta(\dot{\gamma})$ one allows rescaling the data onto the universal curve for Newtonian fluids. The shear rate $\dot{\gamma}$ is here the average shear rate in the cell. For stronger shear-thinning, this rescaling fails and deviations from the classical result toward smaller fingers are observed.

Narrower fingers have also been observed by Rabaud et al. (Rabaud, Couder, and Gerard, 1988). Using a Hele-Shaw cell with engraved glass plates, they found viscous fingers with λ significantly smaller than 0.5 for Newtonian fluids. The observation of such 'anomalous' fingers is explained by the fact that the engravings represent a local perturbation at the finger tip. This disturbance removes the classical selection of the discrete set of solutions. The continuum of solutions given by the analytical result of Saffman and Taylor without surface tension then becomes accessible: λ can take values smaller than 0.5 at high velocity. Rabaud et al. showed that for a given value of the capillary number Ca, it is not the relative finger width that is selected but that the dimensionless radius of curvature at the tip ρ/b. ρ can be linked to the finger width λ via the relation $\rho = \frac{\lambda^2 W}{\pi(1-\lambda)}$, which follows from the finger shape predicted by Saffman and Taylor.

A similar mechanism has been found to be responsible for the selection of the viscous fingers in a shear thinning fluid. Here when the shear thinning character of the fluid is strong enough, anisotropy plays the role of the perturbation at the finger tip. Fig. 6.5 left shows experimental finger profiles for a given capillary number and three
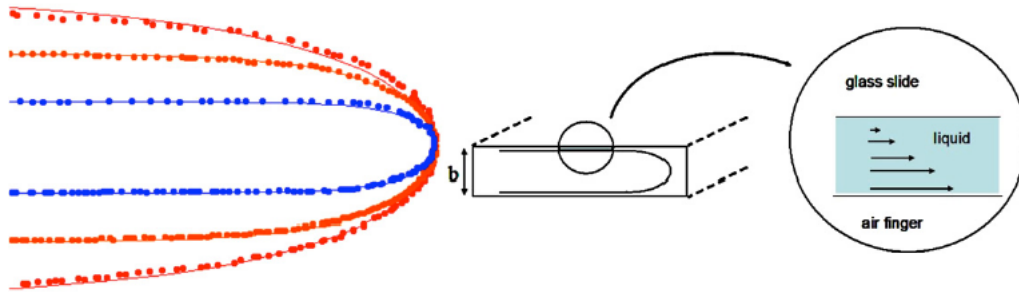
FIGURE 6.5: Left image: Experimental finger shapes in a solution of xanthane of 2000 ppm for three different channel widths $W = 2, 4$ and 8 cm. Right image: Sketch of the thin wetting layer observed between the finger and the glass plates. (Source (Lindner and Wagner, 2009)).

different cell widths. One clearly observes that the radius at the finger tip is identical for the three experiments, leading to lower finger width compared to the Newtonian case, in which the relative finger width λ is selected. The relation between ρ/b and λ is found to depend on the shear thinning character of the fluids. Knowledge of the relationship between ρ/b and λ solves the selection problem, as we can now predict the finger width λ from the rheological data. The presence of shear thinning thus leads to a completely different selection mechanism that is closer to what is observed, for example, in dendritic growth [30] and which requires anisotropy in the system. Corvera Poire et al. (Poire and Amar, 1998) directly solved the problem for a power law fluid; their results are in good agreement with the experimental observations. Note that at high velocities one observes a saturation of ρ, leading to an increase of the finger widths. This might be attributed to inertial effects, which have been observed to increase finger width (Chevalier et al., 2006) and which may begin to play a role in this low viscosity fluid.

In experiments using solutions of the flexible polymer, completely different behavior is found. In contrast to the observations in shear thinning fluids, where finger narrowing occurs, one now observes finger widening compared to the Newtonian case (see Fig. 6.4 left). The presence of normal stresses in the thin wetting layer might be responsible for the finger widening; one can attempt to account for this effect by adding a supplementary pressure to the system. In classical theory, the pressure jump at the interface between two liquids is given by the radius of curvature. Tabeling et al. (Tabeling and Libchaber, 1986) have shown that one can incorporate the effect of a finite thickness of the wetting film by correcting the surface tension in the control parameter. Following the same argument, in the control parameter one can add the supplementary pressure caused by the normal stresses to the surface tension term $\sigma^* = \sigma + 1/2N_1(\dot{\gamma})b$. For moderate normal stresses, this allows rescaling of the data onto one universal curve and once again solves the selection problem.

6.3.3 Faraday instability

6.3.3.1 Newtonian liquids

The Faraday experiment was first reported in 1831 (Faraday, 1831). In the appendix of this paper, Faraday reports on the crispated state of a layer of liquid that is shaken

vertically. He refers to works by 'Oersted, Wheatstone and Weber and probably others (sic)' who had earlier mentioned the phenomenon; however, according to Faraday, it was he who gave the first conclusive description. The experimental setup consisted of a box that was mounted on a rod. The rod was set into vibration by a bow; its oscillation frequency was presumably on the order of a few Hz. When the oscillation amplitude exceeded a certain critical value, standing capillary surface waves were observed. Apparently, Faraday was impressed by the richness of the patterns and noted: 'obtained in this way the appearances were very beautiful, and the facilities very great'. It is a remarkable achievement that even at that early date Faraday found that the surface waves oscillate with half of the driving frequency. This is the so-called subharmonic response. Faraday also pointed out differences in the wavy surface patterns when he compared simple oils with, e.g., the white of an egg. He stated: 'The difference between oil and white of egg is remarkable; . . . the crispated state may be a useful and even important indication of the internal constitution of different fluids.'

In 1868, Matthiesen (Matthiesen, 1868) reported on systematic measurements; he stated incorrectly that the surface response should be synchronous to the drive. In 1883, Lord Rayleigh (Rayleigh, 1883) proposed a theoretical treatment in terms of a parametric pendulum, the Mathieu oscillator. In 1954, Benjamin and Ursell (Benjamin and Ursell, 1954) solved the linear problem for ideal liquids (without viscosity) with an infinite set of Mathieu oscillators that oscillate with integral and $(n+1)/2$ multiples of the driving frequency. The integral multiples correspond to a possible harmonic (synchronous) response and the $(n+1)/2$ to a subharmonic response (Fig. 6.6). In 1994, Kumar and Tuckerman (Kumar and Tuckerman, 1994) presented a numerical analysis of the linear problem in the case of viscous liquids with finite depth of the layer. Together with an analytical treatment, this analysis was used to find parameters to experimentally reproduce a harmonic response using a very thin layer of liquid (Muller et al., 1997). Recently, a large variety of patterns with up to 10-fold rotational symmetry (quasiperiodic), superlattices or localized patterns have been reported (Binks and Water, 1997; Arbell and Fineberg, 1998). A variety of these patterns could be obtained using a simple liquid driven with a single frequency. Near onset, in linear order, a single wave number first became unstable. The resulting wave vector(s) could have any orientation, but nonlinear interaction with the higher harmonics led to a given pattern selection process (Muller et al., 1997). Obviously, the pattern dynamic might become even richer if two discrete wave numbers become unstable simultaneously.

It is worth mentioning that numerical simulation of the full hydrodynamical problem of the Faraday experiment with a single driving frequency for simple liquids became available only very recently (Perinet and Juric, 2009). Perinet et al. solved the complete nonlinear Navier-Stokes equations by a finite-difference projection method coupled to a Front Tracking technique for the calculation of the surface tension forces and advection of the interface. They compared the complete spatial and temporal Fourier spectrum of the surface state and found good agreement with experimental data from Kityk et al. (Kityk et al., 2005). A quantitative theoretical description of the nonlinear wave state of polymeric liquids remains an even more challenging problem that is still unsolved.
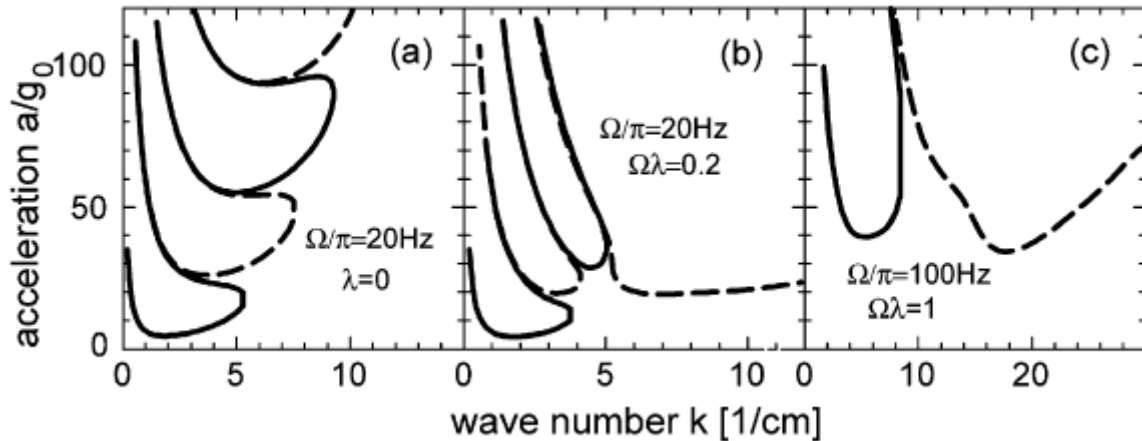
FIGURE 6.6: The linear stability diagram of the Faraday experiment
for a Maxwell fluid. a) For a Newtonian fluid, (b) For polymeric fluids
with finite relaxation time, (c) For polymeric fluids when the inverse
polymer relaxation time compares to the driving angular frequency Ω
(Source (Muller and Zimmermann, 1999)).

6.3.3.2 Polymeric liquids

The first experimental data on Faraday waves of polymer solutions were, to our
knowledge, presented in 1998 by Raynal, Kumar and Fauve (Raynal, Kumar, and
Fauve, 1999). Their work concentrates on dilute polymer solutions where the in-
fluence of elasticity is small. They found a slight shift of the critical acceleration;
the critical wave numbers were not affected. In 1999, Muller and Zimmermann
presented a linear stability analysis for a Maxwell fluid (Muller and Zimmermann,
1999). They found that when the inverse of the relaxation time of the Maxwell fluid
compares to the driving frequency, a harmonic response might become unstable first
and that, for a certain set of parameters, a bistable situation exists; see Fig. 6.6.
Again, in 1999, Wagner and Muller presented experimental and theoretical data on a
Faraday experiment using a concentrated polymer solution of 2000 ppm (mol weight:
4×10^6 g/mol) in a water-glycerol mixture (Wagner, Muller, and Knorr, 1999) with
a relaxation time $\tau_p \sim 1$s. The rheological data obtained for the complex viscosity
was then fed into the linear stability algorithm of Kumar and Tuckerman (Kumar
and Tuckerman, 1994) and a reasonable agreement of the experimentally and numer-
ically determined critical accelerations was obtained. Notably, a bicritical situation
was found in which the subharmonic and harmonic responses became unstable si-
multaneously. For parameters where only a harmonic response existed, a coherent
pattern of hexagons was observed (Fig. 6.7a). The hexagonal symmetry is generic
for a harmonic response where the temporal symmetry allows the coupling of three
wave vectors H_n that are equally distributed on the critical circle (Fig. 6.7c). For fre-
quencies close to the bicritical point, with increasing driving strength subharmonic
wave vectors S_n also become unstable. They are slaved by the harmonic hexagonal
pattern and arrange together to a 2×2 superlattice. The nomenclature is taken from
crystallography and relates to the ratio of $1 : 2$ of the harmonic and subharmonic
wave vectors, which is close to the ratio of linear unstable wave numbers (Fig. 6.7b).

The pattern-forming process can be understood in the following way. The linear
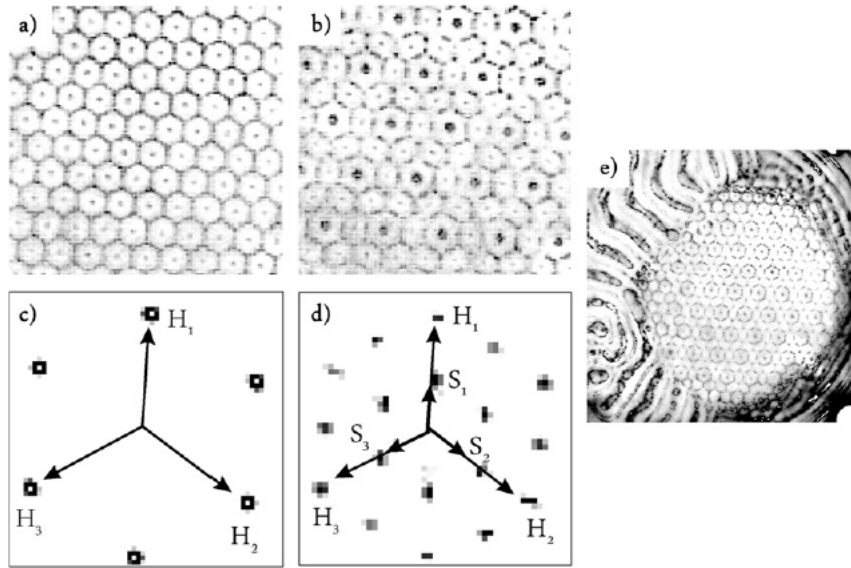
FIGURE 6.7: (a) The harmonic hexagonal pattern, (b) The harmonic-subharmonic hexagonal superlattice, (c) and (d) The respective spatial Fourier spectra, (e) Localized stationary surface patterns of harmonic hexagons in coexistence with a localized nonstationary patch of lines. (Source (Wagner, Muller, and Knorr, 1999)).

stability analysis reveals that the surface state consists of a singular wave number k (only exactly at the bicritical point do two wave modes synchronously become unstable) but of an infinite series of temporal Fourier components, $n\Omega$ or $(n+1)/2\Omega$ for the harmonic or subharmonic responses, respectively. This linear result is fed into the nonlinear equations for the hydrodynamic velocity field $\mathbf{v}$. The solvability condition in quadratic order implies that resonant terms must vanish in the higher orders to prevent secular growth. For the temporal components, an arbitrary quadratic nonlinearity results in a frequency spectrum of integral multiples of Ω whether or not S or H are considered. Thus, quadratic nonlinearities are able to resonate with harmonic linear eigenmodes, but not with subharmonic ones. In the same way, spatial resonance must be guarantied as well. Now, any triplet of harmonic modes $\{\mathbf{k}_{H1}, \mathbf{k}_{H2}, \mathbf{k}_{H3}\}$ with $|\mathbf{k}_{Hm}| = k_H$ and $\mathbf{k}_{H1} + \mathbf{k}_{H2} + \mathbf{k}_{H3} = 0$ are in resonance. This generic 3-wave vector coupling is well known (e.g., from non-Boussinesq-Rayleigh-Benard convection) and enforces a saddle node bifurcation towards hexagonal patterns. The associated solvability condition is referred to as the amplitude equation or Ginzburg-Landau equation. Within the subharmonic regime, such a resonant 3-wave vector coupling is prohibited due to the missing temporal resonance. The pattern selection mechanism is therefore then controlled by the cubic coupling coefficient in the associated amplitude equations (Edwards and Fauve, 1994; Chen, 1997), and a variety of patterns is allowed.

For increased driving strength, localized patches of hexagons have also been observed. They cannot be explained by a triplet of real Landau equations supplemented by diffusive spatial derivatives, since within this familiar amplitude equation model, stable isolated islands of hexagons do not exist. For even larger driving strength, the patterns become chaotically time-dependent. Patches of subharmonically oscillating

lines originating in an erratic manner from the cell boundary or the flat surface penetrate into the stationary hexagonal superlattice. They then disappear and the original structure is recovered. This process repeats itself on time scales of seconds to minutes, leading to a temporary coexistence of the stationary hexagonal superlattice with subharmonic lines. Higher driving amplitudes lead to a fully chaotic surface pattern. Still, no satisfying theoretical description of these states exists.

6.4 Conclusions

Further examples of hydrodynamic surface instabilities include the Kelvin-Helmholtz instability (the interfacial instability of two liquids that are sheared against each other), the Rayleigh-Taylor instability (that of the interface between two liquids of different densities with the heavier liquid placed on top of the lighter), the Benard Marangoni (an instability that occurs when a layer of liquid that is heated from below becomes unstable due to differences in the surface stresses caused by thermal gradients), the case in which a thin film flowing down an inclined plane becomes unstable against wavy distortion (Gupta, 1967) and the disintegration of a liquid jet into droplets (Eggers and Villermaux, 2008). Some of these systems have been investigated for the case of complex liquids (Graham, 2003). A special case is the so-called shark-skin instability (Tordella, 1956; Denn, 1990), which refers to the appearance of a wavy distortion on a polymeric fiber that is forced through a hole or slit (a 'die') above a critical speed. This instability is attributed either to an instability at the solid-liquid interface (stick-slip) or to a bulk instability (Bertola et al., 2003). All these instabilities will be investigated via spatiotemporal analysis at a later time.

Bibliography

A. A. Draad, G. D. C. Kuiken and F. T. M. Nieuwstadt (1998). "Laminar–turbulent transition in pipe flow for Newtonian and non-Newtonian fluids". In: *J. Fluid Mech.* 377, pp. 267–312.

Afendikov, A. L. and T. J. Bridges (2001). "Instability of the Hocking-Stewartson pulse and its implications for three-dimensional Poiseuille flow". In: *Proc. R. Soc. Lond* A457, pp. 257–272.

Agoston, G.A. et al. (1954). "Flow of Gasoline Thickened by Napalm". In: *Eng. Chem.* 46.5, pp. 1017–1019.

Akylas, T. R. (1982). "A nonlinear theory for the generation of water waves by wind". In: *Studies in Appl. Math.* 67, pp. 1–24.

Akylas, T. R. and D. J. Benney (1980). "Direct resonance in nonlinear wave systems". In: *Studies in Appl. Math.* 63.209-226.

Akylas, T. R. and D. J. Benney (1982). "The Evolution of Waves Near Direct-Resonance Conditions". In: *Studies in Appl. Math.* 67, pp. 107–123.

Alhushaybar, A. and J. Uddin (2019). "Convective and absolute instability of viscoelastic liquid jets in the presence of gravity". In: *Phys. Fluids* 31, p. 044106.

Alhushaybari, A. and J. Uddin (2020). "Absolute instability of free-falling viscoelastic liquid jets with surfactants". In: *Phys. Fluids* 32, p. 013102.

Allen, L.A. and T.J. Bridges (2002). "Numerical exterior algebra and the compound matrix method". In: *Numer. Math.* 92, pp. 197–232.

Amarouchene, Y. et al. (2001). "Inhibition of the finite-time singularity during droplet fission of a polymeric fluid". In: *Phys. Rev. Lett.* 86, pp. 3558–3561.

Andereck, C.D., S.S. Liu, and H.L. Swinney (1986). "Flow regimes in a circular Couette system with independently rotating cylinders". In: *J. Fluid. Mech.* 164.155-183.

Aranha, J.A., D.K.P. Yue, and C.C. Mei (1982). "Nonlinear waves near a cut off frequency in an acoustic duct- a numerical study". In: *J. Fluid Mech.* 121, pp. 465–485.

Arbell, H. and J. Fineberg (1998). "Spatial and temporal dynamics of two interacting modes in parametrically driven surface waves". In: *Phys. Rev. Lett.* 81, pp. 4384–4387.

Azaiez, J. and G. M. Homsy (1994a). "Linear stability of free shear flow of viscoelastic liquids". In: *J. Fluid. Mech.* 268, pp. 37–69.

Azaiez, J. and G. M. Homsy (1994b). "Numerical simulation of non-Newtonian free shear flows at high Reynolds numbers". In: *J. Non-Newtonian Fluid Mech.* 52, pp. 333–374.

Barkley, D. (2016). "Theoretical perspective on the route to turbulence in a pipe". In: *J. Fluid Mech.* 803, P1.

Batchelor, G. K., H. K. Moffatt, and M. G. Worster (2002). *Perspectives in Fluid Dynamics: A Collective Introduction to Current Research*. Cambridge University press.

Benjamin, T. B. and F. Ursell (1954). "Numerical simulation of Faraday waves". In: *Proc. R. Soc. London Ser. A* 225, p. 505.

Benny, D. J. and L. H. Gustavsson (1981). "A new mechanism for linear and nonlinear hydrodynamic instability". In: *Studies in Appl. math* 64, pp. 185–209.

Bers, A. (1983). *Space-time evolution of plasma instabilities-absolute and convective*. Vol. 1. Handbook of Plasma Physics.

Bertola, V. et al. (2003). "Melt fracture in polymer extrusion". In: *Phys. Rev. Lett.* 90.114502.

Bhaumik, S. and T. K. Sengupta (2017). "Impulse response and spatio-temporal wave-packets: The common feature of rogue waves, tsunami, and transition to turbulence". In: *Phys. Fluids* 29, p. 124103.

Binks, D. and W. van de Water (1997). "Nonlinear pattern formation of Faraday waves". In: *Phys. Rev. Lett.* 78, pp. 4043–4046.

Bird, R. B., R. C. Armstrong, and O. Hassager (1987). *Dynamics of polymeric liquids, Volume 1: Fluid Mechanics*. 2nd. Wiley Intersciences.

Bird, R. B. et al. (1987). *Dynamics of polymeric liquids, Volume 2: Kinetic Theory*. 2nd. Wiley Intersciences.

Bistagnino, A. et al. (2007). "Nonlinear dynamics of the viscoelastic Kolmogorov flow". In: *J. Fluid Mech.* 590, pp. 61–80.

Boger, D.V. and K. Walters (1993). *Rheology Phenomena in Focus*. 1st ed. Vol. 4. Elsevier.

Bridges, T.J. (1999). "The Orr-Sommerfeld equation on a manifold". In: *Proc. R. Soc. Lond* A455, pp. 3019–3040.

Briggs, R. J. (1964). *Electron-stream interaction with plasmas*. MIT Press, Cambridge.

Byars, J. A. et al. (1994). "Spiral instabilities in theflow of highly elastic fluids between rotating parallel disks". In: *J. Fluid Mech.* 271, pp. 173–218.

Cadot, O. and S. Kumar (2000). "Experimental characterization of viscoelastic effects on two- and three-dimensional shear instabilities". In: *J. Fluid Mech.* 416, pp. 151–172.

Carroll, B. (1986). "Equilibrium conformations of liquid-drops on thin cylinders under forces of capillarity-a theory for the roll-up process". In: *Langmuir* 2, pp. 248–250.

Chang, H., E. Demekhin, and E. Kalaidin (1999). "Iterated stretching of viscoelastic jets". In: *Phys. Fluids* 11, pp. 1717–1737.

Chaudhary, I. et al. (2021). "Linear instability of viscoelastic pipe flow". In: *J. Fluid Mech.* 908.A11.

Chen, P. (1997). "Vinals, Pattern selection in Faraday waves". In: *Phys. Rev. Lett.* 79, pp. 2670–2673.

Chevalier, C. et al. (2006). "Inertial effects on Saffman-Taylor viscous fingering". In: *J. Fluid Mech.* 552, pp. 83–97.

Choueiri, G. H., J. M. Lopez Alonso, and B. Hof (2018). "Exceeding the asymptotic limit of polymer drag reduction". In: *Phys. Rev. Lett.* 120, p. 124501.

Chuoke, R., P. V. Meurs, and C. V. D. Poel (1959). "The instability of slow, immiscible, viscous liquid–liquid displacements in permeable media". In: *Pet. Trans. AIME* 216, p. 188.

Clanet, C. and J. C. Lasheras (1999). "Transition from dripping to jetting". In: *J. Fluid Mech.* 383, pp. 307–326.

Clemmow, P.C. and J.P. Dougherty (1969). *Electronics of particles and plasmas*. Reading, Mass: Addison-Wesle.

Coelho, P. M. and F. T. Pinho (2003). "Vortex shedding in cylinder flow of shear-thinning fluids I. Identification and demarcation of flow regimes". In: *J. Non Newt. Fluid Mech.* 110, pp. 143–176.

Combescot, R. et al. (1986). "Shape selection of Saffman-Taylor fingers". In: *Phys. Rev. Lett.* 56, pp. 2036–2039.

Conte, S.D. (1966). "The Numerical Solution of Linear Boundary Value Problems". In: *SIAM Rev.* 8, p. 309.

Cremer, L. (1953). "Theorie der Luftschall-Di mpfung im l echteckkanal mit schluckender Wand und das sich dabei ergebende hSchste DS mpfungsmag". In: *Acustica* 8, pp. 249–263.

Crighton, D.G. and M. Gaster (1976). "Stability of slowly-diverging jet flow". In: *J. Fluid Mech* 77, pp. 397–413.

Davey, A. (1979). "On the removal of the singularities from the Riccati method". In: *J. Comp. Phys.* 30, pp. 137–144.

Davey, A. (1980). "On the numerical solution of difficult boundary-value problems". In: *J. Comp. Phys.* 35, pp. 36–47.

Davies, A. R. (1988). "Reentrant corner singularities in non-Newtonian flow. Part 1. Theory". In: *J. Non-Newt. Fluid Mech.* 29, pp. 269–293.

Delbende, I. and J. M. Chomaz (1998). "Nonlinear convective/absolute instabilities in parallel two-dimensional wakes". In: *Phys. Fluids* 10, p. 2724.

Denn, M.M. (1990). "Issues in Viscoelastic Fluid Mechanics". In: *Annu. Rev. Fluid Mech.* 22, pp. 13–32.

Denn, M.M. (2001). "EXTRUSION INSTABILITIES AND WALL SLIP". In: *Annu. Rev. Fluid Mech.* 33, pp. 265–287.

Denn, M.M. (2004). "Fifty years of non-Newtonian fluid dynamics". In: *A.I.Ch.E.J.* 50, pp. 2335–2345.

Destarde, M., A. N. Annaidh, and C. D. Coman (2009). "Bending of soft biological tissues". In: *Int. J. Solids Struct.* 46, pp. 4322–4330.

DiPrima, R.C. and H.L. Swinney (1981). "Hydrodynamic instabilities and Transition to Turbulence". In: ed. by J.P. Gollub H.L. Swinney. New York: Springer. Chap. Instabilities and transition in flow between concentric rotating cylinders.

Drazin, P. G. and W. H. Reid (2004). *Hydrodynamic stability*. 2nd. Cambridge University Press.

Edwards, W. and S. Fauve (1994). "Patterns and quasi-patterns in the Faraday experiment". In: *J. Fluid Mech.* 278, pp. 123–148.

Eggers, J. (1993). "Universal pinching of 3d axisymmetrical free-surface flow". In: *Phys. Rev. Lett.* 71, p. 3458.

Eggers, J. (1997). "Nonlinear dynamics and breakup of free-surface flows". In: *Rev. Mod. Phys.* 69, pp. 865–929.

Eggers, J. and E. Villermaux (2008). "Physics of liquid jets". In: *Rep. Progr. Phys.* 71, p. 036601.

Evans, J. D. (2010). "Re-entrant corner behavior of the PTT fluid with a solvent viscosity". In: *J. Non Newt. Fluid Mech.* 165.9, pp. 527–537.

Faraday, M. (1831). "On the forms and states of fluids on vibrating elastic surfaces". In: *Philos. Trans. R. Soc. London* 52, p. 319.

Fattal, R. and R. Kupferman (2004). "Constitutive laws for the matrix-logarithm of the coformation tensor". In: *J. Non-Newt. Fluid Mech.* 123, pp. 281–285.

Ferras, L. L. et al. (2019). "A generalised Phan-Thien-Tanner model". In: *J. Non Newt. Fluid Mech.* 269, pp. 88–89.

Fu, Y. B. and M. S. Pour (2002). "WKB method with repeated roots and its application to the buckling analysis of an everted cylindrical tube". In: *SIAM J. Appl. Maths* 62, pp. 1856–1871.

Fu, Yibin. "Compound matrix method and evans function - a quick introduction". Keele University.

G. G. Lipscomb R. Keunings, M. Denn (1987). "Implications of boundary singularities in complex geometries". In: *J. Non-Newt. Fluid Mech.* 24, pp. 85–96.

gaster, M., E. Kit, and I. Wygnanski (1985). "Large scale structures in a forced tubulent mixing layer". In: *J. Fluid Mech.* 150, pp. 23–29.

Gilbert, F. and G. Backus (1966). "Propagator Matrices in elastic wave and vibration problems". In: *Geophysics* 31, pp. 326–332.

Goddard, J. D. (1979). "Polymer Fluid Mechanics". In: *Adv. Appl. Mech.* 19, pp. 143–219.

Godunov, S. (1961). "Numerical solution of boundary-value problems for systems of linear ordinary differential equations". In: *Uspekhi Mat. Nauk* 16, pp. 171–174.

Govindarajan, R. and K. C. Sahu (2013). "Instabilities in Viscosity-Stratified Flow". In: *Annu. Rev. Fluid Mech.* 46, pp. 331–353.

Graham, M. D. (2003). "Interfacial hoop stress and instability of viscoelastic free surface flows". In: *Phys. Fluids* 15.6, pp. 1702–1710.

Graham, M. D. (2014). "Drag reduction and the dynamics of turbulence in simple and complex fluids". In: *Phys. Fluids* 26, p. 101301.

Groisman, A. and V. Steinberg (1998). "Mechaism of elastic instability in Couette flow of polymer solutions: experiments". In: *Phys. Fluids* 10.2451.

Groisman, A. and V. Steinberg (2000). "Elastic turbulence in a polymer solution flow". In: *Nature* 405, pp. 53–55.

Groisman, A. and V. Steinberg (2001). "Efficient mixing at low Reynolds numbers using polymer additives". In: *Nature* 410.905.

Groisman, A. and V. Steinberg (2004). "Elastic turbulence in curvilinear flows of polymer solutions". In: *New J. Phys.* 6.29.

Gubernov, V.V. et al. (2003). "Evans function stability of combustion waves". In: *SIAM J. Appl. Math.* 63, pp. 1259–1275.

Gupta, A. (1967). "Stability of a visco-elastic liquid film flowing down an inclined plane". In: *J. Fluid Mech.* 28.1, pp. 17–76.

Gustavsson, L. H. (1981). "Resonant growth of three-dimensional disturbances in plane Poiseuille flow". In: *J. Fluid Mech* 112.253-264.

Gustavsson, L. H. and L. S. Hultgren (1980). "A resonance mechanism in plane Couette flow". In: *J. Fluid Mech* 98, pp. 149–159.

Hagen, T. and M. Renardy (1997). "Boundary layer analysis of the Phan-Thien-Tanner and Giesekus model in high Weissenberg number flow". In: *J. Non-Newt. Fluid Mech.* 73, pp. 181–189.

Hansen, R. J. and R. C. Little (1974). "Early turbulence and drag reduction phenomena in larger pipes". In: *Nature* 252.690.

Healy, J. J. (2009). "Destabilizing effects of confinement on homogeneous mixing layers". In: *J. Fluid Mech.* 623, pp. 241–271.

Hibberd, M., M. Kwade, and R. Scharf (1982). "Influence of drag reducing additives on the structure of turbulence in a mixing layer". In: *Rheo. Acta* 21, pp. 582–586.

Hill, C.T. (1972). "Nearly Viscometric Flow of Viscoelastic Fluids in the Disk and Cylinder System. II: Experimental," in: *Trans. Soc. Rheol.* 16, p. 213.

Ho, C.M. and P. Huerre (1984). "Perturbed free shear layers". In: *Annu. Rev. Fluid Mech.* 16, pp. 365–424.

Hof, B. et al. (2004). "Experimental observation of nonlinear travelling waves in turbulent pipe flow". In: *Science* 305.1594.

Huang, Z. and X. Wu (2015). "A non-perturbative approach to spatial instability of weakly non-parallel shear flows". In: *Phys. Fluids* 27, p. 054102.

Huerre, P. and P. A. Monkewitz (1985). "Absolute and convective instabilities in free shear layers". In: *J. FLuid Mech.* 159, pp. 151–168.

Huerre, P. and P. A. Monkewitz (1990). "Local and global instabilities in spatially developing flows". In: *Ann. Rev. Fluid Mech.* 22, pp. 473–537.

Hulsen, M.A., R. Fattal, and R. Kupferman (2005). "Flow of viscoelastic fluids past a cylinder at high Weissenberg number: stabilized simulaton using matrix logarithms". In: *J. Non-Newt. Fluid Mech.* 127, pp. 27–39.

Hultgren, L. S. and L. H. Gustavsson (1981). "Algebraic growth of disturbances in a laminar boundary layer". In: *Phys. Fluids* 24, pp. 1000–1004.

J. M. Chomaz, P. Huerre and L. G. Redekopp (1988). "Bifurcations to local and global modes in spatially developing flows". In: *Phys. Rev. Lett.* 60.1, pp. 25–28.

James, D. and J. Saringer (1980). "Extensional flow of dilute polymer-solutions". In: *J. Fluid Mech.* 97, pp. 655–676.

Joo, J L. and E.S.G. Shaqfeh (1994). "Observations of purely elastic instabilities in the Taylor-Dean flow of a Boger fluid". In: *J. Fluid Mech* 262, pp. 27–73.

Joseph, D.D. (1990). *Fluid Dynamics of Viscoelastic Liquids*. New York: Springer-Verlag.

Joseph, D.D. and R.L. Fosdick (1973). "The free surface on a liquid between cylinders rotating at different speeds. Part I." In: *Arch. Rational Mech. Anal.* 49, p. 321.

Kalashnikov, V. N. and A. M. Kudin (1970). "Kármán ortices in the flow of drag reducing polymer solutions". In: *Nature* 255, pp. 445–446.

Kalliadasis, S. et al. (2012). *Falling liquid films*. Vol. 176. Springer.

Kang, K. L. and K. S. Yeo (2017). "Hybrid POD-FFT analysis of nonlinear evolving coherent structures of DNS wavepacket in laminar-turbulent transition". In: *Phys. Fluids* 29, p. 084105.

Keunings, R. (1989). "Simulation of viscoelastic fluid flow". In: *Fundamentals of Computer Modeling for Polymer Processing*. Ed. by C. L. Tucker III.

Kityk, A. et al. (2005). "Spatiotemporal characterization of interfacial Faraday waves by means of a light absorption technique". In: *Phys. Rev. E* 72, p. 036209.

Koch, W. (1986). "Direct resonance in Orr-Sommerfeld problems". In: *Acta Mech.* 59, pp. 11–29.

Kondic, L., M. J. Shelley, and P. P. Muhoray (1998). "Non-Newtonian Hele–Shaw flow and the Saffman–Taylor instability". In: *Phys. Rev. Lett.* 80, pp. 1433–1436.

Kumar, K. and L. Tuckerman (1994). "Parametric-instability of the interface between 2 fluids". In: *J. Fluid Mech.* 279, pp. 49–68.

Kume, T. et al. (1997). "Rheo-optical studies of shear-induced structures in semidilute polystyrene solutions". In: *Macromolecules* 30, pp. 7232–7236.

Kupfer, K., A. Bers, and A. K. Ram (1987). "The cusp map in the complex-frequency plane for absolute instability". In: *Phys. Fluids* 30.10, pp. 3075–3082.

Lakin, W.D., B.S. Ng, and W. H. Reid (1978). "Approximations to the eigenvalue relation for the Orr-Sommerfeld problem". In: *Philos. Trans. Roy. Soc. London Ser.* A 289, pp. 347–371.

Landau, L.D. and E.M. Lifshitz (1959). *Fluid Mechanics.* London: Permagon Press.

Landau, L.D. and E.M. Lifshitz (1987). *Fluid mechanics.* Pergamon Press , Oxford.

Larson, R. G. (2000). "Turbulence without inertia". In: *Nature* 405, pp. 27–28.

Larson, R. G., E. S. G. Shaqfeh, and S. J. Mueller (1990). "A purely elastic instability in Taylor-Couette flow". In: *J. Fluid Mech.* 218, pp. 573–600.

Larson, R.G. (1988). *Constitutive equations for polymer melts and solutions.* AT&T Bell Laboratries.

Larson, R.G. (1999). *The structure and rheology of Complex fluids.* Oxford University Press, Oxford.

Lifshitz, E. M. and L.P. Pitaevskii (1981). "Physical kinetics". In: London: Pergamon. Chap. 6.

Lindner, A., D. Bonn, and J. Meunier (2000). "Viscous fingering in a shear-thinning fluid". In: *Phys. Fluids* 12, pp. 256–261.

Lindner, A. and C. Wagner (2009). "Viscoelastic surface instabilities". In: *Comptes Rendus Physique* 10, pp. 712–727.

Lindner, A. et al. (2002). "Viscous fingering in non-Newtonian fluids". In: *J. Fluid Mech.* 469, pp. 237–256.

Lindsay, K.A. and C.E. rooney (1992). "A note on compound matrices". In: *J. Comput. Phys.* 103, pp. 472–477.

Lingwood, R. J. (1997). "Absolute instability of the Ekman layer and related rotating flows". In: *J. Fluid Mech.* 331, pp. 405–428.

M. C. Guimaraes N. Pimentel, F. T. Pinho and C. B. da Silva (2020). "Direct numerical simulations of turbulent viscoelastic jets". In: *J. Fluid Mech.* 899, A11.

Magda, J. J. and R.G. Larson (1988). "A transition occuring in ideal elastic liquids duringshear flow". In: *J. Non-Newtonian Fluid Mech.* 30, pp. 1–19.

Malkus, D. S., J. A. Nohel, and B. J. Plohr (1991). "Analysis of New Phenomena in Shear Flow of Non-Newtonian Fluids". In: *SIAM J. Appl. Math.* 51.4, pp. 899–929.

Matthiesen, L. (1868). In: *Annal. Phys. Chem.* 5.14, p. 107.

McKinley, G. H., R. C. Armstrong, and R. A. Brown (1993). "The wake instability in viscoelastic flow past confined circular cylinders". In: *Phil. Trans. R. Soc. A* 344, pp. 265–304.

McLean, J. and P. Saffman (1981). "The effect of surface tension on the shape of fingers in a Hele-Shaw cell". In: *J. Fluid Mech.* 102, pp. 455–469.

Merkine, L.O. (1977). "Convective and absolute instability of baroclinic eddies". In: *Geophys. Astrophys. Fluid Dyn.* 9, pp. 29–57.

Meulenbroek, B. et al. (2003). "Intrinsic route to melt fracture in polymer extrusion:a weekly nonlinear subcritical instability of viscoelastic Poiseuille flow". In: *Phys. Rev. Lett.* 90.024502.

Meulenbroek, B. et al. (2004). "Weekly nonlinear subcritical instability of viscoelastic Poiseuille flow". In: *J. Non-Newt. Fluid Mech.* 116.235.

Mikaelian, K. (2014). "Boussinesq approximation for Rayleigh-Taylor and Richtmyer-Meshkov instabilities". In: *Phys. Fluids* 26, p. 054103.

Miller, J. C. and J. M. Rallison (2007). "Interfacial instability between sheared elastic liquids in a channel". In: *J. Non-Newt. Fluid Mech.* 143, pp. 71–87.

Monkewitz, P. A. (1988). "The absolute and convective nature of instability in two-dimensional wakes at low Reynolds numbers". In: *Phys. Fluids* 31.5, pp. 999–106.

Morozov, A.N. and W. van Sarloos (2005). "Subcritical finite-amplitude solutions in pane Couette flow of visco-elastic fluids". In: *Phys. Rev. Lett.* 95.024501.

Morozov, A.N. and W. van Sarloos (2007). "An introductory essay on subcritical instabilities and the transition to turbulence in visco-elastic parallel shear flows". In: *Phys. Rep.* 447, pp. 112–143.

Muller, H. and W. Zimmermann (1999). "Faraday instability in a linear viscoelastic fluid". In: *Europhys. Lett.* 45, pp. 169–174.

Muller, H. et al. (1997). "Analytic stability theory for Faraday waves and the observation of the harmonic surface response". In: *Phys. Rev. Lett.* 78, pp. 2357–2360.

Muller, S. J., R. G. Larson, and E. S. G. Shaqfeh (1989). "A purely elastic transition in Taylor-Couette flow". In: *Rheol. Acta* 28, pp. 499–503.

Mysels, K. J. (1949). *Flow of Thickened Fluids*. U. S. Patent.

Negi, P. S. et al. (2019). "Bypass transition delay using oscillations of spanwise wall velocity". In: *Phys. Rev. Fluids* 4, p. 063904.

Newell, A. Coo and J.A. Whitehead (1969). "Finite bandwidth, finite amplitude convection". In: *J. Fluid Mech.* 38, pp. 279–303.

Ng, B. S. and W. H. Reid (1979a). "A numerical method for linear two-point boundary-value problems using compound matrices". In: *J. Comput. Phys.* 33, pp. 70–85.

Ng, B.S. and W. H. Reid (1979b). "An initial-value method for eigenvalue problems using compound matrices". In: *J. Comput. Phys.* 30, pp. 125–136.

Ng, B.S. and W. H. Reid (1985). "The Compound Matrix Method for Ordinary Differential Equations". In: *J. Comp. Phys.* 58, pp. 209–228.

Ngamaramvaranggul, V. and M. F. Webster (2002). "Simulation of pressure-tooling wire-coating flow with Phan-Thien/Tanner models". In: *Int. J. Num. Meth. fluids* 38.7, pp. 677–710.

Oertel, Jr. H. (1990). "Wakes behind blunt bodies". In: *Ann. Rev. Fluid Mech.* 22, pp. 539–564.

Oliveira, M. and G. McKinley (2005). "Iterated stretching and multiple beads-on-a-string phenomena in dilute solutions of highly extensible flexible polymers". In: *Phys. Fluids* 17, p. 071704.

Oliveira, M., R. Yeh, and G.H. McKinley (2006). "Iterated stretching, extensional rheology and formation of beads-on-a-string structures in polymer solutions". In: *J. Non-Newtonian Fluid Mech.* 137, pp. 137–148.

Owens, R.G. and T.N. Philips (2002). *Computational Rheology*. Imperial College press, London.

Pahl, M., W. Gleissle, and H.-M. Laun (1991). "Praktische Rheologie der Kunststoffe und Elastomere". In: *VDI verlag*.

Pego, R. L. and M. I. Weinstein (1992). "Eigenvalues, and instability of solitary waves". In: *Phil. Trans. R. Sc. Lond.* A340, pp. 47–94.

Perinet, L. T. N. and D. Juric (2009). "Numerical simulation of Faraday waves". In: *J. Fluid Mech.* 635, pp. 1–26.

Phan-Thien, N.J. (1983). "Coaxial-disk flow of an Oldroyd-B fluid: exact solution and stability". In: *J. Non-Newt. Fluid Mech.* 13, pp. 325–340.

Pier, B. (2008). "Local and global instabilities in the wake of a sphere". In: *J. Fluid Mech.* 603, pp. 39–61.

Pierce, A. D. (1981). *Acoustics: An introduction to its physical principles and applications*. New York: McGraw-Hill.

Pipe, C. (2005). "Experiments investigating the effects of fluid elasticity on laminar vortex shedding from a cylinder". MA thesis. EPFL.

Podgorski, T. and A. Belmonte (2002). "Surface folds during the penetration of a viscoelastic fluid by a sphere". In: *J. Fluid. Mech.* 460.337-348.

Poire, E. C. and M. B. Amar (1998). "Finger behavior of a shear thinning fluid in a Hele-Shaw cell". In: *Phys. Rev. Lett.* 81, pp. 2048–2051.

P.Pakdel and G.H. McKinley (1996). "Elastic instability and curved streamlines". In: *Phys. Rev. Lett.* 77.2459.

Provansal, M., C. Mathis, and L. Boyer (1987). "Bénard-von Kármán instability: transient and forced regimes". In: *J. Fluid Mech.* 182, pp. 1–22.

Rabaud, M., Y. Couder, and N. Gerard (1988). "Dynamics and stability of anomalous Saffman-Taylor fingers". In: *Phys. Rev. A* 37, pp. 935–947.

Rauwendaal, C. and P.J. Gramann (2001). *Polymer extrusion*. Hanser, Munich.

Ray, P. K. and T. A. Zaki (2014). "Absolute instability in viscoelastic mixing layers". In: *Phys. Fluids* 26, p. 014103.

Ray, P. K. and T. A. Zaki (2015). "Absolute/convective instability of planar viscoelastic jets". In: *Phys. Fluids* 27, p. 014110.

Rayleigh, J. W. (1883). "Numerical simulation of Faraday waves". In: *Phil. Mag. J. Sci.* 5, p. 229.

Raynal, F., S. Kumar, and S. Fauve (1999). "Faraday instability with a polymer solution". In: *Eur. Phys. J. B* 9, pp. 175–178.

Reiner, M., G. W. Scott Blair, and H.B. Hawley (1949). "The weissenberg effect in sweetened condensed milk". In: *J. Soc. Chem. Indus.* 68, pp. 327–328.

Reynolds, O. (1883). "An experimental investigation of the circumstances which determine whether the motion of water shall be direct or sinuous, and of the law of resistance in parallel channels". In: *O. Phil. Trans. R. Soc. Lond.* 174, pp. 935–982.

Riediger, S. (1989). *The influence of drag reduction additives on the coherent structures in a free shear layer*. Heidelberg: Adv. Turbulence 2: Springer-Verlag.

Rothert, A., R. Richter, and I. Rehberg (2003). "Formation of a drop: Viscosity dependence of three flow regimes". In: *New J. Phys.* 5.

Saffman, P. and G. Taylor (1958). "The penetration of a fluid into a porous medium or Hele-Shaw cell containing a more viscous liquid". In: *Proc. R. Soc. A* 245, pp. 312–329.

Samanta, D. et al. (2013). "Elasto-inertial turbulence". In: *Proc. Natl. Acad. Sci. USA* 110, p. 10557.

Sattler, R., C.Wagner, and J. Eggers (2008). "Blistering pattern and formation of nanofibers in capillary thinning of polymer solutions". In: *Phys. Rev. Lett.* 100, p. 164502.

Sattler, R., A. Kityk, and C. Wagner (2007). "Molecular configurations in the droplet detachment process of a complex liquid". In: *Phys. Rev. E* 75, p. 051805.

Schmid, P.J. and D.S. Henningson (2001). *Stability and transition in shear flows*. New York: Springer.

Schwarz, B. (1970). "Totally positive differential systems". In: *Pacific J. Math.* 32, p. 203.

Scott, M.R. (1973). "An initial value method for the eigenvalue problem for systems of ordinary differential equations". In: *J. Comput. Phys.* 12, p. 334.

Sengupta, T. K. (1992). "Solution of the Orr-sommerfeld equation for high wave numbers". In: *Computers fluids* 21.2, pp. 301–303.

Sengupta, T. K. (2012). *Instabilities of Flows and Transition to Turbulence*. CRC Press Boca Raton.

Sengupta, T. K. (2016). *Instabilities of Flows and Transition to Turbulence*. CRC Press Boca Raton.

Sengupta, T. K. and S. Bhaumik (2018). *DNS of Wall-Bounded Turbulent Flows: A first Principle Approach*. Singapore: Springer.

Sengupta, T. K. et al. (2016). "Roles of bulk viscosity on Rayleigh-Taylor instability: Non-equilibrium thermodynamics due to spatio-temporal pressure fronts". In: *Phys. Fluids* 28, p. 094102.

Sengupta, Tapan K. (2004). *Fundamentals of Computational Fluid Dynamics*. Universities Press, Hyderabad.

Shaqfeh, E. S. G. (1996). "Purely elastic instabilities in viscometric flows". In: *Ann. Rev. Fluid Mech.* 31, p. 129.

Shoji, T. et al. (2020). "On the origins of transverse jet shear layer instability transition". In: *J. Fluid Mech.* 890, A7–1.

Sircar, S. and D. Bansal (2019). "Spatiotemporal linear stability of viscoelastic free shear flows: Dilute regime". In: *Phys. Fluids* 31, p. 084104.

Sircar, S. and D. M. Bortz (2013). "Impact of flow on ligand-mediated bacterial flocculation". In: *Math. Biosci.* 245.2, pp. 314–321.

Sircar, S. and A. Roberts (2016a). "Ion mediated crosslink driven mucous swelling kinetics". In: *DCDS-B* 21.6, pp. 1937–1951.

Sircar, S. and A. J. Roberts (2016b). "Surface deformation and shear flow in ligand mediated cell adhesion". In: *J. Math. Biol.* 73.4, pp. 1035–1052.

Sircar, S., J. G. Younger, and D. M. Bortz (2014). *Sticky surface: sphere-sphere adhesion dynamics*.

Sircar, S. et al. (2015). "Determining equilibrium osmolarity in poly(ethylene glycol)/chondrotin sulfate gels mimicking articular cartilage". In: *J. Theor. Biol.* 364, pp. 397–406.

Sircar, S. et al. (2016). "Ligand-mediated adhesive mechanics of two static, deformed spheres". In: *Euro. Phys. J. E* 39.10, pp. 1–9.

Squires, T. M. and S. R. Quake (2005). "Microfluidics: fluid physics at nanoliter scale". In: *Rev. Mod. Phys.* 77, pp. 977–1026.

Steinberg, V. (2018). "Role of Thermal Noise in Dynamics of Non-equilibrium Systems: Macro-, Meso- and Microscopic." In: *J. Stat. Phys.* 175.(3-4), pp. 664–680.

Stewartson, K. and I.T. Stuart (1971). "A nonlinear instability theory for a wave system in plane Poiseuille flow". In: *J. Fluid Mech.* 48, pp. 529–45.

Stone, P. A. et al. (2004). "Polymer drag reduction in exact coherent structures of plane shear flow". In: *Phys. Fluids* 16.9, pp. 3470–3482.

Sturrock, P.A. (1958). "Kinematics of growing waves". In: *Phys. Rev.* 112, pp. 1488–1503.

Sundarama, P., T. K. Sengupta, and S. Sengupta (2019). "Is Tollmien-Schlichting wave necessary for transition of zero pressure gradient boundary layer flow?" In: *Phys. Fluids* 31, p. 031701.

Swinney, H.L. (1988). "Nonlinear Evolution and Chaotic Phenomena". In: ed. by P.F. Zweifel G. Gallavotti. Proceedings of a NATO advanced study institite, Plenum. Chap. Instabilities and chaos in rotating fluids, pp. 319–326.

Tabeling, P. and A. Libchaber (1986). "Film draining and the Saffman-Taylor problem". In: *Phys. Rev. A* 33, pp. 794–796.

Taneda, S. (1956). "Experimental investigation of the wakes behind cylinders and plates at low Reynolds numbers". In: *J. Phys. Soc. Japan* 11.3, pp. 302–307.

Tanner, R.I. and K. Walters (1998). *Rheology: An Historical Perspective*. Elsevier.

Taylor, G. I. (1923). "Stability of a viscous liquid contained between two rotating cylinders". In: *Phil. Trans. R. Sc. Lond.* A 223, pp. 289–343.

Thacker, W.C. (1976). "Spatial growth of gulf stream meanders". In: *Geophys. Fluid Dyn.* 7.27, pp. 1–95.

Thien, N. Phan (1978). "A nonlinear network viscoelastic model". In: *J. Rheology* 22.3, pp. 259–283.

Thien, N. Phan and R. I. Tanner (1977). "A new constitutive equation derived from network theory". In: *J. Non-Newtonian Fluid Mech.* 2.4, pp. 353–365.

Tirtaatmadja, V. and T. Sridhar (1993). "A filament stretching device for measurement of ex-tensional viscosity". In: *J. Rheology* 37, pp. 1081–1102.

Toms, B. A. (1948). "Some Observations on the Flow of Linear Polymer Solutions Through Straight Tubes at Large Reynolds Numbers". In: *Proc. of In. Cong. On Rheology* 135.

Toms, B.A. (1949). "Some Observations on the Flow of Linear Polymer Solutions Through Straight Tubes at Large Reynolds Numbers". In: *Proc. 1st Intern. Rheological Congress*. Vol. 2. 2. Netherlands: Norm-Holland Publish Co., pp. 135–142.

Tordella, J. P. (1956). "Fracture in the extrusion of amorphous polymers through capillaries". In: *J. Appl. Phys.* 27.454.

Tritton, D J. (1988). *Physical Fluid Dynamics*. Clarendon Press.

Twiss, R. Q. (1952). "Propagation in electronion streams". In: *Phys. Rev.* 88, pp. 1392–1407.

Vihinen, I., A. M. Honohan, and S. P. Lin (1997). "Image of absolute instability in a liquid jet". In: *Phys. Fluids* 9, p. 3117.

Vinogradov, G.V. and V.N. Manin (1965). "An experimental study of elastic turbulence". In: *Kolloid Z.* 201.93.

Wagner, C., H. Muller, and K. Knorr (1999). "Faraday waves on a viscoelastic liquid". In: *Phys. Rev. Lett.* 83, pp. 308–311.

Wagner, C. et al. (2005). "Droplet detachment and satellite bead formation in viscoelastic fluids". In: *Phys. Rev. Lett.* 95, p. 164504.

Weissenberg, K. (1947). "A continuum theory of rheological phenomena". In: *Nature* 159, pp. 310–311.

White, C. M. and M. G. Mungal (2008). "Mechanics and prediction of turbulent drag reduction with polymer additives". In: *Ann. Rev. Fluid Mech.* 40, pp. 235–256.

Wilson, H. J. and J. M. Rallison (1999). "Instability of channel flows of elastic liquids having continuously stratified properties". In: *J. Non-Newt. Fluid Mech.* 85, pp. 273–298.

Yeo, K.S., B.C. Khoo, and H.Z. Zhao (1996). "The absolute instability of boundary-layer flow over viscoelastic walls". In: *Theoret. Comput. Fluid Dynamics* 8, pp. 237–252.

Yu, Z. and N. Phan-Thien (2004). "Three-dimensional roll-up of a viscoelastic mixing layer". In: *J. Fluid Mech.* 500, pp. 29–53.

Zakin, J. L., B. Lu, and H. W. Bewersdorff (1998). "Surfactant Drag Reduction". In: *Rev. Chem. Eng.* 14.4-5.

List of Publications

1. Sarthok Sircar, Diksha Bansal, Spatiotemporal linear stability of viscoelastic free shear flows: Dilute regime, *Phys. Fluids* **31**, 084104(2019). https://doi.org / 10.1063 / 1.5115455

2. Satyajeet Singh, Diksha Bansal, Gagandeep Kaur, Sarthok Sircar, Implicit-explicit-compact methods for advection diffusion reaction equations, *Comp. and Fluids* **212**, 104709(2020).

3. Diksha Bansal, Dipa Ghosh, Sarthok Sircar, Spatiotemporal linear stability of viscoelastic free shear flows: non-affine regime,*Phys. Fluids*, Submitted.

Curriculum Vitae
Diksha Bansal

Girls Hostel
dikshab@iiitd.ac.in
IIIT Delhi, Okhla Industrial area phase-3,   bansal.diks24@gmail.com
New Delhi, Delhi-110020   +918882239314

Personal info

Date of birth : 24-07-1992
Nationality : Indian
Languages : Hindi and English
Research gate : https://www.researchgate.net/profile/Diksha _ Bansal2

Education

2017–Present : **Ph.D. Mathematics, Dept. Of mathematics, IIITD, Delhi**

2013–2015 :   M.Sc. Mathematics, University Of Delhi, Delhi
2010–2013 :   B.Sc. Mathematics, University Of Delhi, Delhi

Technical strengths

Language :   C, C++, Python
Software Skills : MS Office, Latex, MATLAB, Mathematica, Maple, Tecplot

Teaching assistant/Lecturer Experience

2018-19, 2019-20(Even sem) : TA(ODE/PDE)
2017-18, 2019-20(Odd sem) : TA(Multivariate calculus)
2019-20, 2020-Present(Odd sem) : NPTEL TA(Integral Transform and their Appl.)
2016-17(Odd sem) : Lecturer(B.Sc/B.A.) in Haryana.

Workshops and Conferences

- 'SPARC Workshop cum Conference' on "Advanced Neuro-Imaging and Clinical Applications" held at Indian Institute of Technology Kanpur, Kanpur, Jan 30, 2020 - Feb 2, 2020.

- GIAN Workshop on "Computational Solution of Hyperbolic PDEs for Scientists, Engineers and Mathematicians" held at Indian Institute of Technology Delhi, New Delhi, December 4, 2017-December 16, 2017.

National Exam Qualified

CSIR- NET(JRF) with AIR-55 in June 2016.